Structural and functional brain imaging using extended-focus optical coherence tomography and microscopy

PAR

Paul James MARCHAND

ÉCOLE POLYTECHNIQUE
FÉDÉRALE DE LAUSANNE

Suisse
2018

Abstract

Neuroimaging techniques aim at revealing the anatomy and functional organisation of cerebral structures. Over the past decades, functional magnetic resonance imaging (fMRI) has revolutionized our understanding of human cerebral physiology through its ability to probe neural activity throughout the entire brain in a non-invasive fashion. Nevertheless, despite recent technological improvements, the spatial resolution of fMRI remains limited to a few hundreds of microns, restricting its use to macroscopic studies. Microscopic imaging solutions have been proposed to circumvent this limitation and have enabled revealing the existence of various cerebral structures, such as neuronal and vascular networks and their contribution to information processing and blood flow regulation within the brain. Optical imaging has proven, through its increased resolution and available contrast mechanisms, to be a valuable complement to fMRI for cellular-scale imaging.

In this context, we demonstrate here the capabilities of an extension of optical coherence tomography, termed extended-focus optical coherence tomography (xf-OCT), in imaging cerebral *structure* and *function* at high resolution and very high acquisitions rates.

Optical coherence tomography is an interferometric imaging technique using a low-coherence illumination source to provide fast, three-dimensional imaging of the back-scattering of tissue and cells. By multiplexing the interferometric ranging over several spectral channels, Fourier-domain OCT performs depth-resolved imaging at very high acquisition rates and high sensitivity. Increasing the lateral resolution of optical systems typically reduces the available depth-of-field and thus hampers this depth multiplexing advantage of OCT. Extended-focus systems aim at alleviating this trade-off between imaging depth and lateral resolution through the use of diffraction-less beams such as Bessel beams, providing high resolution imaging over large depths. The xf-OCT system therefore combines fast acquisition rates and high resolution, both characteristics required to image and study the structure and function of microscopic constituents of cerebral tissue.

In this work, we performed functional brain imaging using the ability of xf-OCT to obtain quantitative measurements of blood flow in the brain. Changes in blood velocity evoked by neuronal activation were monitored and maps of hemodynamic activity were generated by adapting tools routinely used in fMRI to xf-OCT imaging. Additionally, three novel xf-OCT instruments are presented, wherein the advantages of different spectral ranges are exploited to reach specific imaging parameters. The increased contrast and resolution afforded by an illumination in the visible spectral range was used in two extended-focus optical coherence microscopy (xf-OCM) implementations for subcellular imaging of *ex-vivo* brain slices and cellular imaging of neurons, capillaries and myelinated axons in the superficial cortex *in-vivo*. Subsequently, an xf-OCT system is presented, operating in the infrared spectral range, wherein the reduced scattering enabled imaging the smallest capillaries deep in the murine cortex

Abstract

in-vivo.

Résumé

Les techniques de neuro-imagerie ont pour but de dévoiler l'anatomie et l'organisation fonctionelle de structures cérébrales. Au cours des dernières décennies, l'imagerie à résonnance magnétique fonctionnelle (fMRI) a révolutionné notre compréhension de la physiologie du cerveau humain par sa capacité à monitorer l'activité cérébrale dans l'integralité du cerveau de manière non-invasive. Malgré les récentes avancées technologiques, la résolution spatiale de l'fMRI reste limitée à quelques centaines de microns, limitant son application à des études macroscopiques.

L'imagerie à échelle microscopique a permit de franchir cette frontière spatiale et de dévoiler l'existance de structures neuronales et vasculaires et d'établir leur contribution dans le traitement d'information cognitif et dans la régulation du flux sanguin.

La haute résolution et le contraste provenant de l'imagerie optique en ont fait un complément attractif à l'fMRI dans le but d'imager la fonction et l'anatomie du cerveau à l'échelle cellulaire. C'est dans ce contexte que nous démontrons l'aptitude d'une variante de la tomographie en cohérence optique, nommée tomographie en cohérence optique à profondeur de champ étendue (xf-OCT), à imager la structure et la fonction de regions cérébrales à haute résolution et à très hautes fréquences d'acquisitions.

La cohérence en tomographie optique est une technique d'imagerie optique interférométrique à basse cohérence permettant d'obtenir des images tridimensionnelles de la rétrodiffusion d'un échantillon de tissue à très haute vitesse. La tomographie en cohérence optique fréquentielle (dans le domaine de Fourier) exploite un multiplexage spectral afin d'obtenir des images de profondeur à de très hautes fréquences d'aquisition et à très haute sensitivité. Dans des systèmes OCT classiques, augmenter la résolution latérale résulte en une reduction de la profondeur de champ accessible et détruit par conséquent l'avantage de multiplexage en profondeur de l'OCT. Les configurations à profondeur de champ étendue répondent à ce problème en employant des faisceaux exempt de diffraction, tel que les faisceaux de Bessel. Les systèmes xf-OCT permettent d'aquérir très rapidement des images à haute résolution et sont par conséquent parfaitement adaptés pour imager et étudier la structure et la fonction d'éléments microscopiques dans des régions cérébrales.

Dans la première partie de cette thèse, l'imagerie cérébrale fonctionelle utilisant l'xf-OCT est démontrée en mesurant de manière quantitative la vitesse du flux sanguin dans le cerveau. L'xf-OCT a été utilisé afin de monitorer des variations locales de flux sanguin suivant l'activation neuronale, qui ont ensuite été traitées afin de générer des cartes statistiques paramétriques d'activation vasculaire en utilisant des outils developpés pour l'fMRI. Trois nouveaux instruments xf-OCT sont ensuite présentés, utilisant les avantages intrinsèques de différentes bandes spectrales afin d'obtenir des charactéristiques d'imageries désirées. Le contrast accru et le gain en résolution résultant d'une illumination dans le

spectre visible ont été exploité dans deux microscopes en cohérence optique à profondeur de champ étendue (xf-OCM) dans le but d'imager des structures sous-cellulaires dans des coupes cervicales *ex-vivo* et des structures cellulaires, tels que des neurones, capillaires et axones dans le cerveaux de souris *in-vivo*. Un troisième système est aussi présenté, opérant dans le spectre infrarouge, afin de diminuer l'impacte de la rétrodiffusion du tissu et imager des capillaires dans les profondeurs du cortex de souris *in-vivo*.

Mots clés : Tomographie en cohérence optique (OCT) ; microscopie en cohérence optique (OCM) ; OCT fréquentiel (dans le domaine de Fourier) (FDOCT) ; microscopie sans agents de contraste ; imagerie tridimensionnelle ; OCT à profondeur de champ étendue (xf-OCT) ; OCM à profondeur de champ étendue (xf-OCM) ; champ sombre ; angiographie ; flux sanguin cérébrale ; vélocimétrie ; OCM dans le spectre visible (visOCM) ; hyperaemie fonctionelle ; imagerie cérébrale.

Contents

Contents

1 Background and thesis objectives

1.1   High resolution brain imaging

Functional magnetic resonance imaging (fMRI) has become the gold-standard for neuroimaging, through its ability to probe cerebral function non-invasively throughout the entire human brain [1]. fMRI provides indirect measurements of neuronal activity by probing evoked changes in the oxygenation levels of cerebral blood. Briefly, the magnetic properties of blood depend on its oxygenation state: hemoglobin is paramagnetic when deoxygenated while diamagnetic when oxygenated. As oxygenation changes occur in the brain, through consumption or increases in arterial/venal blood, these distinct magnetic signatures will lead to a different magnetic susceptibility of tissue, which can be measured using specific MRI imaging sequences (so-called blood oxygenation level dependent signals, BOLD [2]). As neuronal activity is typically associated with an increase in local oxygen concentration and a rise of blood flow to compensate for energy consumption, the local concentration of oxygenated hemoglobin will increase and result in a measurable change in magnetic susceptibility. As such, BOLD fMRI offers an indirect mean of monitoring cerebral activity. Using this principle, fMRI has extensively been used to map cerebral function and has ultimately revolutionized our understanding of human brain physiology. Through specific stimulation paradigms and powerful processing tools, event-related fMRI (er-fMRI) has shed light on the function of various brain regions and their interaction [3]. Moreover, a novel acquisition paradigm, termed resting-state fMRI (rs-fMRI) revealed the existence of networks of brain regions exhibiting similar spontaneous hemodynamic activity at rest [4]. Analysing the temporal correlations between the fluctuations of fMRI activity across cerebral structures provided so-called functional connectivity networks, which have been shown to vary with age [5] and along the time course of diseases such as multiple sclerosis [6] and other neuropathological disorders such as Alzheimer's disease (AD) [7, 8].

In spite of major advancements in fMRI technology, its spatial resolution and dependency on the vascular organisation within an imaging volume prevent interpreting and underpinning the causes of alterations in fMRI signals [9]. Moreover, despite efforts to increase the spatio-temporal resolution of fMRI, by increasing the field strength [10] or engineering novel acquisition schemes and sequences [11, 12], questions regarding the specificity of the fMRI signal (and certain features) to neuronal activity remain open. These features include salient spatio-temporal traits of the hemodynamic response function (HRF), such as the initial dip [13], the post-stimulus undershoot [14] and its laminar

organisation in cortical regions [12], and certain hemodynamic oscillations in the rs-fMRI signal [15, 16, 17].

Altogether, understanding the origins and specificity of the fMRI signal requires studying neural processes and cerebral hemodynamics at a high spatio-temporal resolution using complementary modalities, beyond the current limits of MR imaging. These imaging techniques could then provide direct measurements of vascular structures and functional features as neural activity, blood oxygenation, blood volume and blood velocity, which could ultimately be used to interpet fMRI results [18] and deepen our understanding of brain function. In view of this, we will briefly summarize the main imaging modalities currently available for high resolution brain imaging and later introduce optical coherence tomography (OCT) as a valuable tool to study cerebral physiology.
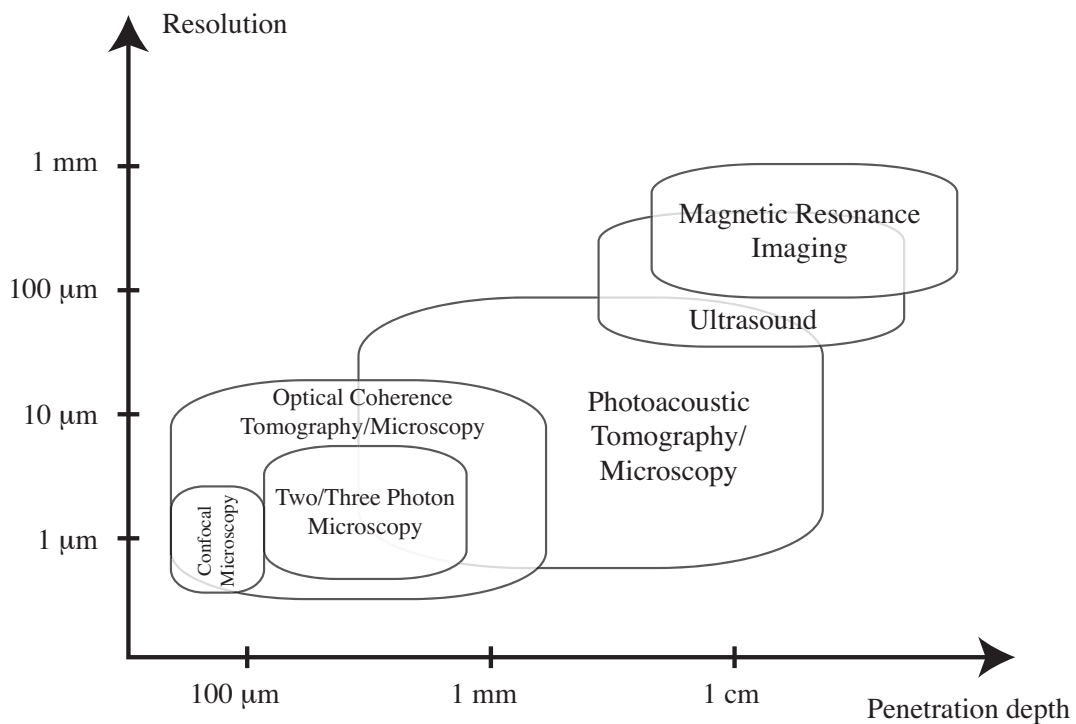
Figure 1.1 – Graphical presentation of current neuroimaging techniques and their achievable penetration depth and resolution

1.1.1   Ultrasound imaging

Acoustic imaging can perform non-invasive imaging by exposing tissue to pulsed waves and detecting the echoes reflected by tissue structures and vasculature [19]. As acoustic waves propagate deep into tissue, ultrasound imaging (US) can image over several centimeters in depth, throughout the entire depth of a rodent's brain. Through an extension termed Doppler US [20], US can also quantify cerebral blood volume (CBV) and cerebral blood flow (CBF), by taking advantage of the Doppler effect to differentiate between static and dynamic tissue (caused by blood flow for example) and estimate the velocity of blood. Although conventional US is typically limited spatially to a few hundreds of microns, a recent optimization of the ultrasonic acquisition and detection scheme has enabled functional US

(fUS) to capture changes in blood volume and flow at the capillary level with a high sensitivity (despite not being able to resolve individual capillaries) [21]. Moreover, combining the use of microbubbles as contrast agents [22] and skull-thinning surgical procedures [23] provides fUS with a sensitivity and depth penetration sufficient to assess the spatio-temporal characteristics of functional hyperamia over the entire depth of a rat's brain [23]. fUS has also shown its ability to measure the functional connectivity between various brain region using imaging protocols and processing tools developed for rs-fMRI [24]. By exploiting apriori knowledge along with novel signal processing schemes, US underwent a paradigm shift similar to optical superresolution, providing a spatial resolution sufficient to image penetrating arterioles and ascending venules in the rat cortex, *in vivo* [25]. Overall, fUS shows great promise for functional brain imaging, but remains limited to vascular imaging through its low resolution and lack of contrast and specificity. Moreover, although fUS is able to capture microvascular hemodynamics, its current resolution is insufficient to image individual capillaries.

1.1.2 Photoacoustic tomography

Photo-acoustic tomography (PAT) is a technique providing specificity and a potential spatial resolution increase to ultrasonic imaging by combining light absorption of endo- and/or exogenous contrast agents and ultrasonic detection [26]. In PAT, light pulses are focused on the sample, absorbed by a specific marker (whose absorption spectrum matches the illumination wavelength) which will locally heat up and dissipate by generating an acoustic wave (thermoacoustic effect) that is then detected by a microphone. Different designs of PAT provide varying levels of resolution and penetration depths, such as photo-acoustic computed tomography (PACT), acoustic-resolution photo-acoustic microscopy (PAM) and optical-resolution PAM [27]. By exploiting the wavelength-dependent differences in absorption of oxygenated and deoxygenated blood, PAT can provide label-free maps of the vasculature and of the oxygenation level of blood over large areas and depths. Using these capabilities, PAT has been used to study the neurovascular coupling [27], analyse hemodynamic fluctuations in cerebral microvasculature [28] and assess functional connectivities in the brains of mice [29]. Moreover, using amyloid binding dyes, PAT could image the amyloid plaque distribution in brain slices and mice brains *in-vivo* [30]. Unfortunately, PAT requires submerging part of the instrument and the sample (i.e. mouse's head) under water to reduce the acoustic impedance mismatch between the sample and air in the path to detector[1]. Moreover, despite initial promising results, three-dimensional imaging of cortical microvasculature and depth-resolved analyses of cortical function are yet to be demonstrated.

1.1.3 Optical microscopy

Optical imaging uses electromagnetic radiation from the UV to the near infrared (NIR) wavelength range to image samples. By combining the shorter wavelength of light and high numerical aperture (NA) objectives, optical microscopy can perform imaging of tissue structures with a sub-micron lateral resolution, currently unachievable with most of the techniques described above. As will be discussed below, contrast in optical imaging originates both from the intrinsic scattering and absorption properties of the sample, whereas specificity can be obtained through the extrinsic contrast provided by

---

[1]The acoustic impedance mismatch reflects the changes in velocity of sound between two media, i.e. water and air. In optics, an equivalent can be found in the refractive index n, reflecting the reduction in the speed of light when propagating in a given medium with respect to vacuum. In optics, variations of n are relatively small, however in acoustics, a factor of $3 \div 4$ is observed between air and water, significantly attenuating the strength of acoustic waves. Impedance mismatching in US and PAT is therefore critical.

fluorescent labels. The structural organisation of the brain has been extensively studied with histology, where stains and dyes have offered means to differentiate between cerebral regions and provide insight into their cellular organisation. Here we will overview some of the main optical imaging techniques that have been developed to perform structural and functional brain imaging.

Wide-field optical imaging

In the visible spectral range, the wavelength-dependent absorption profiles of hemoglobin will differ depending on its oxygenation state [31]. Under red light (at 630 nm), deoxygenated hemoglobin has a significantly stronger absorption than when it is oxygenated. Conversely, green light (at 530 nm) is absorbed almost equally by both oxygenation states of hemoglobin (so-called isobestic point). Variations of light intensity in the green will thus provide qualititative information on the concentration of total hemoglobin (similarly to CBV), a relative reduction in reflectance will indicate a relative increase in blood volume and vice-versa. Similarly, changes in blood oxygenation will cause the reflectivity of red light to vary. By acquiring reflectance images of cortical tissue at several wavelengths, it is possible to extract the relative concentration of oxygenated and deoxygenated hemoglobin through Beer's law. This procedure is the basis for optical intrinsic signal imaging (OISI) [31] and its spectroscopic counterpart, functional near-infrared spectroscopy (fNIRS) [32]. OISI uses wavelengths in the visible spectrum and is more suited to image local cortical hemodynamics in the exposed brain or in rodents (where the skull is much thinner) and can be used to estimate changes in diameter and blood flow velocity in large vessels [33].

Assessing blood flow is also possible using coherent imaging, where the temporal behaviour of a speckle field, obtained by illuminating the exposed cortex with a coherent light source, will reflect the dynamics of flowing particles, i.e. red blood cells (RBC) [34]. The speckle pattern in avascular regions will remain static whereas it will decorrelate over time in blood vessels. This decorrelation is caused both by the RBCs crossing through the imaging pixel and by the Doppler shift experienced by the back-scattered light. Laser Doppler imaging (LDI) uses high speed cameras (up to 20 kHz) to measure the Doppler spectrum of each pixel of the camera and estimate the concentration and speed of blood using the zero and first order moments of the spectrum [35, 36]. Laser speckle contrast imaging (LSCI) takes advantage of the washout of the speckle pattern in vascular areas over the integration time of the camera to obtain contrast between vascularized and avascular areas [34]. In practice, contrast is obtained by calculating the spatial and temporal variance of the speckle patterns. Pixels containing vessels will appear smooth as the speckle pattern will fluctuate much faster than the integration time of the camera. Conversely, the spatial variance of avascular regions will be high, as speckle patterns intrinsically a have very high contrast (speckle patterns are formed by randomly distributed destructive and constructive interferences). An extension of LSCI, termed multi-exposure speckle imaging (MESI) acquires speckle images with a varying integration time to obtain an estimate of the speed of blood [37].

Neuronal activity, in contrast to vascular dynamics, can be captured in wide-field optical imaging through the use of voltage sensitive dyes [38] and fluorescent calcium indicators [39]. The intensity of the fluorescence will reflect either changes in the membrane potential of neurons or the concentration of calcium in their vicinity (which is linked to neuronal signaling). These agents generally need to be injected into the tissue under consideration (i.e. cortex) or require a viral injection or genetic modifications [40].

4

OISI, LSCI and fluorescence wide-field imaging are routinely used to localize brain regions and study the neurovascular coupling [33, 41] and resting-state hemodynamics in humans [42] and mice [43] and have been used to delineate alterations of functional connectivities in models of Alzheimer's disease [7], ischemia [44] and arterial stiffness [45]. Overall, wide-field optical imaging techniques are powerful tools to study cerebral function, but are limited as they only provide two-dimensional projections of cerebral activity. In OISI, LDI and LSCI, the illumination light typically diffuses into cortical tissue, is scattered multiple times before finally reaching the camera where it will have lost all depth information about the sample. It is then almost impossible with these techniques to characterize depth-dependent phenomenons of cerebral function, such as the laminar dynamics of cortical function and distinguish accurately between micro- and macrovascular hemodynamics. Similarly, wide-field fluorescence imaging conveys no information on the depth at which signals are collected. Overcoming this limitation requires optical techniques with depth sectioning capabilities.

Two-photon microscopy

Optical sectioning in microscopy can be obtained through various ways, by using a pinhole to block out-of-focus light, as in confocal microscopy [46], by using the washout of the fringes of an illumination pattern as in structured illumination [47, 48] or by restricting the spatial volume over which fluorescence excitation occurs, as in two-photon excitation fluorescence microscopy (2PEF) [49]. 2PEF uses a femtosecond pulse source in the near-infrared to excite fluorescent proteins and dyes and obtain three-dimensional images of labelled structures. In contrast to confocal microscopy where a single photon is sufficient to excite the fluorescent agent, 2PEF relies on the simultaneous absorption of two photons to raise the fluorophore into its excited state [50]. As in 2PEF two concomitant photons place the fluorescent molecule into a higher electronic state, their individual energy is half the energy of photons in confocal microscopy (single photon microscopy). Two photon microscopy can thus perform fluorescence imaging using conventional fluorescent markers using a longer wavelength excitation sources (typically twice the wavelength of single photon microscopy). As the probability of the simultaneous absorption of multiple photons is very low, a large number of photons need to reach the fluorophore over a short time period to excite the molecule (typically within less than a 100 fs pulse). In practice, this can be achieved by combining femtosecond pulses with high NA objectives, providing a very tight focal volume. Away from the focal volume, the spatial spread (defocus) of the light pulse will prevent fluorescent proteins from being excited. As such, 2PEF has an intrinsic optical sectioning property, as fluorescence will only occur within the tightest region of the focal volume. Ultimately, a three-dimensional image can thus be obtained by scanning this focal volume across all three-dimensions, similarly to confocal microscopy. Altogether, the longer excitation and optical sectioning enables 2PEF to obtain fluorescence images up to hundreds of microns in depth (typically ~ 600 μm) [49].

Since its initial demonstration, 2PEF has rapidly become the mainstay for high-resolution neuro-imaging, through its increased penetration depth, compatibility with already existing imaging protocols and through the development of novel tools for specific imaging of neurophysiological processes (e.g. calcium indicators) [51]. It has enabled to shed light on neural signaling and computation [39, 40] and provided insight into cortical oxygenation [52, 53] and into the effect of neurodegenerative diseases on brain physiology [54]. The vasculature can be imaged by injecting a fluorescent solution into the blood stream (i.e. through intra-venous injections). Following such an injection, the plasma of blood will be

Imaging modality	Resolution	Depth penetration	Contrast mechanism	Optical sectioning
Ultrasound	$> 50 \mu m$	Entire rodent brain	Acoustic reflectance	Yes, temporal gating
PAT	$100 \mu m \div 1 \mu m$	Few millimeters	Light absorption	Yes, temporal gating
OIS	$\sim 10 \mu m$	$\sim 500 \mu m$	Light absorption	No
LDI	$\sim 10 \mu m$	$\sim 500 \mu m$	Speckle dynamics	No
LSCI	$\sim 10 \mu m$	$\sim 500 \mu m$	Speckle wash-out	No
Wide-field fluorescence	$\sim 10 \mu m$	$\sim 500 \mu m$	Fluorescence	No
Confocal microscopy	$\sim 0.2 \mu m^b$ / $\sim 1 \mu m^c$	$\sim 200 \mu m$	Fluorescence	Yes, confocal gating
Two-photon microscopy	$\sim 0.5 \mu m^a$ / $\sim 3 \mu m^b$	$\sim 600 \mu m$	Fluorescence	Yes, non-linear gating
OCT/OCM	$15 \mu m \div 0.5 \mu m^{a,b}$	$\sim 200 \mu m \div 1 mm^d$	Back-scattering	Yes, coherent gating

Table 1.1 – Table summarizing the performance of high-resolution brain imaging techniques

filled with a fluorescent agent, but red blood cells will remain unlabelled and will appear as dark dots in angiograms. Taking advantage of this inherent contrast, several strategies involving complex line scans have been devised to estimate the speed and concentration of RBCs flowing through capillaries [55]. Combining such strategies with calcium indicators has enabled 2PEF to underpin some of the pathways of the neuro-vascular coupling and the origins of certain hemodynamic oscillations observed in resting-state fMRI [16]. Overall, despite recent efforts in increasing the acquisition speed by using resonant scanners [56], remote-focusing [57] and temporal focusing [58], obtaining volumetric images in 2PEF can result in very long acquisitions times (few hours for a 3D volume). Moreover, specific modifications of the optical setup are required to simultaneously image different depths [59]. The need for exogeneous contrast agents also increases the overall invasiveness of the technique and can constrain the imaging conditions (the illumination wavelength needs to match the absorption spectrum of the contrast agent and can thus limit the penetration depth). Finally, the requirement of a tight focal volume additional slows down the total acquisition time, up to hours, when large volumes are imaged [60].

Taken altogether, the imaging techniques presented above and summarized in Table 1.1 possess unique advantages and disadvantages. Ultrasound imaging can image deep into tissue and provide functional information, but is limited in resolution and thus cannot resolve the capillary bed. Photo-acoustic tomography offers a similar depth advantage than fUS and can provide spectroscopic measurements of blood oxygenation, but high resolution three-dimensional imaging of cortical structures still hasn't been demonstrated yet. Wide-field imaging techniques are fast, can be label-free but are limited in resolution and cannot perform three-dimensional imaging. Finally, 2PEF can provide three-dimensional imaging of specific proteins and structures at high-resolution, but is inherently slow, invasive and is limited in depth by the illumination wavelength. Moreover, despite efforts using longer illumination wavelengths, increasing the imaging depth intrinsically increases the imaging time. There is therefore a need for an imaging modality providing fast, deep imaging at high resolution in a label-free manner.

---

[b] Lateral resolution
[c] Axial resolution
[d] Depending on the illumination wavelength

1.2 Optical Coherence Tomography and Microscopy

Optical coherence tomography [61] offers an interesting imaging modality for brain imaging, as it combines label-free imaging at very high acquisition rates. As we will demonstrate below, Fourier-Domain OCT (FD-OCT) acquires depth profiles of tissue back-scattering for each lateral position (so-called A-scans) without scanning the sample axially. As such, tissue information over large depths can be captured simultaneously, and volumetric imaging can be performed at very high speeds, compared to raster-scanning techniques such as 2PEF.

OCT was first implemented to provide non-invasive measurement of ocular structures [62] and has rapidly established itself as the gold-standard in ophthalmology for three-dimensional retinal imaging. Over the past 25 years, several technical advancements such as high speed line cameras, swept-sources and novel acquisition schemes (Fourier-Domain OCT, Doppler OCT and OCT angiography) have propelled OCT into other fields, such as oncology [63], dermatology [64], diabetes research [65] and neuroscience [66].

1.2.1 OCT theory

In order to understand how OCT performs three-dimensional imaging, we will first use a simplified model to describe how polychromatic light interacts and interferes to allow OCT imaging. Let's consider an Michelson interferometer composed of a sample arm and a reference arm, as shown in Fig. 1.2(a):
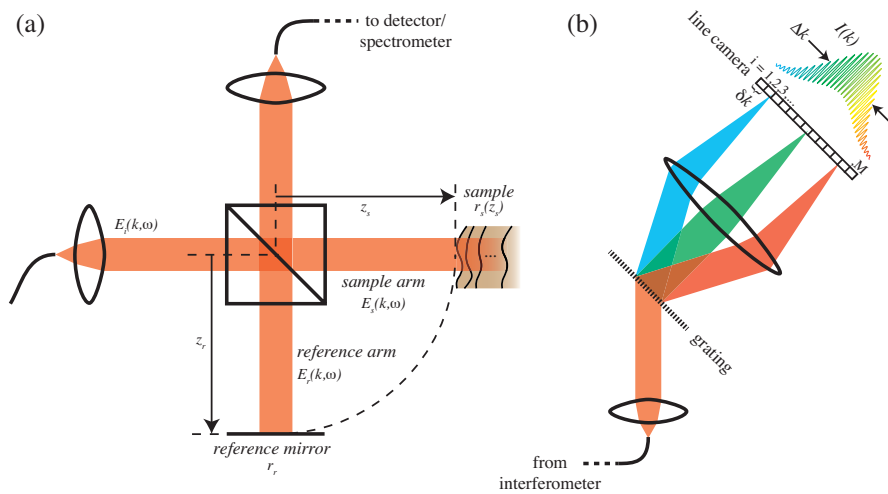

Figure 1.2 – Principles of OCT imaging: (a) OCT can be simplified to a Michelson interferometer, comprising a beamsplitter dividing a polychromatic optical wave $E_i(k,\omega)$ into a reference and sample fields. In the reference and the sample arms, a mirror with a reflectivity r_r and a sample with a reflectivity profile $r_s(z_s)$ reflect the light back into the interferometer respectively. Both waves reflected by the sample and the reference mirror are superimposed after passing through the beam splitter and interfere on the detector (or are sent to the spectrometer in FD-OCT). (b) In FD-OCT, a spectrometer is used to measure the interference spectrum between the light from the reference and the sample arm. A grating is used to spectrally separate the polychromatic light and the different wavelengths are then imaged on a line camera, composed of M pixels. Each pixel of the camera therefore measures a limited bandwidth δk. An FD-OCT system can be viewed as the combination of M distinct interferometers probing the overall interference pattern of a larger spectrum, with a bandwidth Δk.

The electric field $E_i(k,\omega)$ of polychromatic light entering the interferometer can be described as

follows:

$$E_i(k,\omega) = s(k,\omega) \cdot e^{i \cdot (k \cdot z - \omega \cdot t)}, \tag{1.1}$$

where k is the wavenumber defined as $k = {}^{2 \cdot \pi}/_{\lambda}$ and ω is the optical angular frequency, defined as $\omega = 2 \cdot \pi \cdot \nu$, where λ and ν is the light's wavelength and frequency respectively. The wavenumber and angular frequency dependent amplitude is modelled by the envelope $s(k,\omega)$. After passing through the beam splitter, the initial wave E_i is divided into two beams, E_r and E_s heading into the reference and sample arms of the interferometer, respectively:

$$E_s(k,\omega) = \frac{1}{\sqrt{2}} \cdot E_i(k,\omega) \tag{1.2}$$

$$E_r(k,\omega) = \frac{1}{\sqrt{2}} \cdot E_i(k,\omega) \tag{1.3}$$

As shown in Fig. 1.2(a), the reference arm comprises a single reflective surface (reference mirror) with a reflectivity r_r placed at z_r with respect to the beamsplitter. In the sample arm is placed a multi-layered reflective sample composed of N reflective surfaces with reflectivities r_{s_n}, and refractive indices n_{s_n} placed at depths z_{s_n} with respect to the first layer (positioned at a distance z_s from the beam-splitter). The optical path lengths (OPL) of each layer becomes $n_{s_n} \cdot z_{s_n}$. The *object function* $r_s(z_s)$, representing the sample reflectivity profile, can thus be obtained through a sum of N Dirac functions, weighed by their respective reflectivity r_{s_n} and delayed by their individual OPL difference $n_{s_n} \cdot z_{s_n}$. For this simplified calculation, the *object function* is therefore defined as:

$$r_s(z_s) = \sum_{n=1}^{N} r_{s_n} \cdot \delta(z_s - n_{s_n} \cdot z_{s_n}) \tag{1.4}$$

Upon reflection from the sample and the reference mirror, both fields head back towards the beamsplitter and their fields become:

$$
\begin{aligned}
E_s(k,\omega) &= \frac{1}{\sqrt{2}} \cdot E_i(k,\omega) \cdot \left[r_s(z_s) \otimes e^{i2kz_s} \right] \\
&= \frac{1}{\sqrt{2}} \cdot E_i(k,\omega) \cdot \sum_{n=1}^{N} r_{s_n} \cdot e^{i2k(z_s - n_{s_n} \cdot z_{s_n})}
\end{aligned}
\tag{1.5}
$$

$$E_r(k,\omega) = \frac{1}{\sqrt{2}} \cdot E_i(k,\omega) \cdot r_r \cdot e^{i2kz_r}, \tag{1.6}$$

where the symbol $\otimes$ denotes the convolution operator. After passing through the beamsplitter a second time, both fields superimpose and interfere on a photodetector. The intensity on this detector then

becomes:

$$I(k) = \frac{1}{2} \cdot \rho \cdot \left\langle |E_r + E_s|^2 \right\rangle, \tag{1.7}$$

where the $\langle\rangle$ symbol represents the temporal averaging of the photodetector (i.e. integration over the temporal resolution of the detector) and ρ is a factor converting the optical intensity into electrical current. Developing the right term in Eq. 1.7 gives:

$$\left\langle |E_r + E_s|^2 \right\rangle = \left\langle |E_r^2| \right\rangle + \left\langle |E_s^2| \right\rangle + \left\langle E_r E_s^* \right\rangle + \left\langle E_r^* E_s \right\rangle, \tag{1.8}$$

with the individual terms becoming:

$$\begin{aligned}
\left\langle |E_r^2| \right\rangle &= \frac{1}{2} \cdot \left\langle |s(k,\omega)^2| \right\rangle \cdot r_r^2 \\
&= \frac{1}{2} \cdot S(k) \cdot R_r \\
\left\langle |E_s^2| \right\rangle &= \frac{1}{2} \cdot S(k) \cdot |r_s(z_s)|^2 \\
&= \frac{1}{2} \cdot S(k) \cdot \left[\sum_{n=1}^{N} R_{s_n} + \ldots \right. \\
&\qquad \left. \sum_{n \neq m=1}^{N} \sqrt{R_{s_n} R_{s_m}} \cdot \left(e^{i \cdot 2 \cdot k \cdot (n_{s_n} \cdot z_{s_n} - n_{s_m} \cdot z_{s_m})} + e^{-i \cdot 2 \cdot k \cdot (n_{s_n} \cdot z_{s_n} - n_{s_m} \cdot z_{s_m})} \right) \right] \\
\left\langle |E_r E_s^*| \right\rangle &= \frac{1}{2} \cdot S(k) \cdot R_r \cdot \sum_{n=1}^{N} R_s(z_n) \cdot e^{i \cdot 2 \cdot k \cdot (z_r - (z_s - n_{s_n} \cdot z_{s_n}))} \\
\left\langle |E_r^* E_s| \right\rangle &= \frac{1}{2} \cdot S(k) \cdot R_r \cdot \sum_{n=1}^{N} R_s(z_n) \cdot e^{-i \cdot 2 \cdot k \cdot (z_r - (z_s - n_{s_n} \cdot z_{s_n}))},
\end{aligned}$$

$$\tag{1.9}$$
$$\tag{1.10}$$
$$\tag{1.11}$$
$$\tag{1.12}$$

where the squared temporally averaged amplitude $s(k,\omega)$ becomes $S(k)$, as only the signal within the limited temporal bandwidth of the detector is considered, and $R_{s_n} = r_{s_n}^2$ and $R_r = r_r^2$.

Combining these different terms into Eq. 1.8 and using Euler's relation $\cos(k \cdot z) = 1/2 \cdot \left(e^{i \cdot k \cdot z} + e^{-i \cdot k \cdot z} \right)$, we obtain:

$$\begin{aligned}
I(k) &= \frac{\rho}{4} \cdot \left[S(k) \cdot R_r + S(k) \cdot \sum_{n=1}^{N} R_{s_n} \right] + \ldots \\
&\quad \frac{\rho}{4} \cdot S(k) \cdot \sum_{n \neq m=1}^{N} \sqrt{R_{s_n} R_{s_m}} \cdot \cos(2 \cdot k \cdot (n_{s_n} \cdot z_{s_n} - n_{s_m} \cdot z_{s_m})) + \ldots \\
&\quad \frac{\rho}{2} \cdot S(k) \cdot \sum_{n=1}^{N} \sqrt{R_r R_{s_n}} \cdot \cos(2 \cdot k \cdot (z_r - (z_s - n_{s_n} \cdot z_{s_n})))
\end{aligned} \tag{1.13}$$

The intensity $I(k)$ is therefore the spectrum of the polychromatic light in the interferometer $S(k)$, with a constant intensity offset (first term in in Eq. 1.13) and two modulations. The offset combines the effects of the reflectivity of the reference mirror and an integrated reflectivity of the sample. The first modulation term in Eq. 1.13, called the auto-correlation term, originates from the interference between the different reflectors of the sample. The offset, also called DC term, contributes dominantly

to the intensity, as it depends directly on the reflectivity of the reference arm R_r. Conversely, the auto-correlation term, i.e. the inter-layer interference, is very weak and can be ignored provided the reference arm power is properly adjusted. Finally, the second modulation term is directly dependent on the distance between the reference arm and the depth position of the sample layers $z_r - (z_s - z_{s_n})$ and is proportional to the square root of product of the reference arm and the sample's reflectivity. This term therefore contains the *object function*. As the position $\Delta z = z_r - (z_s - z_{s_n})$ of the sample's layers with respect the reference arm length is the term driving the modulation of the second cosine in Eq. 1.13, performing an inverse Fourier transform of $I(k)$ would provide a depth profile, revealing the position of the sample's layers and their individual reflectivities:

$$
\begin{aligned}
\mathscr{F}^{-1}\{I(k)\}(z) &= \gamma(z) \otimes \left[\frac{\rho}{4} \cdot \left(R_r + \sum_{n=1}^{N} R_{s_n} \right) \right] + \ldots \\
&\quad \gamma(z) \otimes \left[\frac{\rho}{8} \cdot \left(\sum_{n \neq m=1}^{N} \sqrt{R_{s_n} R_{s_m}} \cdot \delta(z \pm 2 \cdot (n_{s_n} \cdot z_{s_n} - n_{s_m} \cdot z_{s_m})) \right) \right] + \ldots \\
&\quad \gamma(z) \otimes \left[\frac{\rho}{4} \cdot \left(\sum_{n=1}^{N} \sqrt{R_r R_{s_n}} \cdot \delta(z \pm 2 \cdot (z_r - (z_s - n_{s_n} \cdot z_{s_n}))) \right) \right] \\
&= i(z)
\end{aligned}
\tag{1.14}
$$

Through this Fourier transform, one obtains a function $i(z)^{\text{e}}$, containing the depth reflectivity profile $\sum_{n=1}^{N} \delta(z \pm 2 \cdot (z_r - (z_s - z_{s_n})))$ convolved with the Fourier transform of the spectrum $\mathscr{F}^{-1}\{S(k)\}(z) = \gamma(z)$, the *coherence function* of the light source, given by the Wiener-Khinchin theorem. The width of the *coherence function* $\gamma(z)$, called *coherence length* l_c, dictates the distance over which the light from the reference and sample arms will interfere: if the distance between the two surfaces is beyond the coherence length l_c, the electric fields will superimpose, but no interference will occur. From Eq. 1.14, it is clear that the *coherence length l_c*, will dictate the axial resolution of the OCT system, or the so-called *coherence gating*, which is inversely proportional to the bandwidth of the illumination spectrum. For a Gaussian-shaped spectrum, the axial resolution l_c is given by:

$$
l_c \approx 0.44 \cdot \frac{\lambda_c^2}{\Delta \lambda},
\tag{1.15}
$$

where λ_c is the central wavelength and $\Delta \lambda$ is the bandwidth of the illumination source.

In Fourier-domain OCT (FD-OCT), the interferogram $I(k)$ is directly recorded using a spectrometer, as presented in Fig. 1.2(b). A Fourier-transform is then performed on the modulated spectrum, after a background subtraction (to remove the DC component) and $\lambda \leftrightarrow k$ mapping, to obtain a depth profile of the reflectivity of the sample (A-scan). FD-OCT systems can be viewed as composed of M separate interferometers (where M is the number of pixels in the line camera) with an individual coherence functions $\Gamma(z)$, given by the bandwidth of each pixel of the spectrometer δk. As this bandwidth δk is much shorter than the overall bandwidth of the spectrum (more specifically, here $S(k)$ is the power spectral density), the coherence function $\Gamma(z)$ will reach a few millimetres. Overall, in FD-OCT

---

[e]In this simplified calculation, the phase of the interferogram is not considered. If a phase $\Delta\phi$ is added into the second cosine term of Eq. 1.13, the Fourier transform operation will generate a complex function, where the each δ terms will be multiplied by an complex exponential $e^{\pm i \cdot \Delta \phi}$. This complex OCT signal is also referred to as the OCT complex phasor. Moreover, if the spectrum $S(k)$ is an asymmetric function, its Fourier transform $\gamma(z)$ will also be a complex function.

systems, the axial resolution is dictated by the width of the coherence function of the source $\gamma(z)$ (i.e. the coherence length l_c), but by multiplexing the imaging in wavenumber, the interference between the reference and the sample arms will be measured over the width of the coherence function of each pixel $\Gamma(z)$, which is typically orders of magnitudes larger than the axial resolution l_c. A three-dimensional image of reflectance $i(x, y, z)$ can therefore be obtained by scanning the beam laterally in two dimensions, over x and y. In contrast to confocal and two-photon microscopy where the axial and lateral resolutions are coupled (through the NA of the objective), the axial resolution of OCT is solely dictated by the coherence length of the source and is therefore independent of the lateral resolution.
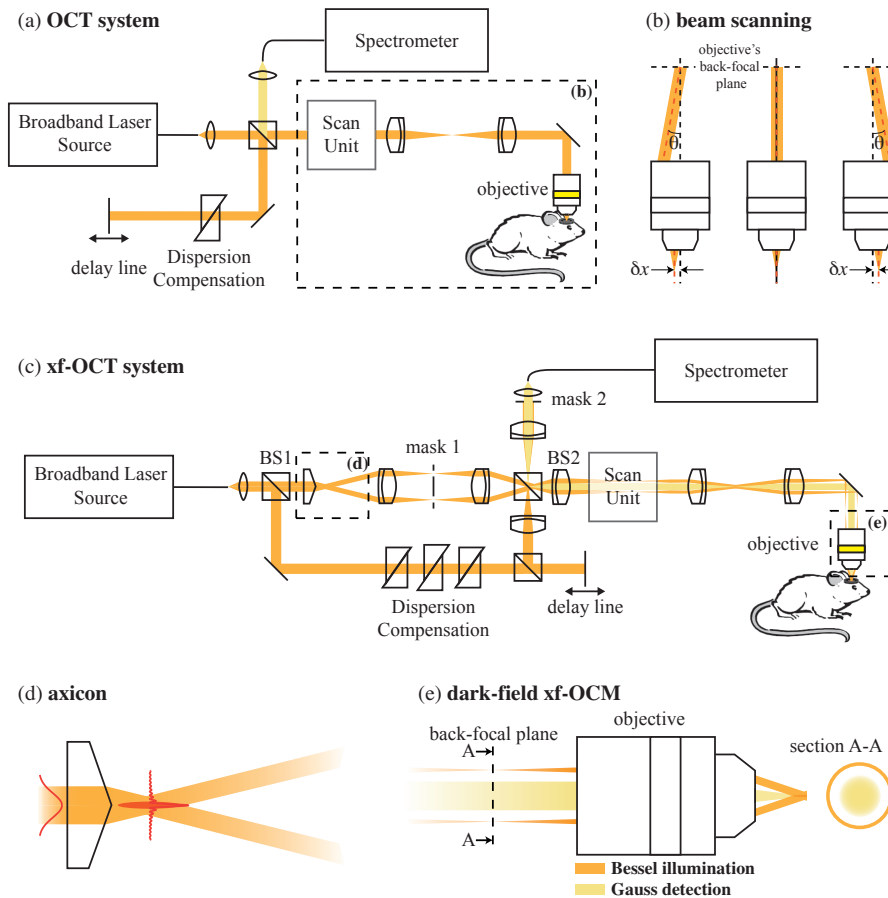
Figure 1.3 – OCT and xfOCT systems: (a) Conventional OCT systems typically are based on a Michelson interferometer, where a scan-unit and an objective are used to raster-scan the focal volume laterally over the sample. This beam scanning is usually performed by galvo mirrors, where the angle change θ at the back-focal plane of the objective will translate to a position change δx on the sample (b). (c) An extended-focus configuration can be obtained by combining a Bessel illumination and a Gaussian detection. This mode splitting implies changing the core of the microscope from a Michelson to a Mach-Zehnder interferometer. A Bessel-beam are typically produced by propagating an intial Gaussian beam through an axicon lens (d). A dark-field xf-OCT system implies spatially separating the Bessel illumination from the Gaussian detection in the back-focal plane of the objective. If there is no overlap between both modes, as shown in (e), specular reflections of the illumination on the sample will not be detected and a dark-field contrast will be obtained.

A typical OCT system is presented in Fig. 1.3(a), where the sample arm is composed of a pair of galvo scanners and an objective, to focus the light on the area of interest. As shown in Fig. 1.3(b), the

light is scanned over the sample laterally by varying its incidence angle at the back-focal plane of the objective. The typical lateral resolution of OCT systems varies between ~10 µm to 50 µm.

Optical coherence microscopy

In conventional optical imaging systems, the lateral resolution δr depends on the numerical aperture (NA) of the objective and the central wavelength λ_c of the illumination source as follows:

$$\delta r = 0.61 \cdot \frac{\lambda_c}{NA},$$

(1.16)

where the 0.61 factor depends on the metric used to measure the resolution (here the Rayleigh criterion) and also the optical system. Increasing the NA of a confocal system, which is the building block of an OCT system, typically results in a restriction of the depth-of-field (DOF), i.e. the depth over which light is collected, as shown in the following expression, relating the DOF, defined as the Rayleigh length z_r to the NA:

$$z_r \propto \pi \cdot \frac{\lambda_c}{NA^2},$$

(1.17)

This principle is exploited in confocal scanning microscopy to obtain depth-sectioning (confocal-gating). However, in FD-OCT, reducing this DOF can restrict the imaging depth below the available imaging depth of the spectrometer and penetration depth of light, and can ultimately hamper the multiplex advantage described previously. Consequently, at very high resolutions, optical coherence tomography systems (more commonly known as optical coherence microscopy, OCM [67]) require an additional scan of the sample along the optical axis to perform three-dimensional imaging. This additional scan can result in very long acquisition times (up to hours for a 3D image) and can require additional post-processing steps to reconstruct a volumetric image.

Extended-focus optical coherence microscopy

Overcoming the restricted DOF imposed by high NA objectives is possible by changing the beam type used to scan the sample. In OCT systems, the illumination and detection modes are typically Gaussian and therefore suffer from the decrease in DOF described above when the beam is focused into a tight beam waist (high resolution). An ideal beam for OCM imaging would therefore be a needle shaped beam, where the waist of the beam is constant and the energy equally distributed over depth [68]. Although such beams do not exist, a close approximation is found in Bessel beams [69], as shown in Fig 1.3(d). The needle-like shape of the focus of Bessel beams is formed by a cylindrically symmetric wave interference. In addition to their diffraction-less property, where the central lobe exhibits very little broadening in depth, the energy distribution and flow in such beams increase their robustness to obstructions along the propagation direction [70]. Briefly, each side lobe of a Bessel beam carries almost the same energy and is used to generate the central lobe later in the propagation of the beam. As such, the energy in the side rings is continuously transferred to the main lobe over time and small obstructions of this central lobe will be compensated for along the propagation direction by the energy in the side lobes from previous depths. Bessel beams can be generated through an SLM [71] or a conical lens, i.e. an axicon [72].

The first implementation of extended-focus optical coherence tomography (xf-OCT) was realised by replacing the systems' objective with such an axicon lens [72]. The system showed an increase in depth-of-field over conventional Gaussian beam systems, but its collection efficiency was very low, as Bessel beams form a ring in the back-aperture of the objective. A Bessel detection would thus collect only a small fraction of the back-scattered light. To overcome this detection inefficiency, Leitgeb et al. devised an extended-focus OCM (xf-OCM) system [73], similar to the setup presented in Fig. 1.3(c), by splitting the detection and illumination paths of the interferometer and used a Gaussian mode for the detection. This change in configuration reduces the extended-focus capability of the overall system, but increases its collection efficiency. Overall, a trade-off exists between a large depth-of-field and high photon collection. Extended-focus OCM has been used to image the islets of Langerhans in the pancreas [65, 74], amyloid plaques in alzheimeric mice models [75] and characterize mitochondrial dynamics in living cells [76].

dark-field Optical Coherence Microscopy

An additional advantage of using a Bessel illumination and a Gaussian detection is the ability to spatially separate both beams and obtain a dark-field contrast [77]. As mentioned previously, OCT measures changes in the refractive index of the sample under investigation and therefore collects the light reflected from any reflective surface. As such, imaging very thin structures placed on a highly reflective flat surface, such as cells on a glass coverslide, is a challenge in OCT, as the strong reflectivity of glass will fill a large portion of the dynamic range of the camera and ultimately drown the weak back-scattering of the cells. By spatially separating the Bessel illumination from the Gaussian detection in a conjugate plane of the back-aperture of the objective, as demonstrated in Fig. 1.3(e), the specular reflections of glass are not collected by the detection. The entire dynamic range of the camera can therefore be allocated to collect the weak back-scattering from the sample. Intrinsically, spatially filtering the reflected Bessel ring implies using a smaller detection NA. The resulting system, called dark-field OCM (df-OCM) has been successfully used to image cells placed on a coverslide and *ex-vivo* pancreatic tissue slices. Using a similar design than developed by Villiger et al., Blatter et al. constructed a low NA dark-field OCT (df-OCT) system in the infrared spectral range to image deep into skin [78].

Although not discussed in this thesis, the performance of OCT and xf-OCM systems can be described using coherent transfer functions (CTF). Moreover, CTFs are particularly well suited to highlight specific features of coherent systems, such as the dark-field property of the df-OCM platform. The calculation and interpretation of CTFs are discussed in detail in Villiger et al. [79].

1.2.2 OCT tools for brain imaging

Having discussed the physical principle behind image formation in OCT and the different implementations of xf-OCM, we will now list the different tools available in OCT to perform structural and functional brain imaging.

Intrinsic contrast

Contrast in OCT arises from variations in the refractive index of the sample under investigation [80]. Although non-specific, the back-scattering properties of individual components of tissue can provide an intrinsic contrast, which can be used to differentiate tissual structures. Using full-field OCM (FF-OCM),

Assayag et al. demonstrated the ability to discriminate between myelinated axons, blood vessels and neuronal cells in *ex-vivo* cerebral tissue through their back-scattering and morphology [81]. Tamborski et al. and Srinivasan et al. extended these observations and imaged the cortex of rodents *in-vivo* using OCM systems in the near-infrared [82] and infrared wavelength range [83]. Similarly to the results obtained in FF-OCM, myelinated axons and neurons appear as bright white lines and dark spheroids respectively. Further observations revealed the strong direction-dependency of myelin scattering, where fibers oriented orthogonally to the optical axis appeared brighter than parallel ones [84, 85]. In the mice cortex, Srinivasan et al. demonstrated that inducing anoxic depolarization (killing the neurons) changed the contrast of cells and effectively increased their backscattering. The initial darker contrast could therefore be attributed to cell viability. Possible explanations for this lack of scattering include the variation of refractive index within the cells being much smaller than those in the neuropil, or the spatial scale of these variations being too small to cause significant back-scattering. Interestingly, in fixed human tissue, Magain et al. observed neurons with an opposite contrast than in the previous observations of Assayag and Srinivasan, i.e. neurons appear as bright structures surrounded by a darker neuropil [86]. Additionally, Bolmont and Bouwens et al. demonstrated that amyloid plaques in alzheimeric mouse models are characterized by a stronger back-scattering than the neuropil, similarly to myelin fibers, and therefore can be observed in xf-OCM images [75]. Ultimately, these studies reveal the potential of OCM to image and resolve cerebral structures through their intrinsic contrast.

Overall, two main conditions are fundamental to fully exploit the intrinsic contrast of OCT. Firstly, the resolution of the OCT system should be sufficiently high to resolve fine structures within the tissue. At low resolution, features are blurred and the intensity of each voxel reflects the sum of the back-scattering of each structure within the coherence volume. Secondly, the illumination spectrum of the system must be selected so as to increase the contrast of the desired structure to be observed. Tissue typically exhibits a stronger back-scattering in the visible wavelength range [87]. In view of this, a general trend has emerged in recent years within the OCT community to shift the central wavelength λ_c of the illumination spectrum into the visible wavelength range. As discussed above, decreasing λ_c has the added benefit of increasing the axial and lateral resolutions (given the same bandwidth $\Delta\lambda$ and NA). The individual spectral signatures of endo- and exogenous contrast agents in the visible spectral range can be distinguished using a fine spectrometer, enabling spectroscopic OCT. Lichtenegger et al. constructed an OCM system in the visible wavelength range and used the spectral signatures of contrast agents to image amyloid plaques in the *ex-vivo* cerebral tissue of mice and humans [87]. Chong et al. and Chen et al. used a spectroscopic OCT system to quantify the oxygen saturation in blood vessels in the brain [88, 89].

OCT angiography

The OCT signal, at a given lateral and depth position, can be viewed as the sum of the back-scattered fields of the particles present in the coherence volume. The temporal state of these particles, i.e. whether they move or not, will be reflected in the temporal behaviour of the OCT signal and can be used to distinguish between two types of scatterers, static or dynamic [68]. In blood vessels, the main component of the back-scattering originates from RBCs, which are inherently dynamic. An RBC flowing through the focus will cause a fluctuation of the intensity, the phase and the overall field of OCT signal. As will be described later, motion along the optical axis will result in a deterministic Doppler phase shift (rotation of the complex OCT phasor over time), which can then be extracted to estimate the
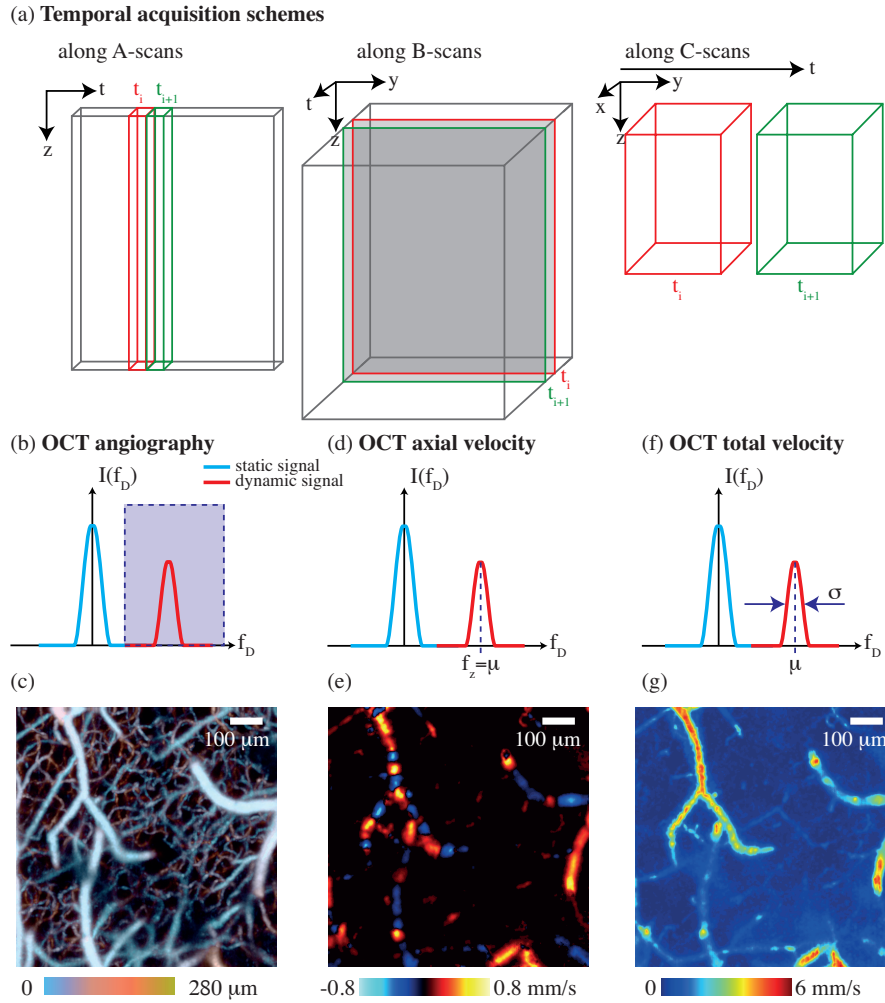
Figure 1.4 – Vascular imaging with OCT: Obtaining information on dynamic processes, whether contrast or velocimetric measurements, implies acquiring timetraces of OCT signals. Depending on the timescales of interest, these timetraces can be obtained either by oversampling along A-scans (axial depth profiles), along B-scans (2D planes of lateral position and depth) or along C-scans (volumetric images). (b) OCT angiography aims at selectively imaging vasculature from the sample (c). Such contrast is typically obtained through a high-pass filtering operation, where the static and dynamic components of the OCT signal are attenuated and amplified respectively. (d) The mean frequency μ of the Doppler spectrum $I(f_D)$ will provide an estimation of the axial velocity of RBCs in cortical blood vessels (e). Moreover, measuring the frequency spread σ and mean μ of this Doppler spectrum (f) will allow estimating their total velocity (g). Data taken from [90]

axial velocity of the RBC [91]. Other types of movements, such as tumbling or lateral movements of erythrocytes within the coherence volume will cause random fluctuations of the intensity and phase, resulting in a decorrelation of the OCT signal over time. Red blood cells have a highly orientation dependent scattering through their disk-like shape [92]. Small orientation changes could therefore cause large variations in the overall OCT signal (intensity and phase).

In tissue, the dynamic component of back-scattering is dominated by RBC motion (at the timescales of OCT imaging). As such, isolating the fluctuations in the OCT signal enables visualising the tissue's vasculature without the need for exogenous contrast agents, as illustrated in Fig. 1.4(b) and (c). Several scanning protocols and algorithms have been developed over the past decades to selectively enhance this motion contrast and perform so-called OCT angiography [93]. Three main classes of post-processing algorithms have been developed, by either analysing changes in the *amplitude*, *phase* or the *overall complex OCT* (also called *field-based*) signal over time. As illustrated in Fig. 1.4(a), OCT angiography protocols involve scanning schemes enabling timeseries to be acquired, either by oversampling along an A-scan (line) [94], a B-scan (plane) [95] or even a C-scan (volume) [96]. Speckle-variance based OCT angiography techniques $SV(x, y, z)$ discard the phase information of the OCT phasor and exploit the temporal variance of its intensity (speckle pattern) to enhance the motion contrast of vessels [97]:

$$SV(x, y, z) = \frac{1}{N} \cdot \sum_{t=0}^{(N-1) \cdot T} \left[\mathscr{I}(x, y, z, t) - \langle \mathscr{I}(x, y, z) \rangle \right]^2, \tag{1.18}$$

where N is the number of repeated acquisitions, T is the time lag between each frame and $\mathscr{I}(x, y, z, t)$ is the spatially and temporally resolved OCT signal intensity, defined as $\mathscr{I}(x, y, z, t) = |i(x, y, z, t)|^2$. In contrast, phase variance techniques $PV(x, y, z)$ exploit the phase variations caused by RBCs motion [98, 99]. The phase differences $\Delta\Phi(x, y, z, t)$ between two consecutive measurements are calculated and then used to estimate the phase variance over time.

$$PV(x, y, z) = \frac{1}{N-1} \cdot \sum_{t=0}^{(N-2) \cdot T} \left[\Delta\Phi(x, y, z, t) - \langle \Delta\Phi(x, y, z) \rangle \right]^2, \tag{1.19}$$

where the sum is performed on $N-1$ acquisitions, as at least two subsequent phasors are necessary to obtain the phase difference $\Delta\Phi(x, y, z, t)$. As the phase is particularly sensitive to small motions artefacts, conventional phase variance methods, as shown in equation 1.19 require an initial phase bulk motion correction. An alternative method presented by Vakoc et al. [63] uses circular statistics and performs the variance operation along the spatial dimension to cancel the effect of bulk axial motion. As the axial motion will affect each phase difference along depth with the same phase offset, it will not influence the variance. Moreover, their implementation of phase-variance weights the phase difference by the local OCT amplitude to alleviate the impact of the high phase noise of low scattering regions.

Finally, field-based OCT angiography protocols $A(x, y, z)$ use the overall phasor and act as a high-pass temporal filtering on the complex OCT signal timetraces [95, 94, 100]. These techniques are sensitive to fluctuations originating from both the intensity and the phase. A typical implementation of the high-pass filtering operation is through a complex subtraction over different temporal acquisitions,

as shown here:

$$A(x, y, z) = \frac{1}{N} \cdot \sum_{t=0}^{(N-1)\cdot T} |i(x, y, z, t+T) - i(x, y, z, t)|^2 \qquad (1.20)$$

Similarly to phase variance protocols, corrections for bulk motion artefacts are typically necessary prior to performing the high-pass filtering. Although the performance of each protocol varies depending on the phase stability of the system, the sample fixation and other parameters, each technique has its own advantages and disadvantages. Phase variance requires a good phase stability, but does not require any additional normalization steps to account for the decrease in depth of the OCT intensity and can be made insensitive to axial bulk phase motions. Conversely, and as will be discussed later, the signal in the field-sensitive algorithms has been shown to reflect the concentration of moving particles, which could be used as a measurement of relative hematocrit [101]. A lushness of variations of the techniques presented in equations 1.18, 1.19 and 1.20 have been developed over the years, involving different averaging methods (along the spatial [102], temporal [103] or spectral dimensions [104]), normalization steps and more sophisticated filtering operations (e.g. temporal correlations) [93]. In the journal articles presented in this thesis, angiograms were obtained using a complex subtraction (field-based angiography) [95]. OCT angiography is an ever growing field and angiographic protocols described above has been used in ophtalmology [105], oncology [63] and neuroscience to image and quantify changes in the vascular bed throughout diseases [106].

OCT velocimetry

In addition to angiography, offering a mean to selective visualize vessels qualitatively, OCT can perform velocimetric measurements of the speed of particles flowing through the focal volume. Over the past decades, several different techniques have been developed to measure the velocity of blood in tissue in a quantitative manner.

Doppler OCT

Doppler optical coherence tomography (DOCT) [91] can perform spatially resolved velocity measurements by exploiting the Doppler shift of the light back-scattered by moving scatterers (Fig. 1.5(a)). To illustrate the calculation of the velocity, let's consider the effect of a mirror moving on the interferogram over time $I(k, t)$. By simplifying the expression of $I(k)$ from Eq. 1.8 and adding a time-varying position of the mirror in the sample arm $z(t)$ with a refractive index n, we obtain:

$$I(k, t) = S(k) \cdot \cos(2 \cdot k \cdot n \cdot z(t)) \qquad (1.21)$$

By replacing $z(t) = z_0 + \delta z(t) = z_0 + v_z \cdot t$:

$$
\begin{aligned}
I(k, t) &= S(k) \cdot \cos(2 \cdot k \cdot n \cdot (z_0 + v_z \cdot t)) & (1.22)\\
&= S(k) \cdot \cos(2 \cdot k \cdot n \cdot z_0 + n \cdot \omega_z \cdot t), & (1.23)
\end{aligned}
$$

where v_z is the axial speed of the sample mirror, z_0 is its initial axial position and $\omega_z = 2 \cdot v_z \cdot k$ is the beating frequency (also called Doppler beating). Equation 1.24 highlights the time-dependency of the fringes of the spectrum and shows that moving the axial position of the sample's mirror with a constant speed will cause the modulation frequency of the interferogram to change linearly in time. Alternatively, if the OCT signal $i(z, t)$ is viewed as a complex phasor, the effect of a moving the mirror along the optical axis with constant speed will result in a rotation of the phasor in the complex plane with an angular speed given by the Doppler beating ω_z.

By acquiring multiple interferograms in time, it is possible to deduce the axial speed of the mirror by extracting the phase difference between the different acquisitions. At time $t = t_0 + T$, where T is the time lag between two acquisitions, the interferogram will become:

$$
\begin{aligned}
I(k, t \mid t = t_0 + T) &= S(k) \cdot \cos(2 \cdot k \cdot n \cdot z_0 + n \cdot \omega_z \cdot (t_0 + T)) & (1.24)\\
&= S(k) \cdot \cos(2 \cdot k \cdot n \cdot z_0 + n \cdot \omega_z \cdot t_0 + \Delta\phi)) & (1.25)
\end{aligned}
$$

Where $\Delta\phi$ is the phase difference between the two acquisitions, and if extracted, can be used to calculate the speed as follows:

$$
\Delta\phi = n \cdot \omega_z \cdot T = 2 \cdot n \cdot v_z \cdot k \cdot T = v_z \cdot T \cdot \frac{4 \cdot \pi \cdot n}{\lambda}, \tag{1.26}
$$

where λ is the central wavelength of the source. Extracting the velocity from the phase difference $\Delta\phi$ can be performed through various means, e.g. by using a Kasai estimator [66] or by using an auto-correlation algorithm [107]. Another way of calculating the speed of the mirror v_z is to calculate the Doppler frequency spectrum of the interferogram by means of a Fourier transform along the temporal dimension (Fig. 1.4(d) and (e)). The mean frequency of this temporal frequency spectrum will then be:

$$
f_z = \frac{\omega_z \cdot n}{2 \cdot \pi} = \frac{2 \cdot v_z \cdot k \cdot n}{2 \cdot \pi} = \frac{n \cdot k}{\pi} \cdot v_z \tag{1.27}
$$

This method, termed joint Spectral and Time-Domain OCT (jSTdOCT) was developed by Szkulmowski et al. and applied to quantify axial flow in the retina [108]. Overall, the jSTdOCT formalism requires two independent Fourier transforms along the spectral and temporal dimensions to obtain depth-resolved Doppler spectras of the sample. The mean frequency f_z is then estimated either through the maximum [108] of the Doppler spectrum or through circular statistics [109]. As will be shown in the next section, this additional Fourier transform will be required to estimate the total velocity of blood.

Quantitative blood flow OCT

In biological tissue and especially in the cerebral cortex, a large portion of the vascular network is oriented parallel to the tissue surface and therefore perpendicularly to the optical axis [110]. As shown in Fig. 1.5(b), the axial velocity component of moving RBCs in these vessels will be null (or very low) and will ultimately not be measurable with DOCT [93]. Moreover, to obtain an estimation of the absolute blood velocity (amplitude of the total velocity vector), a measurement of the orientation of the vessels is necessary [111]. Although modifications can be made to the optical system to measure

almost directly the absolute velocity (i.e. through three-beams configurations [112]) and algorithms have been developed for angular correction [111, 113], these strategies involve either cumbersome post-processing steps or complex imaging systems. Interestingly, the lateral component of the velocity vector (i.e. in the plane of imaging) can be estimated by measuring the spread in the Doppler frequency spectrum [84, 114, 115]. Conceptually, this can be explained by the fact that light impinging on the moving scatterer and then back-scattered has a certain angular spread (dictated by the NA of the objective) and will therefore probe different projections of the velocity vector of the moving particle, as illustrated in Fig. 1.5(c) and (d). This angular spread will result in different Doppler shifts and ultimately will widen the Doppler spectrum. Wavevectors at the edges of the angular spread will therefore experience a Doppler shift reflecting a combination of the axial and lateral components of the velocity vector, whereas wavevectors at the center of the angular spread (i.e. parallel to the optical axis) will only be shifted by motion along the optical axis. Consequently, the illumination and detection modes (which define the angular spread for the illumination and detection) will influence the overall shape of the Doppler spectrum [109]. To account for this effect, Bouwens et al. derived an analytical framework allowing to estimate the lateral and axial velocity components of moving scatterers, taking into account the illumination and detection modes of the OCT system [109]. For an extended-focus configuration, Bouwens et al. showed that the mean $\mu[f_D]$ and the spread $\sigma[f_D]$ of the Doppler frequency spectrum are related to the transverse and axial velocity projections, v_t and v_z, as follows [109]:

$$\mu[f_D] \approx \frac{n \cdot k_0}{\pi} \cdot v_z \tag{1.28}$$

and

$$\sigma[f_D] \approx \frac{A}{2} \cdot \frac{n^2 \cdot k_0^2}{4 \cdot \pi^2 \cdot f^2} \cdot v_t^2 + \frac{n^2 \cdot k_\sigma^2}{\pi^2} \cdot v_z^2, \tag{1.29}$$

where n is the refractive index of tissue, k_0 and k_σ are the source's central wavenumber and its standard deviation respectively, f is the focal length of the objective and A is a parameter defined by the illumination and detection modes. As expected, the axial velocity estimation presented in Eq. 1.28 is identical to the result from the jSTdOCT algorithm of Eq. 1.27.

In practice, total blood flow measurements are performed by temporally oversampling each lateral position (typically 32 to 64 time points per position). A timetrace of OCT signal is therefore obtained for each voxel of the imaging volume which can be Fourier transformed to obtain a depth resolved Doppler frequency spectrum (jSTdOCT method). Each spectra are then fit using a modified Gaussian function from which the width and the frequency are finally extracted and converted into the lateral and axial velocity projections, using Eq. 1.28 and 1.29. As such, measuring the mean frequency and spread of the Doppler frequency spectrum enables retrieving the total velocity of blood, as illustrated in Fig. 1.5 (f) and (g).

An alternative way of obtaining quantitative blood flow measurements was devised by Lee et al. using concepts from dynamic light scattering [116]. Their technique, called dynamic light scattering OCT (DLS-OCT) calculates and fits the autocorrelation function of OCT signal to obtain an estimation of the axial and lateral projections of velocity and diffusion parameters. DLS-OCT was applied to

calculate the velocity of blood in large vessels of the cortex of rats and to measure diffusion in neurons [117].
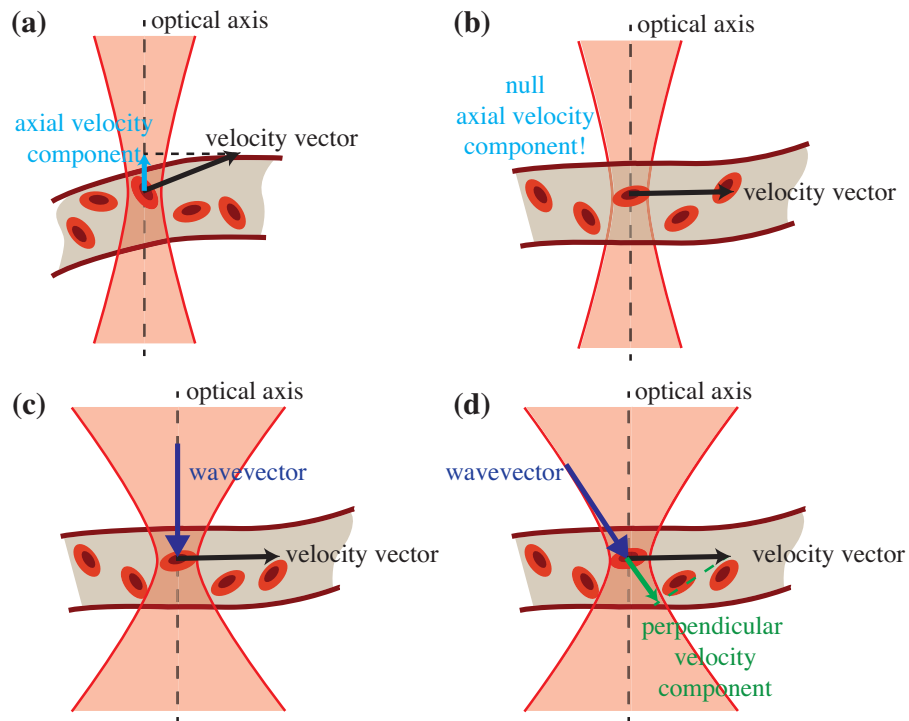

Figure 1.5 – Illustration of total blood flow estimation with Doppler OCT. (a) The axial velocity projection of RBCs moving through vessels will cause the incident and reflected light to experience a Doppler shift. In cases where RBC motion is parallel to the optical axis, light along the optical axis will not experience any Doppler shift (b). As such, when the light's wavevector is perpendicular to the velocity vector of RBCs, no Doppler shift will occur (c). However, through the system's NA, not all wavevectors will be parallel to the optical axis, such wavevectors will impinge at different angles on RBCs and will therefore experience a Doppler shift even if the RBC flows perpendicularly to the optical axis (d).

Capillary velocimetry

The vascular network is composed of several vessel calibers having very different flowing characteristics. In capillaries, red blood cells typically flow at very low speeds (0.1 to 2 mm/s) and one by one [110], in a discrete fashion, with sometimes very low linear hematocrits (very large time differences between each red blood cells as shown in Fig. 1.6(a)). As mentioned previously, Doppler OCT measures the Doppler beating ω_z between light back-scattered from a moving erythrocyte and a static reference. In practice, multiple time points are necessary to record this beating and calculate the velocity of the moving scatterers (to either estimate the phase differences $\Delta\phi$ or the Doppler frequency spectrum accurately). In the case of capillaries, the discrete nature of red blood cell flow can bias these measurements, as the Doppler beating will be not measured in a continuous fashion (it will only be measurable when a red blood cell flows through the focus). In view of these limitations, several different strategies have been developed to measure the velocity of RBCs in capillaries. Lee et al. took advantage of this discrete RBC flow to calculate the RBC linear density, speed and flux (number of RBC per second) [118]. As illustrated in Fig. 1.6(b), their strategy is based on the observation that as RBCs flow one-by-one in capillaries, the

OCT intensity would also be pseudo-discrete, i.e. showing peaks in intensity reflecting the passage of a RBC (the plasma does not reflect any light, whereas RBC are highly reflecting particles). The technique is similar to capillary velocimetric techniques used in 2PEF microscopy [55] (see 1.1.3), wherein vessels are filled with a fluorescent dye and red blood cells appear as dark dots in the angiograms. If the temporal and spatial sampling are sufficiently fine, the speed of the RBC can be derived from the temporal extent of these intensity peaks in the timetraces [119], by assuming a fixed RBC diameter, as shown in Fig. 1.6. In practice, each peak in the timetraces is fit with a Gaussian function with 3 free parameters, the amplitude, spread and a constant offset. The speed of the RBC is then determined through the ratio of the size of the RBC (and other optical parameters) and the spread of the fitted Gaussian (in seconds). Ren et al. devised a similar strategy based on the observation of transients in the phase of the Doppler OCT signal instead of the OCT intensity to detect the passage of RBCs [120]. A slightly more invasive alternative, developed by Pan et al. [121], involves an injection of a highly scattering contrast agent, e.g. intralipid, to make the scattering temporally constant even in capillaries and thus render the Doppler beating continuous (Fig. 1.6(c)). Additionally, the intravenous injection of intralipid also increases the contrast in angiograms and could also be used to quantify other hemodynamic parameters, such as transit time distributions [122]. Alternatively, in an general effort to make OCT angiography a quantitative tool, Choi et al. derived an analytical model of optical micro-angiography (OMAG) [101], a *field*-based angiography technique (see 1.2.2), to characterize the relationship between the OMAG signal and blood velocity and concentration. They demonstrated that at low B-scan rates, the OMAG signal mainly reflects changes in concentration, whereas at very short times between frames, the OMAG signal is driven both by the velocity and the concentration of the moving scatterers. Finally, Tang et al. developed an optimized Doppler OCT protocol with a very dense temporal oversampling (800 time samples per position) to account for the discrete RBC flow [123]. As the PSF of OCT systems is typically of the size of capillaries or larger, the velocity measured might reflect the contribution of both moving RBCs and static tissue in the same imaging volume (as illustrated in Fig. 1.6(d) and (e)). To circumvent this potential bias, Tang et al. added a high-pass filtering step prior to the estimation of the phase of the OCT signal, and then used a histogram to measure the RBC's axial velocity. Their technique was then used to obtain the axial velocity projection of RBC speed in the entire cortical column of a mouse, by shifting the focus in depth.

1.2.3 Applications of OCT in brain imaging

Using the various tools defined above, OCT is increasingly being used to study brain structure and function. An exhaustive review of every single paper involving OCT imaging to study the brain would be out of the scope of this thesis, so we will focus on two main applications of interest: *functional hyperaemia* and *structural brain mapping*.

Functional hyperaemia

As explained in the introduction, the energy consumption following neuronal firing is typically countered by a local increase in blood flow. Although fMRI and 2PEF have revolutionized our understanding of these processes by shedding light on several aspects of the mechanisms underlying functional hyperaemia, these techniques are limited by either the nature of their contrast (i.e. BOLD signal), by their resolution, acquisition speeds or penetration depths.

OCT is an ideal tool to study functional hyperaemia, as the hemodynamic activity over an entire
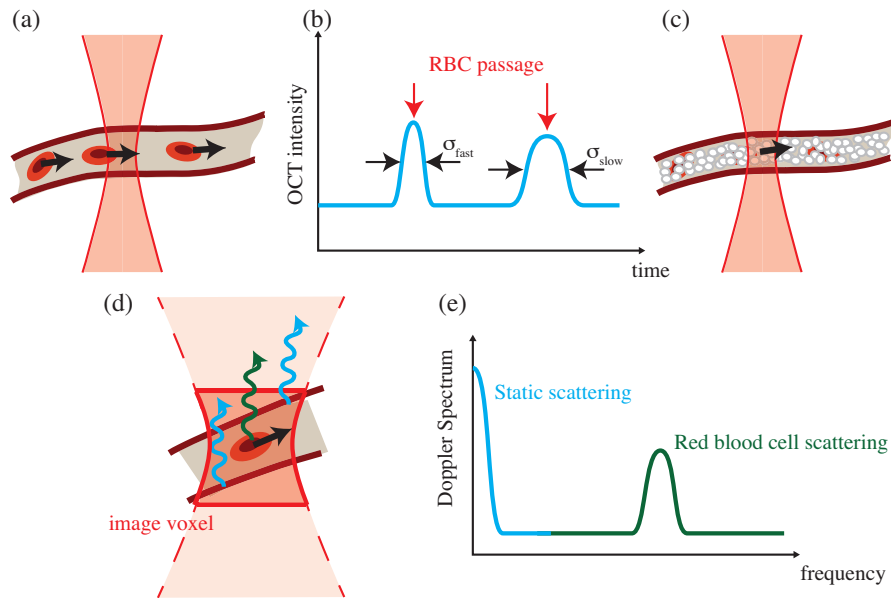
Figure 1.6 – Alternative velocimetric OCT metrics: (a) RBCs typically flow one-by-one in capillaries and will produce an increase in the intensity of the OCT signal as they flow through the system's focal volume (b). The temporal width σ_{RBC} of these intensity peaks will provide information on the RBC speed. (c) To counter the discrete nature of capillary flow and produce constant scattering in time, a scattering solution can be injected into the blood stream. (d) As the resolution of OCT systems can be larger than the size of a capillary, the overall OCT intensity will reflect the contribution from the static tissue and moving RBCs present within the image voxel. (e) The frequency spectrum of the OCT signal will therefore contain a DC component, from the static scattering, and an AC component caused by the dynamic scattering of the RBC.

cortical depth can be monitored simultaneously through its high speed, minimal invasiveness and large penetration depths. Using the concepts of OCT angiography illustrated in 1.2.2, Radhakrishnan et al. devised a metric to estimate the concentration of RBC in blood [124]. Briefly, as mentioned previously, the dynamic component of the OCT signal can be shown to reflect the concentration of moving particles, i.e. red blood cells. However, similarly to the OCT signal itself, the dynamic component is affected by other parameters, such as the OCT's roll-off, the confocal gating and the attenuation of light in depth. As both the static and dynamic components experience these properties identically, normalizing the dynamic signal with the static component would result in a metric independent of the system's imaging parameters and reflecting only the concentration of RBCs. Alleviating the influence of light attenuation on the dynamic signal is of tremendous importance as the latter has been shown to increase during functional hyperaemia (by increases in blood volume at more superficial depths) [125]. This change in attenuation will thus affect the OCT intensity at deeper layers, and will not reflect the hemodynamic activity of the voxel of interest. Normalizing the dynamic signal thus provides a depth-resolved metric of dynamic RBC content, unaffected by the activity of overlaying vascular structures. Using this so-called dynamic RBC concentration metric in combination with RBC capillary velocimetry, Srinivasan et al. investigated the laminar characteristics of blood flow dynamics during functional hyperaemia [126]. Similarly to results obtained in fMRI, OCT angiography revealed that the strongest and fastest rise in blood flow occurred in layer IV of the cortex [12], followed later by the rest of the layers. Moreover, they observed a temporal mismatch between the dynamics of RBC content and RBC speed (which can be thought of a mismatch between CBV and CBF).

Using a similar metric, termed statistical intensity variation (SIV) [127], and a segmentation of the vascular network, Lee et al. analysed the hemodynamic activity of a large region of the microvascular network [128]. Recent studies by Rasmussen et al. have highlighted the importance of flow pattern distributions of the microvascular network in dealing with oxygen delivery [129]. More specifically, increasing the variance in the transit time of blood through the capillary network results in a more efficient delivery of oxygen to tissue. In view of these results, Lee et al. imaged the hemodynamic response of a large capillary bed [128], performed a segmentation to obtain a hemodynamic time trace per capillary segment and analysed the variance of the signal across the different vessels. Their investigation revealed an increase in the variance in the hemodynamic activity of the vascular network *prior* to the rise of blood flow caused by the neural activity. This observation hints to the existence of an active flow regulation system at the capillary level, e.g. through pericytes [130, 131]. Overall, these studies highlight the suitability of OCT as a high resolution counterpart of fMRI, enabling capturing at high acquisiton rates hemodynamic processes occuring at the capillary level. Moreover, the abundant tools devised for OCT (some of which were presented in 1.2.2) provide the opportunity to capture and separate the different hemodynamic contributions to functional hyperaemia and delineate alterations in the neurovascular coupling caused by diseases [132].

Structural brain mapping

In parallel to efforts in providing functional maps of the brain, there has been a growing interest in performing large scale histology of human and rodent brains, in an attempt to match structure with function and unveil morphological alterations caused by neurodegenerative diseases. Several optical techniques have been adapted to perform whole-brain histological imaging [133], such as wide-field fluorescence imaging and two-photon microscopy [134], by coupling the optical system to a

mechanised tissue slicer, i.e. a vibratome. Although serial wide-field fluorescence-based techniques provide specificity and enable distinguishing between several cell types and tissue structures, obtaining three-dimensional high resolution images requires very thin tissue slices [133], which can create severe distortions in tissue. Two-photon microscopy relaxes this constraint through its axial sectioning capabilities and its penetration depth of a few hundreds of microns, which can be further increased using tissue clearing techniques [135]. However, scanning the two-photon excitation beam across the lateral and axial dimensions can result in extremely long acquisitions times. Overall, the combined effects of chemical alterations caused by the clearing, staining and tissue dehydration and physical distortions from the slicing can encumber attempts at registrating and validating these results with other modalities (such as MRI or standard histology) [136].

In view of these technical limitations, OCT can provide an interesting alternative for structural brain imaging. Through its depth multiplexing capabilities, OCT can decrease the overall acquisition times compared to confocal and two-photon microscopy. Moreover, as large penetration depths can be reached with OCT in the infrared spectral range (up to ~1.5 mm in brain tissue [83]), thicker tissue slices can be cut, resulting in less physical distortions. Finally, OCT is a label-free imaging technique and does not require tissue staining. This latter point implies that OCT does not provide the specificity of fluorescence imaging, however, as described earlier, the back-scattering properties of tissue can offer an intrinsic contrast, enabling identifying myelinated axons and neurons. Moreover, a plethora of additional tools can be used to discriminate between brain structures and provide additional functional information [137, 138, 139, 140, 141]. The attenuation coefficient of light in brain images has been shown to enable differentiating between different brain regions, typically between white and grey matter, and provides a contrast similar to Nissl staining [136]. Fibers also provide a different reflectivity depending on their orientation and can therefore be tracked [138]. Moreover, combining these metrics and polarization sensitive OCT, Wang et al. were able to perform structure tensor imaging (similarly to diffusion tensor MRI) to map the orientation of myelinated fibers, with the goal of providing connectome information at high microscopic resolution [137, 141].

1.3 Thesis objectives

The overall aim of this thesis is to present extended-focus optical coherence tomography and microscopy as valuable tools for studying cerebral structure and function. Despite the increasing interest for OCT in brain applications, fundamental technical limitations, such as the loss of lateral resolution in depth, hamper the efficacy of the technique and lead to long measurement times and potential inaccuracies in functional measurements. As such, this thesis focuses on presenting novel implementations of xf-OCT and xf-OCM for specific applications, i.e. high-resolution imaging, functional imaging of cerebral reactivity and deep cortical imaging.

The second chapter of this thesis focuses on demonstrating the capabilities of extended-focus OCM for *functional* imaging, motivated by an effort to translate some of the statistical tools devised for fMRI into microscopic brain imaging and measure quantitative velocity changes occurring in the brain. The total blood velocity ability of OCT, along with the depth extension advantage of xf-OCM, were used to track the stimuli-evoked velocity changes occurring in cortical vessels during functional hyperaemia. Neuronal activation was obtained through an electrical stimulation of the hind paw of a mouse placed under the microscope. After having acquired these velocity timetraces, a powerful statistical framework

of fMRI, called the general linear model (GLM), was applied to highlight the level of correlation between the recorded vascular activity and the stimulation paradigm, resulting in capillary-level, depth-resolved statistical parametric maps of vascular reactivity.

Two main trends currently dictate the development of novel OCT systems for brain imaging, high resolution and deep tissue penetration. Efforts in high resolution imaging are primarily driven by the desire to understand brain function at the cellular level. In view of this, the third chapter presents a novel high-resolution extended-focus OCM system combining a high NA objective with a large bandwidth spectrum centred in the visible wavelength range, termed visOCM. As will be described in Chapter 3, the visOCM system possesses a lateral resolution of 0.4 µm maintained over 40 µm in depth, and an axial resolution of 0.69 µm. Obtaining such characteristics required devising strategies for finely balancing the dispersion in the system, which are discussed in the journal article. The system's compatibility for brain mapping was assessed by imaging fixed brain slices of healthy and alzheimeric mice.

Chapter 4 is a direct extension of the work on the visOCM, where the system was modified to perform *in-vivo* imaging of cortical structures. The resolution of the system was reduced to obtain a depth of field matching the penetration depth of light in cortical tissue. Through the high resolution and increased contrast offered by the visible illumination spectrum, several features could be visualized in the first layers of the cortex, such as myelinated axons, capillary vessels and even layer II/III neurons, *in-vivo*.

The fifth chapter of this thesis treats the second major trend in OCT for brain applications: deep tissue imaging. Studying cortical function requires imaging throughout the entire depth of the cortex (i.e. ~ 1-1.5 mm in mice). To this end, novel OCT systems have been designed operating at longer central wavelength illumination (1.3 µm and beyond) or using novel sources, limiting the impact of system parameters, such as roll-off. Despite these efforts, xf-OCM systems designed for brain applications still operate at short central wavelengths and thus are limited in penetration depth. Chapter 5 presents a novel xf-OCT optimized for deep cortical imaging. It combines the larger penetration capabilities of light in the infrared spectral range (1.3 µm) with the diffraction-less properties of Bessel beams to provide capillary-level imaging over the entire cortical depth. As sources in this wavelength range typically offer little power relative to typical sources used for xf-OCM imaging at 800 nm, the design of this novel system was optimized to minimize power losses and improve the illumination's efficiency.

Finally, chapter 6 presents a few images that were obtained throughout this thesis that were unfortunately never published.

2 | Imaging of functional hyperaemia with extended-focus OCM

MAPPING OF BRAIN FUNCTION involves recording changes in neuronal and/or cerebral vascular activity occurring during the execution of a given task (e.g. grabbing task) or during a specific stimulation protocols (e.g. visual, auditory, olfactory etc...), in a minimally-invasive fashion. Such paradigms have revealed the presence of salient features of the functional organisation of the brain, such as the retinotopic [142, 143] and tonotopic [144] organisations of the human visual and auditory cortices respectively. Although neuronal activity provides ground-truth mapping of cerebral function, non-invasive electrophysiological methods such as EEG have very low spatial resolutions and are limited to two-dimensional projections. Alternatively, as neuronal processing is typically accompanied by local changes in blood flow, volume and oxygenation, hemodynamic measurements can provide a proxy for cerebral activity. Brain mapping with MRI relies on these local changes in blood oxygenation and cerebral blood volume to map regions involved in the processing of sensory or cognitive information [145]. Over the past decades, powerful processing tools have been devised to extract these subtle hemodynamic changes and locate regions of increased neuronal activity [146]. The statistical parametric mapping (SPM) framework encompasses pre-processing steps for image normalization and registration of fMRI data and statistical tools to analyse and identify voxels with increased activity related to the task or stimulation protocol [146]. This latter analysis is typically performed using the general linear model (GLM), wherein the voxel's activity is modelled as a linear combination of a set of regressors including hemodynamic changes and additional components (e.g. non-task-related signal drifts, changes in field strength, ...). The primary regressor used in GLM models the change of BOLD signal during the stimulation presentation period of the experiment's protocol. In practice, this regressor is obtained by convolving a so-called *hemodynamic response function* (HRF) with a binary representation of the experimental paradigm $N(t)$, whose value is 0 and 1 when the stimulation is off and on, respectively (boxcar function).

$$N(t) = \begin{cases} 1, & \text{if } t_{stim_{start}} < t < t_{stim_{end}} \\ 0, & \text{otherwise,} \end{cases} \tag{2.1}$$

where $t_{stim_{start}}$ and $t_{stim_{end}}$ are the start and end times of the stimulation presentation, respectively. Under assumptions of linearity, the HRF can be viewed as the impulse hemodynamic response of the

brain, i.e. the BOLD response measured for an extremely short stimulation event. For BOLD fMRI, the HRF shows a rapid initial rise, followed by a prolonged decay, as shown in Fig. 2.1(a), and is typically obtained using a Gamma function:

$$HRF(t; T_0, n, \lambda) = \frac{(t - T_0)^{n-1}}{\lambda^n \cdot (n-1)!} \cdot e^{-\frac{t-T_0}{\lambda}}, \tag{2.2}$$

where T_0 characterizes the time delay between the stimulation onset and the BOLD response, and n and λ determine its overall shape. Alternatively, modelling more complex characteristics of the BOLD response, as the initial dip or post-stimulus undershoot, can be achieved through a difference of Gamma functions, instead of a single function. The first regressor $X_1(t)$ is therefore obtained by convolving $HRF(t)$ with $N(t)$:

$$X_1(t) = HRF(t) \otimes N(t), \tag{2.3}$$

where $\otimes$ denotes the convolution operator. An illustration of the result of this operation is shown in Fig. 2.1(b).
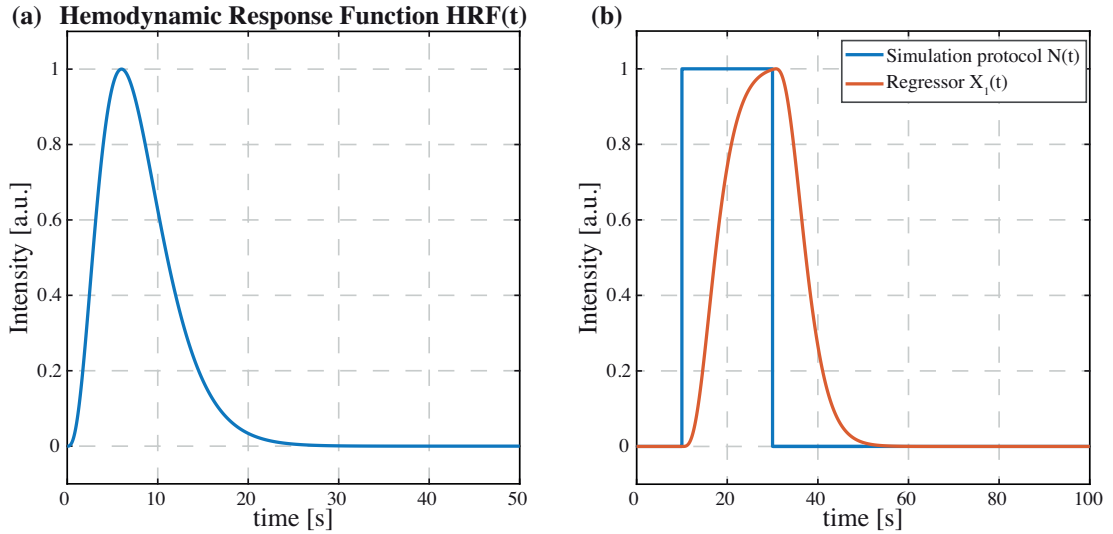

Figure 2.1 – Illustration of the general linear model: (a) The hemodynamic response function is modelled as a fast rise of signal followed by a slow decay. It can be viewed as the impulse hemodynamic response to neural activity. (b) As such, to predict the evoked BOLD response measured during the execution of a task $X_1(t)$ (orange curve), the HRF is convolved with the stimulation paradigm $N(t)$, shown in blue.

Additional regressors $X_i(t)$ can be added to the regressor set $X = [X_1(t), X_2(t), \ldots, X_N(t)]$ to model more complex response dynamics (e.g. such as time lags and spreads, through the first and second temporal derivatives of the $HRF(t)$) or to account for system parameters (DC component of signal, field strength drift, ...). The BOLD activity of a single voxel $y(t)$ is then modelled as a linear combination of

the regressors and a noise component $\epsilon(t)$:

$$y(t) = \sum_{i=1}^{N} \left(X_i(t) \cdot \beta_i \right) + \epsilon(t), \tag{2.4}$$

where β_i is the weight corresponding to the regressor $X_i(t)$ and its estimate $\hat{\beta}_i$ is obtained by minimizing the least squares error between the estimated $\hat{y}(t)$ and the measured timetrace $y(t)$. Ultimately, the estimated factor $\hat{\beta}_1$ scaling the $HRF(t)$ will reflect the contribution of the modelled change of BOLD signal caused by the stimulation to the overall signal $\hat{y}(t)$ (provided there aren't any spontaneous fluctuations time-locked with the stimulation paradigm). The statistical significance of $\hat{\beta}_1$ is then determined through hypothesis testing, wherein the hypothesis that $\hat{\beta}_1 = 0$ is assessed (i.e. the interrogated voxel shows no task-related activation). Applying this inference testing on each voxel of the fMRI data provides p-value maps (p-values resulting from each individual test), or the so-called *statistical parametric maps* over the entire brain.

As mentioned in chapter 1, the resolution of fMRI is spatially limited to a few hundreds of microns and questions relating to the specificity of the BOLD response to neuronal activity remain unanswered. As such, capturing hemodynamic fluctuations of specific vessel calibres, such as capillaries, in response to neuronal activity is currently unattainable with MRI. In view of this limitation, several studies have used high resolution imaging techniques, such as 2PEF and OCT to shed light on the contribution of the different elements of the neurovascular coupling. For instance, Lindvere et al. used 2PEF to evaluate changes in capillary diameters following neuronal activation in the rat brain [147] whereas Srinivasan et al. employed OCT angiography to characterize the laminar behaviour of the hemodynamic response of capillaries [126], as previously observed in ultra-high resolution fMRI [12]. Although these studies, amongst others, have contributed to an overall deepening of our understanding of the neurovascular unit and its function, a gap remains between fMRI techology and processing tools and high-resolution imaging. The goal of the journal article presented in this chapter is therefore to show an application and adaptation of statistical parametric mapping for studying cortical activation at the capillary level using xf-OCM. Using the capabilities of OCT for total flow imaging, we captured quantitative changes in blood velocity occurring during functional hyperaemia in different vascular compartments at a very high-resolution ($\sim 2\mu m$), and fit them through a GLM framework modelling the rise of blood velocity during cortical activation.

2.1 Journal article

Statistical parametric mapping of stimuli evoked changes in total blood flow velocity in the mouse cortex obtained with extended-focus optical coherence microscopy

Paul J. Marchand,[1] Arno Bouwens,[1] Tristan Bolmont,[1] Vincent K. Shamaei,[1] David Nguyen,[1] Daniel Szlag,[1] Jérôme Extermann [1] and Theo Lasser[1]

[1] Laboratoire d'Optique Biomédicale, Institute of Microengineering, School of Engineering, École Polytechnique Fédérale de Lausanne (EPFL), CH1015 Lausanne, Switzerland

Functional magnetic resonance (fMRI) imaging is the current gold-standard in neuroimaging. fMRI exploits local changes in blood oxygenation to map neuronal activity over the entire brain. However, its spatial resolution is currently limited to a few hundreds of microns. Here we use extended-focus optical coherence microscopy (xfOCM) to quantitatively measure changes in blood flow velocity during functional hyperaemia at high spatio-temporal resolution in the somatosensory cortex of mice. As optical coherence microscopy acquires hundreds of depth slices simultaneously, blood flow velocity measurements can be performed over several vessels in parallel. We present the proof-of-principle of an optimised statistical parametric mapping framework to analyse quantitative blood flow timetraces acquired with xfOCM using the general linear model. We demonstrate the feasibility of generating maps of cortical hemodynamic reactivity at the capillary level with optical coherence microscopy. To validate our method, we exploited 3 stimulation paradigms, covering different temporal dynamics and stimulated limbs, and demonstrated its repeatability over 2 trials, separated by a week.

2.1.1 Introduction

Over the past decades, functional magnetic resonance imaging (fMRI) has revolutionised our understanding of brain function through its ability to probe neuronal activity throughout the entire human brain. Alongside the evolution of fMRI technology, powerful statistical tools such as statistical parametric mapping (SPM) have been tailored to provide comprehensive measures of cerebral activity[146]. While fMRI can provide whole-brain imaging, its resolution is currently limited to a few hundred microns. In contrast, optical microscopy favours an increased resolution over a limited field of view, and is able to investigate stimuli-evoked changes at the cellular level. Recently, Lindvere et al. used two-photon microscopy (TPM) to study and map capillary reactivity in the rat brain by imaging changes in capillary diameter during functional stimulation[147]. Nevertheless, measuring changes in red blood cell (RBC) velocity over several vessels with TPM, as opposed to changes in microvascular network geometry, requires more intricate scan patterns and would result in very long acquisition times (> 2 hours).

Optical coherence microscopy [61] (OCM), being an interferometric imaging technique, is sensitive to the Doppler frequency shift of light scattered off moving red blood cells. This Doppler shift can be exploited to obtain both qualitative and quantitative measurements of blood flow. Moreover, as three-dimensional images can be obtained through a two-dimensional raster scan, OCM is a promising technique for red blood cell velocity measurements as it can acquire volumetric flow images at a fast acquisition rate (< 5 minutes). To date, both the quantitative and qualitative imaging modalities have been demonstrated in a wide variety of applications, including in cerebral blood flow imaging. Interestingly, Srinivasan et al. have shown that OCM is a useful tool to study the neurovascular coupling [66, 126]. Alternative techniques, based on fluctuations of the backscattering have been devised to capture hemodynamic parameters: Lee et al. exploited the increased scattering occuring by the passage of a red blood cell through the focus to measure red blood cell flux, speed and linear density [117, 127]. Additionnally, Srinivasan et al. have related the power of the dynamic component of the acquired signal to red blood cell content [126].

Classical OCM, however, suffers from a trade-off between lateral resolution and axial field-of-view. Indeed, at lateral resolutions on the order of 1 μm, the axial depth-of-field is limited to ~5 μm. Consequently, OCM systems either have low lateral resolution (~10 μm), or require a 3D raster scan to be performed. Extended-focus OCM [73] (xfOCM) was developed specifically to overcome this limitation; it allows acquiring 3D images with the high resolution and axial field-of-view of two-photon microscopy, at the acquisition speed of OCM (<4 seconds per structural volume). Moreover, our group has recently derived a general theoretical model allowing for quantitative measurements of the axial and lateral velocity components of blood flow [148] and has proven its applicability in imaging cerebral blood flow in the mouse cortex [109]. Briefly, the method is an extension of traditional Doppler techniques and relates the mean and spread of the Doppler spectrum to the axial and lateral velocity components of the scatterers passing through the focus.

Here we present as a proof-of-concept, the first application, to our knowledge, of statistical parametric mapping tools to total blood velocity measurements in the mouse cortex using xfOCM (SPM-OCM), generating depth resolved maps of hemodynamic reactivity at the capillary level. Furthermore, we show that our method is compatible with longitudinal studies, which we demonstrate by repeated monitoring of the same animal and brain region over time.

2.1.2 Materials and Methods

Extended-focus Optical Coherence Microscopy:

The xfOCM set-up was optimised to measure changes in total blood flow velocity in cortical vasculature and its lay-out has been presented in detail in Ref.[75]. The optical system combines a Bessel-mode illumination with a Gaussian-mode detection, to obtain a constant lateral resolution over an extended depth of focus, while maintaining a good detection sensitivity. The xfOCM system combines a 10X, NA = 0.3 Zeiss Neofluar objective and a broadband Ti-Sa laser (Femtolasers) centred at $\lambda_0 = 780$ nm with a bandwidth of $\Delta\lambda = 120$ nm, providing an axial resolution of 2.5 μm in tissue and a lateral resolution of 1.3 μm maintained over 400 μm in depth. The interference pattern between the light originating from the sample and the reference arm is recorded by a spectrometer comprised of a high-speed line camera (Basler Sprint spL4096-140km) with a sensitivity > 90 dB.

Journal article

Table 2.1 – Summary of the 3 stimulation protocols used for the proof-of-principle of SPM-OCM

Protocol	Current [mA]	Limb	Timings (Baseline - Stimulation - Rest)
Pr1	1.5 - 2	Hindpaw	3 s - 3 s - 19 s
Pr2	1.5	Hindpaw	80 s - 20 s - 140 s
Pr3	1.5	Forepaw	80 s - 20 s - 140 s

Localization of the activation area using Optical Intrinsic Signal Imaging:

To localise the area of response in the somatosensory cortex to the electrical stimulation, the xfOCM platform was augmented with a collinear optical instrinsic signal (OIS) imaging module with an illumination ring of red LEDs (λ= 660 nm, Sloan AG), as depicted in Fig. 2.2(a). Prior to the xfOCM blood flow imaging, an initial stimulation protocol was performed during OIS acquisition, consisting of 3 seconds of rest, 3 seconds of stimulation at 1.5 mA and 3 seconds of rest. Each trial is repeated 10 times with an intertrial time of ~10 seconds. The area of response was then recovered by analysing changes in the reflectance of the red light during stimulation.

Animal Preparation:

All experiments were carried out in accordance to the Swiss legislation on animal experimentation (LPA and OPAn). The protocol (VD 2526) was approved by the cantonal veterinary authority of the canton de Vaud, Switzerland (SCAV, Département de la sécurité et de l'environnement, Service de la consommation et des affaires vétérinaires) based on the recommendations issued by the regional ethical committee (i.e. the State Committee for animal experiments of canton de Vaud) and are in-line with the 3Rs and follow the ARRIVE guidelines. Optical access to the somatosensory cortex was obtained through a 4 mm open-skull optical window on C57BL/6 mice (8 months old, both male and female, n = 3) anaesthetised with a mixture of Ketamine/Xylazine (80-100 mg/kg, i.p.). When removing the excised skull, care was taken not to puncture the dura. The exposed brain was sealed with a 4 mm circular glass coverslip using dental cement. A custom-made head fixation ring was then mounted on the skull with dental cement, to minimize motion artefacts during imaging and facilitate image localization between imaging sessions [54]. After surgery, the animals were allowed to rest for at least one week. Prior to imaging, the mice were anaesthetised using the same cocktail of Ketamine/Xylazine and then transferred to the xfOCM platform and secured through a head fixation platform. The power at the sample used throughout the imaging sessions was ~ 7 mW.

Electrical Stimulation:

Electrical stimulation was performed by inserting a pair of electrodes (Grass Technologies) subcutaneously in either the fore- or hindpaw of the animals. Pulses of 300 μs at 3 Hz were delivered at currents ranging from 1.5 to 2 mA. To validate our technique, we tested 3 different stimulation protocols (summarised in Table 2.1), including 2 different stimulation lengths (short and long) and different stimulated limbs.

2.1.3 Results:

Statistical Parametric Mapping Optical Coherence Microscopy pipeline:

With the area of response to the electrical stimulation localised through OIS imaging, an OCM angiogram was acquired over a subregion of the activated area. As depicted in Fig. 2.2(b), the angiogram acquisition protocol consisted in sampling each transverse position multiple times (here 3 B-scans, i.e. yz-slices) at a line-rate of 70 kHz. The vasculature was then revealed by suppressing the static component of the OCM signal over these multiple acquisitions, i.e. high-pass filtering along the slow-axis [95]. The resulting en-face angiogram image's size was 512 × 1'536 pixels corresponding to an area of 800 μm × 800 μm. From the angiogram, we split the region of interest into several lateral positions, depicted as yellow dashed lines in Fig. 2.3(a), Fig. 2.4(b), Fig. 2.5(a) and Fig. 2.5(e). This splitting allowed maintaining a sufficiently high temporal resolution (of 1 second per quantitative blood flow B-scan acquisition), whilst covering a sufficiently large portion of the activated area. At these selected lateral positions, we then acquired total blood flow traces (Fig. 2.3(b)) to quantitatively capture changes in blood velocity caused by neuronal activity. Blood flow quantification was performed using a method inspired on Doppler ultrasound imaging recently developed by our group [148]. In this method, the axial and lateral components of the velocity of moving scatterers are calculated at each image voxel from the mean and width of the local Doppler spectrum measured by xfOCM (as demonstrated in Fig. 2.2(e) and (f)). In order to measure the local Doppler spectrum, a time series of the xfOCM signal was acquired by oversampling 32 times along the fast scan axis at a line rate of 20 kHz. The Doppler spectrum for each voxel of the imaged volume was then obtained through a Fourier transform of these time series over the temporal dimension. As described previously [148], the Doppler Spectrum was then fit to a modified Gaussian function, from which the mean and width allowed estimating the axial and lateral velocity projections through equations (1) and (2) provided in the work of Bouwens et al. [109]. Table 2.2 summarizes the imaging protocols used here with their respective parameters.

In contrast to fMRI data, where the activity of a voxel typically reflects the sum of several different hemodynamic sources (arteries, venules, capillaries, etc.), OCM angiograms can resolve down to the smallest capillaries. A portion of the voxels of the OCM data will therefore not belong to vascular components and thus will not reflect any hemodynamic activity. To focus our SPM analysis only on voxels belonging to the vasculature, we proceeded to segment our OCM angiograms (Fig. 2.3(c) and (d)): the vessels' cross-sections were manually segmented from the angiographic measurements using a custom made MATLAB interface. In OCM-based blood flow measurements, vessels are typically accompanied by *tails* or *shadows* caused by multiple scattering. To avoid biased measurements, any vessels lying in these shadows were excluded from further analysis. Total blood velocity time traces were then obtained by averaging over the cross-section of the segmented vessel. Finally, the time traces were then temporally smoothened through a causal sliding window (support size of 2 and 3 seconds for the short and long protocols respectively) and averaged over the different trials (10 for the short protocol). The effective temporal resolution of both protocols is thus 2 and 3 seconds for the short and long protocols respectively.

General Linear Model fitting of quantitative blood flow velocity timetraces:

Maps of stimuli-evoked hemodynamic activity were obtained by applying a general linear model [146] (GLM) analysis to the aforementioned timetraces. Briefly, the GLM models a timetrace y as a linear
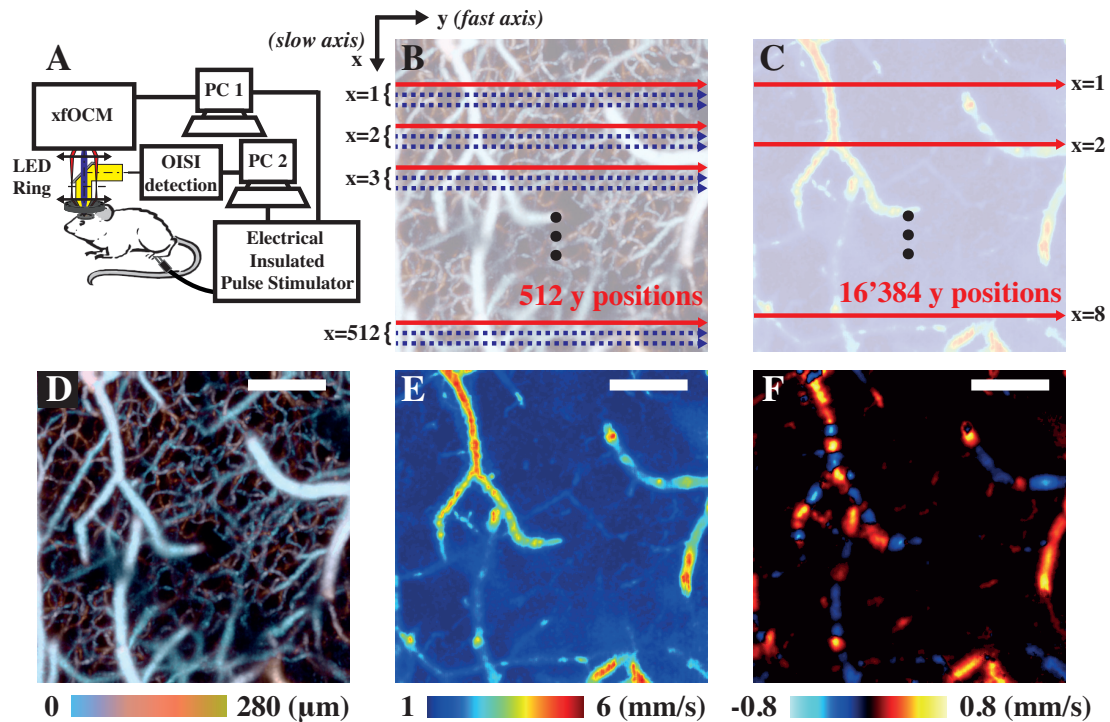
Figure 2.2 – The xfOCM set-up was augmented with an OIS imaging module and an LED ring to localise the area of maximal response to stimulation (a). Two individual computers controlled the xfOCM and the OIS detection respectively and were both connected to a Pulse Stimulator to deliver the electrical pulses to the limb of interest. OCM angiograms, as shown in (d), were obtained by acquiring 3 passes along the slow axis at each lateral position (b). In contrast, total flow velocity images, as depicted in tile (e), were obtained by oversampling 32 times along the fast axis (c). During the functional imaging, the total blood flow velocity protocol was applied at selected lateral positions (highlighted by the red arrow in (c) and by yellow dashed line in the following figures) instead of all over the lateral field of view to increase the temporal resolution of the acquisitions. The differences between total flow and axial flow images are portrayed in tiles (e) & (f) respectively, where the orientation of the vessel leads to discontinuities and speed reversal in the axial but not in the total flow image. Moreover, the range of velocities between both tiles is also different, as in (e) the magnitude of the total velocity vector is shown whereas only the magnitude of its projection along the optical axis is shown in (f). Scalebars: 200 μm.

Table 2.2 – Summary of the acquisition protocols used for the proof-of-principle of SPM-OCM

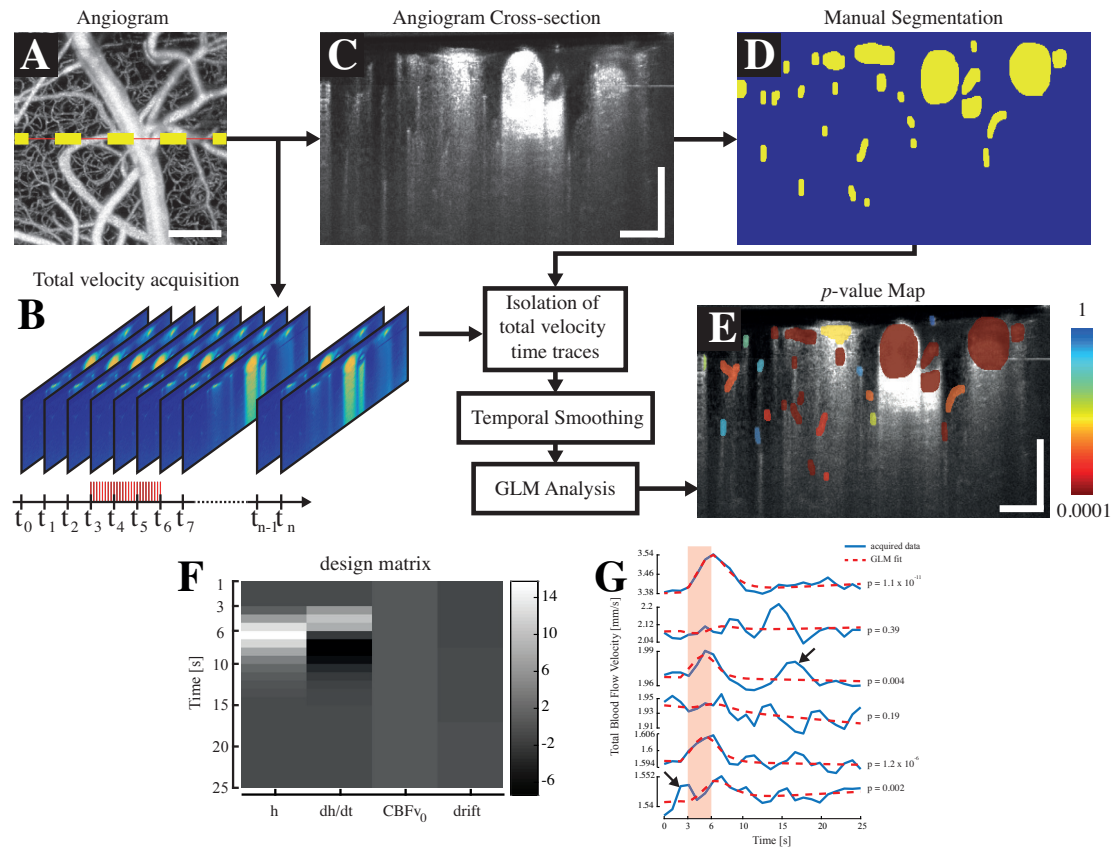| Protocol	Full Angiogram	Total Blood Flow Slice
# A-scans (fast axis × slow axis)	512 × 1'536	16'384 × 1
Area Covered	800 μm × 800 μm	800 μm line
Acquisition Speed	70 kHz	20 kHz
Acquisition Time	12s	1s

Figure 2.3 – SPM-OCM protocol: An angiogram (a) is first acquired on the area of response previously localised using OIS imaging. At a selected lateral position (highlighted by the yellow dashed line in a), an acquisition of total blood flow during the electrical stimulation is performed (b). Subsequently, an angiogram is acquired at the same location for segmentation purposes (c). The vessels in the selected angiogram are segmented manually via a MATLAB interface (d) and the total blood flow timetraces of each individual segmented vessel are isolated and smoothed temporally. Finally, a GLM analysis, using a design matrix (example for the short stimulation paradigm shown in (f)), is performed on each timetrace and leads to a p-value map, displaying the vessel's reactivity (e). The design matrix used in the GLM analyses comprised the velocity response regressor h, its derivative dh/dt, a baseline flow value $CBFv0$ and a drift component (f). An illustration of the results obtained by the GLM analysis is displayed in tile (g), showing that the p-value obtained by the regression is sensitive to the noise in the data, pointed by the arrows. Scalebars: 100 μm.

combination of a basis of regressors X and an additive noise component ε, as shown in the following equation:

$$y = X \begin{bmatrix} \beta_1 \\ \beta_2 \\ \vdots \\ \beta_n \end{bmatrix} + \epsilon \qquad (2.5)$$

The factors β, scaling the different regressors, are then estimated so as to minimise the sum of square errors between the measured and estimated y. To model the hemodynamic timetraces acquired using xfOCM, the matrix X, also termed design matrix, comprised a set of regressors including a velocity response regressor, its temporal derivative, a linear slope and a constant term (Fig. 2.3(f)). The velocity response regressor models the increase of blood flow velocity caused by the local neuronal activation, whereas its derivative accounts for the time lag between the onset of the stimulation and the response [146]. The linear slope component accounts for potential post-stimulus physiological noise. In practice, the velocity response regressor is obtained by convolving a hemodynamic response function (HRF) to the electrical stimulation paradigm. The HRF represents the impulse response of the cerebrovascular system, i.e. the vascular response caused by an infinitely short stimulus and is typically modelled by a gamma function. In fMRI SPM analysis, the HRF is a difference of two shifted gamma functions to account for the first peak in the BOLD response and its undershoot. In the blood flow velocity traces acquired with our approach, however, no evidence was found for the existence of such a dip. Hence, the HRFs used here consisted of a single gamma function:

$$HRF = (t - T_0)^{n-1} \cdot \frac{e^{(-t+T_0)/\lambda}}{(n-1)! \cdot \lambda^n} \qquad (2.6)$$

where T_0, n and λ are parameters controlling both the delay and the width of the response. For each dataset (i.e. animal/trial), the parameters of the HRF were estimated through a series of independent GLM analyses on the mean of the timetraces in the dataset using different HRFs, obtained by convolving gamma functions with varying parameters to the stimulus paradigm. The gamma function leading to the minimal difference of sum of square errors (lowest p-value), was then used as the HRF for the corresponding dataset (animal/trial). Interestingly, the HRFs obtained for each individual animal/trial showed a high level of consistency: out of the 5 estimated HRFs, only the one of the short stimulus of animal 3 differed.

To infer which vessels responded to the electrical stimulus, a hypothesis-testing step was performed to assess whether the parameter β_1 (scaling factor for the velocity response regressor) is different from zero. If the null hypothesis is rejected, i.e. β_1 is significantly different from zero, one can assert that the hemodynamic response function models the data, and thus that the selected vessel responded to the electrical stimulation. As shown in Fig. 2.3(e), by performing GLM analyses on each segmented vessel of the acquired volume, we generated p-value maps, where the vessels with the lowest p-value seemingly showed an activity which correlated the most to the electrical stimulation. The GLM is ultimately a regression technique, the p-value score will reflect how well the different regressors model the acquired data. As such, the technique is sensitive to noise that is not accounted for by the regressors.

This phenomenon is illustrated in Fig. 2.2(g), where different timetraces and their fits are shown (in blue and dashed red respectively). Physiological noise, pointed by the arrows in the third and last plot from the top, increases tremendously the p-value and could ultimately make the fit not statistically significant.

The familywise error rate was controlled through a Bonferroni correction with the number of time traces using an initial significance level α = 0.05 (segmented vessel compartment).

Additionally, we grouped each vessel in 3 different caliber categories : arteries, capillaries and veins, which were identified by tracing them to larger known vessels or by analysing the speed direction in penetrating vessels through their axial velocity component. We then analysed the average timetraces for each groups, and calculated the relative changes in blood flow velocity from the baseline values.

Stimuli-evoked activity maps using statistical parametric mapping OCM:

We tested our SPM-OCM procedure on 3 animals and 3 stimulation paradigms (see Table 2.1 for a summary of the protocols). In a first set of trials, we used protocol Pr1 to assess the variability of the evoked blood flow response within the different vascular components. The stimulation was repeated 10 times at each of the 5 lateral positions. The region of activation initially localised by OIS imaging (Fig.2.4(a)) was imaged by OCM angiography to reveal the microvasculature (Fig. 2.4(b)). As mentioned above, we performed the electrical stimulation and quantitative blood flow measurements at 5 lateral positions (dashed lines in Fig. 2.4(b)). The activation maps obtained using the velocity response regressor (i.e. result of the convolution between the HRF and the stimulation paradigm) in tile 2.4(i), are shown in tiles 2.4(c) to (h) where the color encodes the p-value of each vessel (red being the lowest p-value). The parameters of the gamma function used for this dataset were T_0=0, n=3 and λ= 1. All of the statistically significant timetraces are plotted in panel (c) of the same figure (with a significance level corrected to $\alpha_{corr} = 2.94 \times 10^{-4}$), confirming the heterogeneous nature of blood flow velocity timetraces in the cerebral cortex: even though each timetrace indicates a tendency to respond to the stimulation, their time lag and amplitude vary for each vessel, as highlighted by the arrows in panel (c) showing two timetraces experiencing similar baseline velocities and response amplitudes but delayed by 3-4 seconds. The relative changes and average velocities for each compartments are reported in panel (j) of 2.4 for each statistically significant timetrace. These plots show that capillaries exhibit in average a rise of 3% of their baseline value in response to stimulation, with changes going up to 10%. Interestingly, some vessels exhibit different p-values in the different tiles of Fig. 2.4(d)-(f), which could potentially be caused by variations in the depth of the anaesthesia during the imaging session.

In a second set of experiments, we used the longer protocol Pr2 to assess the viability of the technique for longitudinal studies. The second animal was therefore imaged twice, at a week interval. For both imaging trials, a longer stimulation period was applied to the contralateral hindpaw, with 80 seconds of baseline rest, 20 seconds of stimulation and 140 seconds of rest, at 1.5mA. A single stimulation trial was applied at each lateral position. Figure 2.5 displays the results obtained for the second animal at both sessions, with the angiograms (Fig. 2.5(a) & (e)) and the activation maps for 3 selected lateral positions (Fig. 2.5(b), (c), (d), (f), (g) & (h)). As indicated by the angiograms (Fig. 2.5(a) & (e)), both electrical stimulation trials were performed at the same location (i.e. same region within the hindpaw contralateral primary somatosensory cortex area). Moreover, the means of all of the total blood flow velocity time traces of each session, plotted in Fig. 2.5(i), show a similar response to the electrical stimulation in both trials (in magnitude and time lag). The slight difference in baseline flow
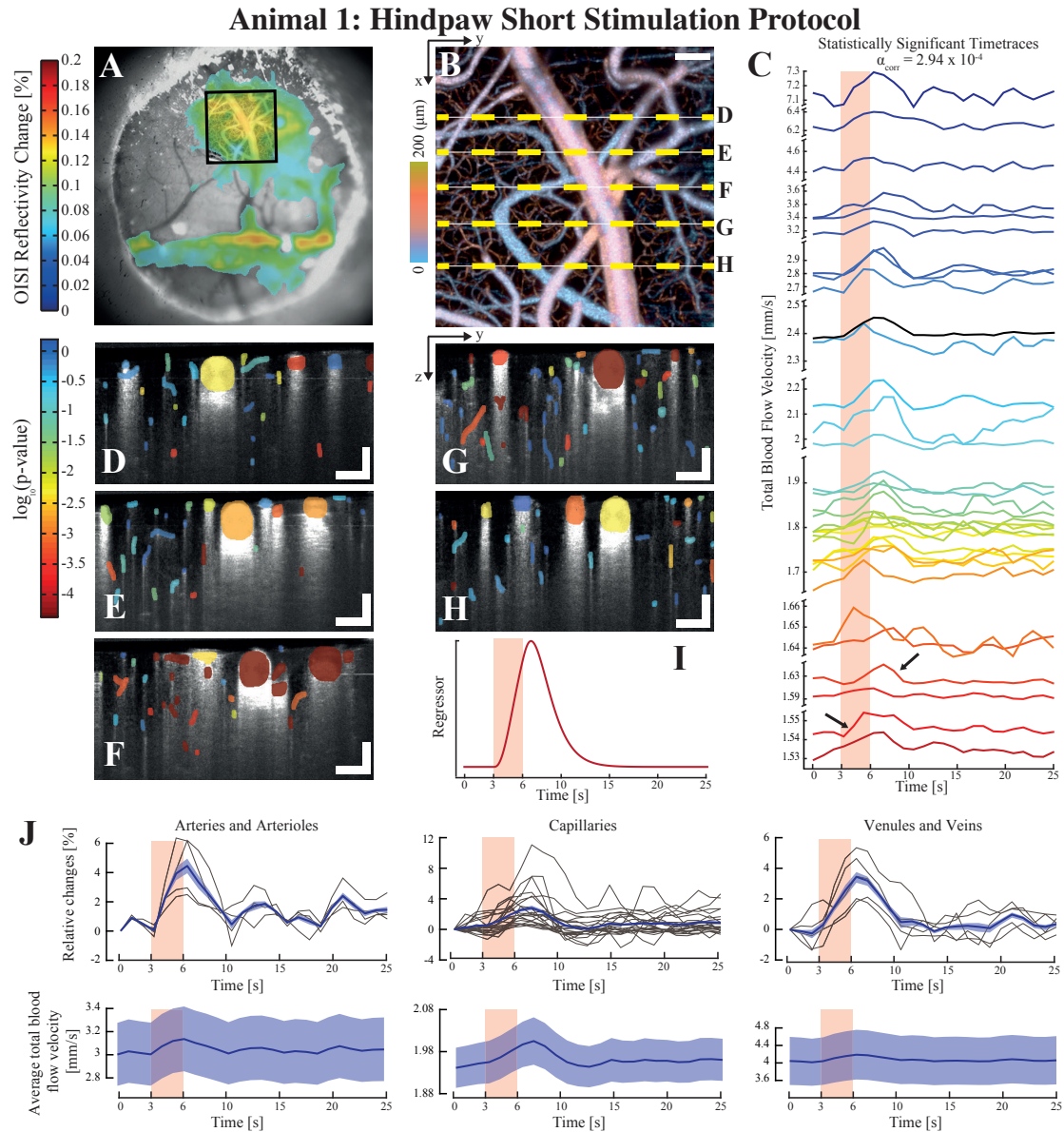
Animal 1: Hindpaw Short Stimulation Protocol

Figure 2.4 – Assessment of the variability of the evoked response within different vascular compartments using the short protocol on animal 1. OISI imaging is first used to localise the area of maximal response to the electrical stimulation, here with a 5x objective (a). An angiogram is then obtained in OCM over a selected region (square in tile (a)) to reveal the vasculature (b). The total velocity timetraces which lead to a statistically significant result after GLM analysis are displayed in tile (c), demonstrating the inherent heterogeneity of the hemodynamic reactivity of vessels (the arrows indicate both fast and slow total blood flow responses). The statistical maps of the different lateral positions highlighted in (b) are shown in tiles (d) to (h), where the p-value is color coded. The regressor used to model the velocity response for the GLM analysis of this dataset is shown in tile (i). The significant timetraces were grouped according to their respective vascular compartment (*arteries and arterioles, capillaries* and *venules and veins*) and both their average relative changes and average blood velocity are plotted in tile (j). The shaded areas in (j) represent the standard error around the mean (in bold). Each individual relative change curve are plotted in light grey in the relative changed panel. Scalebars: 100 μm.

velocity between both trials (25 µm/s) can be explained by slight experimental differences (level of anaesthesia, positioning of electrodes, etc.). The same gamma function was used for the GLM analysis of both trials, and used the following parameters: $T_0=0$, $n=3$ and $\lambda=1$ (identical to animal 1). The statistically significant timetraces for both trials are plotted in panels (j) and (k), with their respective significance level α_{corr}. Interestingly, in addition to the expected rise of blood flow velocity during functional hyperaemia, certain blood velocity timetraces presented in panels (j) and (k) exhibit distinct low-frequency oscillations, centred at 0.1 Hz (see arrows in both panels). These oscillations, present here in vessels with high baseline velocity (i.e. arteries or veins), have already been reported [41] and could originate from either vasomotion or Mayer Waves [17].
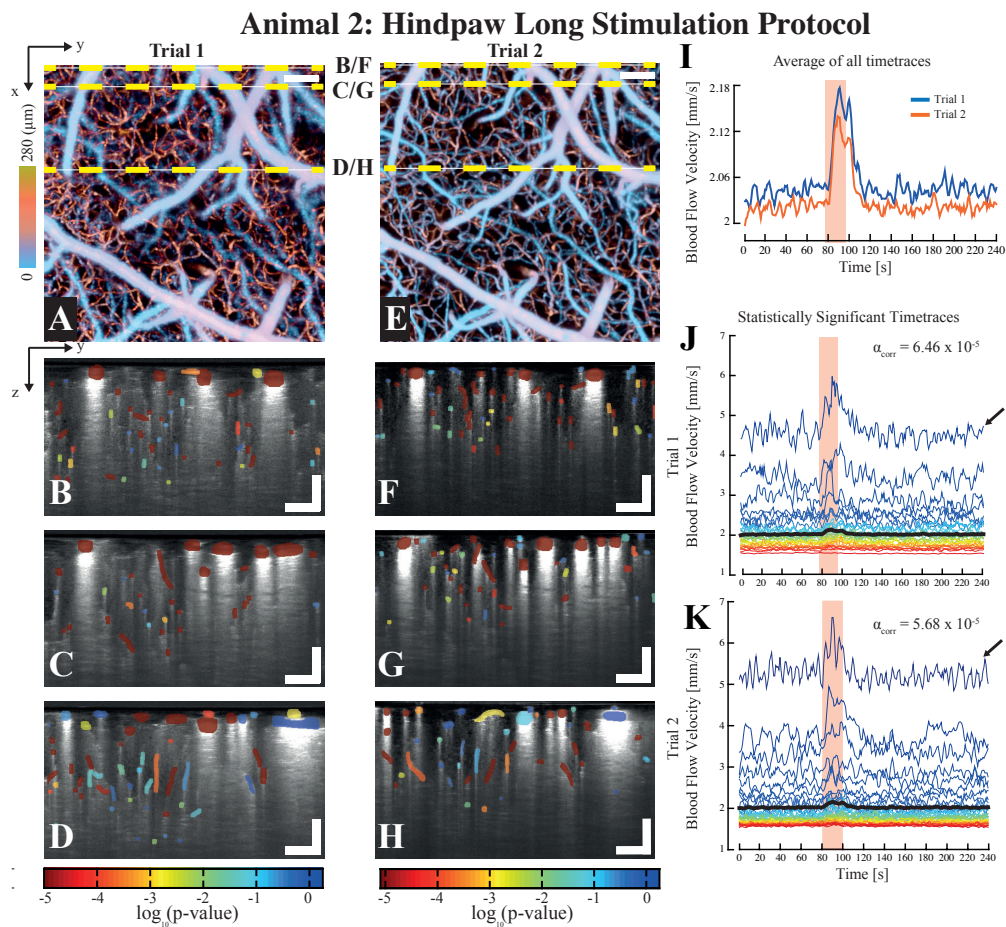
Figure 2.5 – Assessment of the viability of SPM-OCM for longitudinal studies obtained by applying the long protocol on animal 2. The depth-coded angiograms for both trials are shown in tile (a) and (e) respectively, showing that the region interrogated in each trials was identical. The statistical maps characterizing the hemodynamic reactivity of the vessels are shown for the lateral positions highlighted with yellow dashed lines in the angiograms ((a) & (e)) in tiles (b) to (h). The average of all of the timetraces for both trials are shown in tile (i), whereas a selection of the statistically significant timetraces for each trials are shown in tiles (j) and (k). Interestingly, the higher flow traces are accompanied by a low frequency fluctuation, typically observed in cortical arteries (pointed by the arrows in (j) & (k)). Scalebars: 100 µm.

Finally, in a last set of experiments, we imaged the velocity response by stimulation two different limbs with our method to assess the viability of using different stimulus protocols on the same animal.

The third animal was thus imaged at two different trials, using protocols Pr1 and Pr3 (short and long) to the hindpaw and the forepaw respectively. The results of both trials are displayed in Fig. 2.6. The short stimulation protocol is identical in timing to the one of animal 1 with a current of 2 mA. Similarly to animal 1, the timetraces of total blood flow velocity in panel (c) of Fig. 2.6 reveal the different dynamics of the responses, with changes in amplitude, lag time and spread. The statistical maps displayed in tiles (d) to (g), which refer to the dashed lines in tile (b) of the same figure, additionally reveal the spatial heterogeneity of the response to the electrical stimulation, with vessels seemingly quiescent in close proximity to reacting vessels. The regressor used in this analysis was based on a gamma function with parameters T_0=0.5, n=4, λ=1 and the corrected significance level was set to α_{corr}=2.5 × 10^{-4}. Similarly to animal 1, we also computed the relative changes and the average velocities for each compartment. Once again, the average relative velocity change occurring in capillaries in around 3%.

The long protocol was identical to the protocol used on animal 2 (Pr2) but was applied to the hindpaw of animal 3. The OIS responses of both stimulated limbs show two defined regions: S1HL and S1FL (tiles (a) and (i)). Similarly to the other protocols, the statistical maps obtained after GLM analysis of the total velocity time traces recorded during the electrical stimulus are displayed in tiles (k) to (p) of Fig. 2.6. The statistically significant timetraces obtained through the GLM analysis are plotted in tile (q), with the mean timetrace plotted in bold. The gamma function for this trial was identical to the one used for the data of animals 1 and 2, i.e. T_0=0, n=3, λ=1.

Compartment resolved velocity measurements:

In addition to the GLM analysis of the acquired timetraces, we have also computed the average speeds for the different vessel compartments present in our dataset (Arteries, Capillaries and Venules). The results for each animals and trials are presented in Table 3, where we computed the velocity of both in baseline and activated conditions for the statistically significant timetraces obtained by the GLM analysis. Additionally, we calculated the average speed velocity for all of the timetraces for each compartments. Interestingly, the average velocity of veins for the regions imaged in animal 1 and the long protocol of animal 3 are higher than the average velocity of arteries. This observation can be explained by the presence of large veins crossing the field of view of both acquisitions (see Fig. 2.4(b) and 2.6(j)). Additionally, the average velocities in both trials of animal 2 show a good level of consistency, thus strengthening the potential of longitudinal studies with the protocol used here.

2.1.4 Discussion and Conclusion

In this work, we demonstrated the application of statistical parametric mapping as a means to study stimuli-evoked hemodynamic traces acquired through extended-focus optical coherence microscopy. We developed a framework to statistically assess the response of vascular entities during electrical stimulation. Contrary to the application of SPM to fMRI data, using OCM allowed us to create maps of vessel reactivity at the capillary level, using the hemodynamic activity of individual vessels. These activations maps will be used in future studies to monitor alterations in the neurovascular coupling along the progression of diseases, by either comparing the strength of the response or by analysing changes in the hemodynamic response function.

As mentioned previously, the HRFs chosen for the different animals/trials were estimated in a data-driven manner, by analysing the average of all of the segmented timetraces in the dataset. The estimated HRFs were very similar across the different trials and animals, as highlighted by the parameters of the
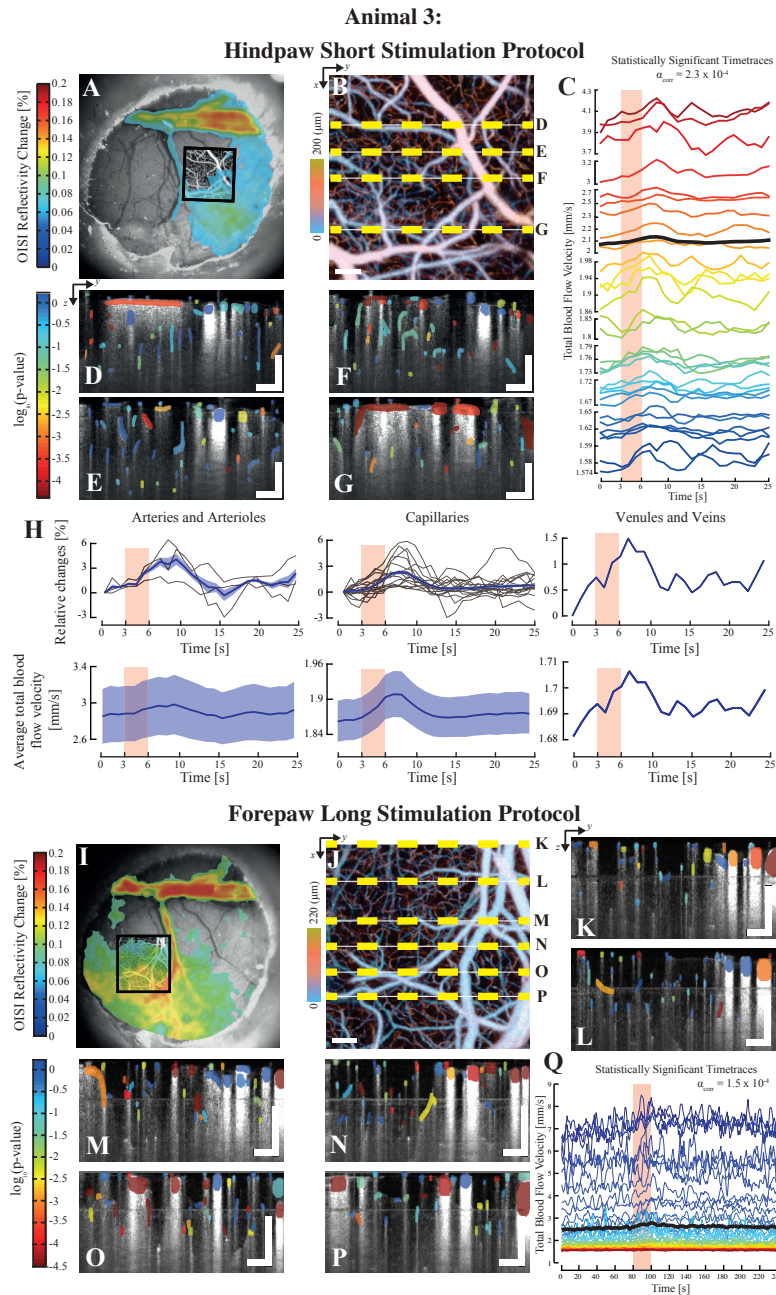
Animal 3:

Hindpaw Short Stimulation Protocol

Forepaw Long Stimulation Protocol

Figure 2.6 – Illustration of the use of different stimulation protocols using SPM-OCM: Results for both short and long protocols on the animal 3. The top half of the figure displays the results from the short electrical stimulation applied to the hindpaw (Pr1). OIS imaging was first used to localize the area of maximal response to the stimulus with a 5x objective (a). An angiogram was then acquired using xfOCM over the area localized by OISI (b). Statistically relevent total velocity timetraces are plotted in tile (c), revealing again the intrinsic heterogeneity of the stimuli evoked velocity response. The statistical maps of the lateral positions highlighted in tile (b) are displayed in tiles (d), (e), (f) and (g). Similarly to animal 1, the vascular compartment of each timetrace was identified and the mean changes relative to the baseline and mean velocity for each group is plotted in (h). The mean of the respective plots is shown in bold with the standard error. The individual relative change curves for each vessel are shown in light grey. The lower half of the figure presents the results obtained using the long protocol applied to the forepaw (Pr3). Once again, OISI was used to first localize the area of maximal response (h), which was then imaged using xfOCM angiography (i). The statistical maps obtained after SPM analysis of the total velocity timetraces are displayed in tiles (j) to (p), with their lateral positions highlighted in tile (i). Scalebars: 100 μm.

Journal article

Table 2.3 – Summary of the different average total blood flow speeds acquired for all animals and protocols. The mean value is given with the respective standard error. A: *Arteries and arterioles*, C: *capillaries*, V: *Venules and veins.*

| | | Total blood flow speed | | |
| | | Statistically significant timetraces | | All timetraces |
Animal	Vessel caliber	Baseline [mm/s]	Activated [mm/s]	Average [mm/s]
#1	A	3.02 ± 0.47	3.08 ± 0.48	2.94 ± 0.32
	C	1.95 ± 0.09	1.98 ± 0.10	1.77 ± 0.02
	V	4.03 ± 0.97	4.13 ± 1.00	4.45 ± 0.64
#2: Trial 1	A	3.54 ± 0.41	3.78 ± 0.46	4.03 ± 0.26
	C	1.86 ± 0.02	1.93 ± 0.02	1.84 ± 0.01
	V	2.87 ± 0.21	3.13 ± 0.26	2.66 ± 0.19
#2: Trial 2	A	3.78 ± 0.24	4.15 ± 0.28	4.04 ± 0.26
	C	1.79 ± 0.01	1.87 ± 0.02	1.78 ± 0.01
	V	2.77 ± 0.18	3.01 ± 0.21	2.52 ± 0.16
#3: Short	A	2.87 ± 0.50	2.93 ± 0.51	4.65 ± 0.78
	C	1.86 ± 0.07	1.89 ± 0.07	1.82 ± 0.02
	V	1.69 ± 0.00	1.70 ± 0.00	1.84 ± 0.12
#3: Long	A	3.65 ± 0.56	4.03 ± 0.66	4.40 ± 0.47
	C	1.83 ± 0.08	1.92 ± 0.10	1.81 ± 0.03
	V	4.66 ± 0.79	5.14 ± 0.91	3.61 ± 0.45

gamma function used for the different animals and trials. This consistency is particularly interesting as it indicates that the estimated HRF could be monitored to study diseases, as alterations of the latter function could reflect a dysfunction in the neurovascular coupling [149].

Interestingly, the dynamics of the velocity response regressors used in our analyses (obtained by convolving the HRF to the stimulation paradigm) closely resemble the hemodynamic responses obtained using alternative OCT-based metrics [126, 127]. Discrepancies between our measurements and those presented in the aforementioned studies could originate from the nature of the metrics (dynamic RBC content [126], qualitative dynamic RBC speed [126] and RBC flux [127]), from post-processing steps (i.e. temporal averaging) and ultimately from the experimental design (choice of animals, anaesthetic protocols, etc.). On the other hand, the obtained activation maps present a high level of heterogeneity in the responses, revealing both responding and seemingly quiescent vessels in close proximity. This observation can be explained by several factors. In terms of physiology, this apparent variability could be a reflection of the inherent statistical nature of capillary flow at rest and during activation [150]. Moreover, the presence of various vessel compartments (arteries, arterioles, capillaries, venules and veins), also provides an explanation for the heterogeneity of the data, as they all possess different intrinsic dynamics (blood flow velocity changes should be observed first on the arterial end, followed by the capillary bed and ending with venules and veins). Unfortunately, the temporal resolution of the current implementation of our blood flow velocity measurements (approx. 2 s) and the sparsity of the different vessel calibers does not allow us to perform a quantitative assessment of these dynamics. Alternatively, the effect of the anaesthesics has to be considered, as it can interfere with the hemodynamic response by suppressing vascular autoregulation and altering the neurovascular coupling [151, 55]. Here we used a cocktail of Ketamine/Xylazine for its ease-of-use and its compatibility with longitudinal imaging. Nevertheless, ketamine is an NMDA receptor antagonist [55] and can cause decreases in cerebral glucose metabolism in the somatosensory cortex.

Xylazine, used in conjunction with ketamine to minimize its side effects, is a muscle relaxant and causes hypotension and reductions in cerebral blood flow [152]. Ultimately, the effects of different anaesthetic protocols on the hemodynamic reactivity of vessels could be assessed using the method presented here. This knowledge will be very valuable in future studies, such that the choice of anaesthesia can be tailored to minimise the influence on hemodynamic reactivity. Moreover, for the purpose of this proof-of-concept, electrical stimulation of the paws was used to elicit cortical hemodynamic responses, nevertheless the method described can be applied to more complex protocols using trained awake animals (i.e. whisker, visual or olfactory stimulation).

In addition to the application of statistical parametric mapping tools to the data acquired during functional hyperaemia, we analysed the relative changes in velocity speed caused by the stimulus. Although there seems to be a certain level of consistency between the two reported acquisitions (Fig. 2.4(j) and 2.6(h)), care should be taken when analysing these results, as they are potentially prone to bias caused by the limited speed sensitivity of the measurement technique. They could reflect either only a limited fraction of the vessels (i.e. high speed capillaries) or could also origin from capillaries with baseline speeds below the noise limit with speeds rising above it during the activation. Additionally, as the number of arteries and veins was restricted by the field-of-view, these relative changes would only reflect a very limited category of vessels.

For applications where deeper layers of the cortex are of interest, the penetration depth of the xfOCM system can be increased through the use of longer wavelengths (e.g. 1.3 µm). Indeed, OCM has been shown to attain penetration depths superior to 1 mm in the murine brain [126]. These deeper cortical layers are of interest because the hemodynamic activity is known to be stronger as the metabolic demand is larger.

The quantitative blood flow imaging method used here allows the measurement of both axial and lateral components of blood velocity. This is an important advantage as the orientation of a significant portion of cortical vasculature is perpendicular to the optical axis. Using regular Doppler OCM, the velocity of such vessels cannot be measured when the optical axis is perpendicular to the optical axis, which would lead to discontinuities in the trace of the vessel (see Fig. 2.2(e) & (f)). Ultimately, the framework developed in this work can be applied to any other velocity acquisition scheme as it relies only on the dynamics of the hemodynamic timetrace and not on the nature of the measurement (quantitative or not). For instance, our method could also be used with the SIV method developed by Lee et al. [127] or with the metrics devised by Srinivasan et al. [66, 126].

The scanning protocols we used to measure blood velocity are sensitive to velocities higher than 1.5 mm/s, therefore only higher velocity capillaries and larger vessel calibers were imaged. This speed sensitivity limitation leads to a bias in the average capillary velocity measurements, which we computed to be around 1.8 mm/s (see Table 3) and is higher than the average capillary speed previously reported. Interestingly, the dynamic range of our method can be adapted simply by changing the scan protocol. For example, by lowering the sampling rate, by increasing the oversampling along the fast scan axis or by oversampling over the slow axis, slower flows and thus smaller capillaries can be imaged. However, for slow flow in narrow capillaries, the haematocrit might be low enough such that the discrete nature of RBC flow in capillaries can no longer be neglected. This could hamper the accuracy of Doppler based velocimetric techniques, as the acquisition of the Doppler signal would appear discontinuous. The Doppler spectrum fitting procedure used to estimate the axial and lateral velocity provides some degree of robustness to this effect [148], but a validation of the blood velocity measurements will be required when our method is to be used in capillaries with low haematocrit. Alternatively, these effects could be

hampered by injecting a scattering agent (such as an intralipid solution) in the vascular system, making the Doppler signal continuous [121]. Ultimately, at the acquisition speeds used in this work (around 1 Hz), potential aliasing from both respiration and heart rate can occur. These additional artefacts were alleviated here by averaging between trials.

Future work will focus on extending the technique by exploring other aspects of SPM and by completing the design matrix with regressors accounting for additional dynamics of the hemodynamic response and physiological effects. Additionally, the current optical system and acquisition protocols will be modified to increase the dynamic range of the CBF measurements and allow monitoring deeper vessels. As mentioned earlier, by increasing the temporal resolution of the technique, a complete delineation of the dynamics of functional hyperaemia from the arterial to the venal end could be possible and could be analysed with the lag regressor in the GLM.

The work presented here focuses mainly on demonstrating the feasibility, compatibility and performance of SPM with OCM acquired data. As such, no further analyses on the dynamics and heterogeneity of the hemodynamic response to somatosensory activation were presented yet. Nevertheless, the SPM-OCM technique will be used to characterise the reactivity of deeper and lower velocity capillaries and elucidate the hemodynamic characteristics across different layers and cortical regions. Furthermore, SPM analyses could be used to delineate alterations in the hemodynamic response function and strength of functional hyperaemia under different anaesthesics and throughout the development of neuropathologies such as Alzheimer's Disease.

3 | High resolution imaging with extended-focus optical coherence microscopy in the visible spectrum

HIGH RESOLUTION IMAGING METHODS are of paramount importance to understand cerebral structure and function at the cellular level. As mentioned in chapter 1, optical microscopy is a mainstay for high resolution imaging, as the short illumination wavelengths and high focusing power of optical objectives enable reaching sub-micron resolutions. Among optical microscopy techniques, optical coherence microscopy has recently emerged as a valuable tool to study brain structure in a label-free manner and at high resolution [66]. As described in section 1.2.1, the axial resolution of OCT systems is dictated by the source's central wavelength λ_c and bandwidth $\Delta\lambda$. Until recently, the lack of large bandwidth laser sources limited the axial resolution of FD-OCM systems to a few microns. Moreover, as most FD-OCM systems operate in the near-infrared to infrared spectral range, reaching high axial resolutions requires significantly increasing the source's bandwidth, leading to cumbersome optical designs and detection schemes. FF-OCM systems, based on a time-domain OCT detection scheme, were shown to reach axial resolutions close to 1 μm using thermal-light lamps centred in the visible wavelength range [153]. Such systems have shown great promise in imaging of brain tissue but provide a reduced sensitivity compared to FD-OCM and require long acquisition times to obtain volumetric images.

The emergence of mature supercontinuum lasers provided powerful large bandwidth light sources in the visible wavelength range compatible with FD-OCM technology and ultimately lead to a new field in OCT technology: *visible OCT* [154]. The advantages of visible light compared to infrared illuminations are twofold: increased light scattering and absorption by tissue and higher axial resolutions for comparable bandwidths. As mentioned in chapter 1, blood and other endogenous agents exhibit distinct absorption spectral signatures in the visible wavelength range, which are used in OIS and PAT to measure blood oxygenation and perform spectroscopy. In OCT, these absorption and scattering characteristics could open novel avenues for contrast in OCT images. Moreover, as mentioned before and as highlighted by Fig. 3.1, sub-micron axial resolution can be reached through the shorter central wavelength of visible light relative to infrared illuminations, as highlighted by Eq. 1.15. Overall, the enhanced contrast and higher resolution of visible light offer novel means to image and study cerebral structures in a label-free manner with OCT [87].

In this context, we developed an extended-focus OCM system operating at a central wavelength λ_c

= 635 nm with a bandwidth $\Delta\lambda$ = 245 nm to image cortical structures and cellular cultures. A lateral resolution of 0.4 µm was obtained using a high-NA objective, maintained over 40 µm through an extended-focus configuration. We used the system to image cortical structures of both healthy and alzheimeric fixed mice brain and live macrophages.
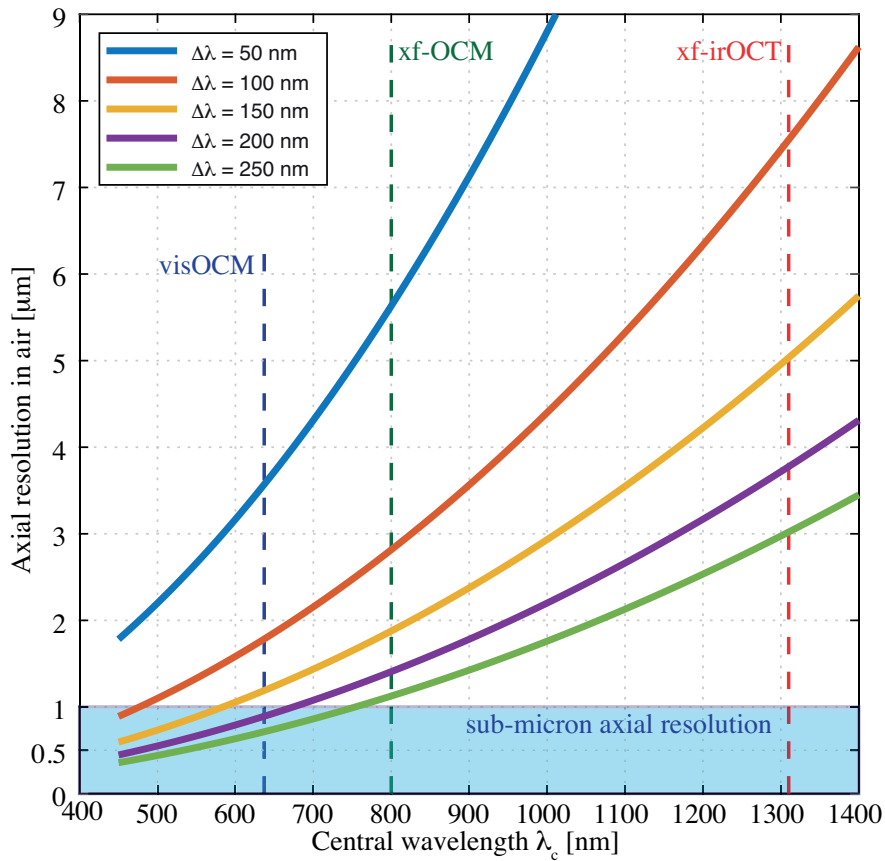

Figure 3.1 – Axial resolution in OCT imaging in function of the central wavelength λ_c and bandwidth $\Delta\lambda$ of the illumination source. The central wavelength of the visOCM, xf-OCM and xf-irOCT systems are highlighted (striped lines), as well as the region to obtain a sub-micron axial resolution (blue square).

3.1 Journal article

Visible spectrum extended-focus optical coherence microscopy for label-free sub-cellular tomography

Paul J. Marchand,[1] Arno Bouwens,[1] Daniel Szlag,[1] David Nguyen,[1] Adrien Descloux,[1] Miguel Sison,[1] Séverine Coquoz,[1] Jérôme Extermann,[1] and Theo Lasser[1]

[1]Laboratoire d'Optique Biomédicale, École Polytechnique Fédérale de Lausanne, CH-1015 Lausanne, Switzerland

We present a novel extended-focus optical coherence microscope (OCM) attaining 0.7 µm axial and 0.4 µm lateral resolution maintained over a depth of 40 µm, while preserving the advantages of Fourier domain OCM. Our system uses an ultra-broad spectrum from a super-continuum laser source. As the spectrum spans from near-infrared to visible wavelengths (240 nm in bandwidth), we call the system visOCM. The combination of such a broad spectrum with a high-NA objective creates an almost isotropic 3D submicron resolution. We analyze the imaging performance of visOCM on microbead samples and demonstrate its image quality on cell cultures and ex-vivo brain tissue of both healthy and alzheimeric mice. In addition to neuronal cell bodies, fibers and plaques, visOCM imaging of brain tissue reveals fine vascular structures and sub-cellular features through its high spatial resolution. Sub-cellular structures were also observed in live cells and were further revealed through a protocol traditionally used for OCT angiography.

3.1.1 Introduction

Over the past decades, optical microscopy has played a paramount role in investigating biological systems through its high spatial and temporal resolution. Confocal fluorescence microscopy [155] and light-sheet microscopy [156], through their capabilities in three-dimensional imaging, have become the mainstay for cellular and sub-cellular imaging. Nevertheless, while fluorescence provides molecular specificity, the influence of these agents on cellular processes is ambiguous, as they might interfere with the functioning of the cell. These effects combined with photobleaching ultimately hinder the possibility to perform long-term imaging.

In such studies, label-free microscopy offers an interesting alternative as it can provide wide-field images at high acquisition rates without using exogenous agents. Moreover, the absence of labels facilitates the sample preparation. Recent advances in phase microscopy [157] and ptychography [158] have allowed performing three-dimensional imaging of cellular cultures or embryos but remain limited to thin single layer structures.

Optical coherence tomography (OCT) is an interferometric imaging technique sensitive to refractive index contrast in the sample [61]. In OCT, the axial resolution is defined by the width of the illumination spectrum and an entire depth profile can be obtained from a single recording of the output spectrum. As such, only a two-dimensional scan is required to obtain a three-dimensional image.

Optical coherence microscopy (OCM), the microscopy analogue to OCT, uses high-NA objectives to obtain a higher lateral resolution. In standard OCM systems, however, the axial field of view is

dictated by the Rayleigh range and thus decreases quadratically ($\propto 1/NA^2$) with the improvement in lateral resolution ($\propto 1/NA$). This compromise can be circumvented by engineering an extended-focus illumination through the use of so-called diffraction-less beams such as Bessel beams [73]. To maintain a good collection efficiency of the scattered light signal, a Gaussian detection mode is used. Therefore, separate illumination and detection modes are required: a Bessel illumination mode and a Gaussian detection mode. This split between modes can further be exploited to filter specular reflections and obtain a dark-field OCM system [77]. The dark-field property is particularly important when investigating weakly scattering structures, such as cell samples, as it suppresses light reflected from the sample support which would otherwise strongly reduce the usable dynamic range of the detector. As such, all available dynamic range can be devoted to the desired, but weak, scattered light signal.

In this paper, we present visible spectrum optical coherence microscopy (visOCM). The system builds upon our previous dark-field OCM design, and improves its imaging capabilities for sub-cellular structures by using a large bandwidth illumination spectrum spanning visible to near-infrared wavelengths and a high-NA objective. The resulting system possesses an almost isotropic submicron resolution (0.4 μm laterally and 0.7 μm axially) maintained over a >40 μm depth of field. A conventional Fourier domain OCM (FDOCM) system without extended focus would have a much shorter depth of field of ∼ 2 μm for the same 0.4 μm lateral resolution. Hence visOCM extends the capabilities of our previous non-imaging visible light optical coherence correlation spectroscopy (OCCS) system and is optimized for three-dimensional cellular tomography [159]. Whereas recent studies have used OCT in the visible spectrum for spectroscopy [160, 161, 162], here we exploit the shorter wavelength of visible light, in conjunction with a very broad spectrum, to obtain a very high lateral and axial resolution, which is necessary for resolving sub-cellular structures. We present a strategy for dispersion compensation and the system's 3D resolution on microbead samples. We demonstrate visOCM's image quality and contrast on living cell cultures as well as fixed brain slices of healthy and alzheimeric mice.

Besides imaging the structure of a sample at a given time-point, there is also much interest in monitoring intracellular dynamics to understanding cell function. As such, several optical microscopy techniques have been developed to analyse cell trafficking and intracellular motility [76, 163, 31]. Recently, OCT methods developed to obtain qualitative and quantitative information on vascular function have been used to reveal sub-cellular compartments and quantify their activity [117, 164]. Being a Fourier-domain method, visOCM is capable of rapidly acquiring tomograms, and therefore these dynamic signal imaging methods can be applied to visOCM as well. In this context, we demonstrate dynamic signal imaging with visOCM on living cells using a protocol used in OCT angiography.

3.1.2 Materials and methods

Optical setup

As illustrated in Fig. 3.2, the optical setup is based on a Mach-Zehnder interferometer, allowing for a separation of the illumination and detection modes, necessary to obtain the desired Bessel-Gauss configuration. The output of a supercontinuum laser (Koheras SuperK Extreme, NKT Photonics) is first filtered through three broadband dielectric mirrors (BB1-EO2, Thorlabs) to reject the source's strong infrared emission. Then, the light is split by a polarizing beam-splitter (PBS251, Thorlabs), and injected in the interferometer using a single-mode fiber (P3-460B-FC-2, Thorlabs). As shown in Fig. 3.4(a), the spectrum in the interferometer is centred at 647 nm and has a 246 nm FWHM. After collimation, the

light passes through a polarizer and then a first beamsplitter (BS1) splits the light into the reference and illumination paths, where an axicon lens (Asphericon, apex angle 176°) generates a Bessel beam. The beam is then Fourier filtered in a telescope to remove stray light originating from the axicon's tip, after which it is steered to the scan-unit, and focused on the sample by a 40x high NA objective (Olympus, effective NA = 0.76). The back-scattered light is collected by the objective, de-scanned by the scan-unit and directed to the detection arm through a second beam splitter (BS2) where it is coupled to a custom-made spectrometer with a single-mode fiber (P3-460B-FC-2, Thorlabs). The spectrometer is comprised of a transmission grating (600 lines/mm, Wasatch Photonics) and a fast line-scan camera (Basler spL2048-140km). Dispersion matching between both interferometer arms was performed by adding a combination of prism pairs in the reference arm. The detailed dispersion matching strategy is presented in 3.1.2.

To obtain a dark-field configuration, the specular reflection was suppressed by spatially filtering the reflected Bessel ring through a mask in the detection arm (mask 2) and by properly filtering the stray light from the tip of the axicon lens (mask 1).
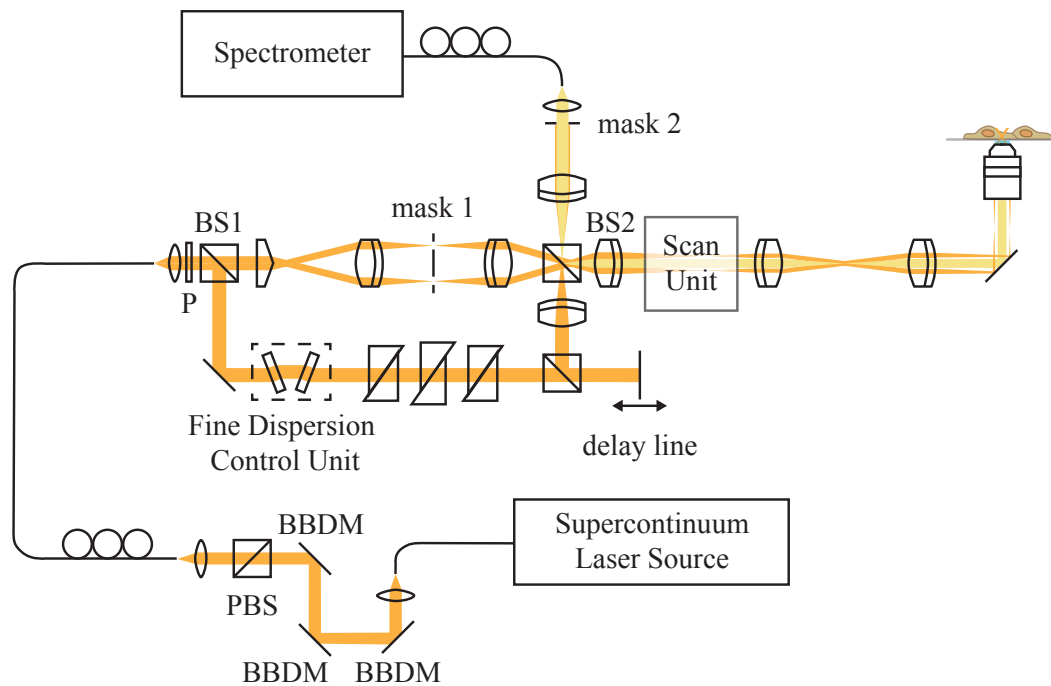
Figure 3.2 – Schematic of the extended-focus OCM using a broad spectrum in the visible wavelength range and a high NA objective for high axial and lateral resolution. By combining a Bessel illumination, generated by an axicon lens, and a Gaussian detection, a dark-field extended-focus system can be obtained. P: Polarizer, BBDM: Broadband dielectric mirror, BS: Beamsplitter, PBS: Polarizing beamsplitter.

Dispersion compensation strategies

The use of a broad illumination spectrum in visOCM renders dispersion matching more challenging, particularly in the visible spectrum where the relationship between the refractive index and the wave-

length becomes increasingly non-linear at shorter wavelengths. Here we opted for a physical dispersion compensation scheme where we first estimated the dispersion caused by the illumination and sample arms prior to constructing the optical system. This allowed us to calculate the best composition of prisms to place in the reference arm (Fig. 3.3(a)). In a second step, during the construction of the setup, we developed a real-time interface in LabView (National Instruments) to display the amount of residual dispersion and used a motorized stage to finely adjust the thickness of the different glasses (Fig. 3.3(b-c)).

Estimation of the dispersion in the optical system

Prior to constructing the optical system, we first estimated the thickness of each glass type present in the different arms of the interferometer. The glass type and respective thickness of each optical element (lenses and beamsplitters) were obtained from the data-sheets provided with each element by Thorlabs. The objective was not modelled in this initial assessment as its composition is unavailable. As depicted in Fig. 3.3(a) and described in Eq. (3.1), we then proceeded to estimate the k-dependent optical path length of each part of the system (sample arm, illumination arm and reference arm) by using the thickness of each glass and their respective dispersion curves (Sellmeier coefficients from the SCHOTT database available on https://www.refractiveindex.info) to obtain the optical path difference (OPD).

$$
OPD(k) = \left[n_{sample,SF5}(k),\ldots,n_{sample,UVFS}(k) \right] \begin{bmatrix} d_{sample,SF5} \\ \vdots \\ d_{sample,UVFS} \end{bmatrix} \ldots
$$
$$
+ \left[n_{ill,SF5}(k),\ldots,n_{ill,UVFS}(k) \right] \begin{bmatrix} d_{ill,SF5} \\ \vdots \\ d_{ill,UVFS} \end{bmatrix} \ldots
$$
$$
- \left[n_{ref,SF5}(k),\ldots,n_{ref,UVFS}(k) \right] \begin{bmatrix} d_{ref,SF5} \\ \vdots \\ d_{ref,UVFS} \end{bmatrix} \quad (3.1)
$$

The obtained OPD was then fit to a set of dispersion curves through a multivariate linear regression to find the thickness of the set of glasses to best balance the dispersion. As described in Eq. (3.2), the multivariate linear regression tries to model the OPD as the sum of the refractive indexes (in function of k) of each glass multiplied by their respective thicknesses and an error term $\epsilon(k)$. By performing this analysis, we can therefore retrieve the thicknesses of each glass required to compensate the OPD of the optical system. An initial analysis of several sets of glasses revealed that combining BK7 and SF10 fully balanced the dispersion of the system.

$$
OPD(k) = \left[n_{BK7}(k), n_{SF10}(k) \right] \begin{bmatrix} d_{BK7} \\ d_{SF10} \end{bmatrix} + \epsilon(k) \quad (3.2)
$$

Fine matching of the dispersion

During the construction and alignment of the system, the dispersion was finely balanced by calculating the residual dispersion in the system and by adjusting the thickness of each individual glass through a pair of motorized mechanical stages. The residual dispersion was measured by placing a sample consisting of a cover glass and a mirror. Then the interferogram's phase was calculated by Hilbert transformation [165], and a linear fit was subtracted (Fig. 3.3(c)). If the dispersion is perfectly balanced between the arms of the interferometer then the residual dispersion curve should be null throughout the spectrum. The motorized mechanical stages, as depicted in Fig. 3.3(b), consists of a stepper motor operating a cogwheel mechanism. The angle between two glass windows can be varied to fine-tune the amount of each glass type in the reference arm. Moreover, as the system is symmetrical, changes in the beam's transverse position caused by the passage of the light through the first window are compensated by the second window. As such, varying the amount of glass causes minimal changes in the alignment of the optical system. The combination of these two effects (fine-tuning and minimal misalignment) facilitates the dispersion compensation procedure. By observing the residual dispersion and iteratively changing the thickness of each glass we could balance the dispersion of the two arms of the microscope. We used SF6 windows, instead of SF10, for dispersion fine tuning.

Image acquisition and processing

All images were acquired at a 20 kHz A-scan rate (with an integration time of 43 μs) and with a power varying from 1.5 mW to 3 mW in the back-focal plane of the objective. With the exception of the dynamic signal imaging protocol (presented in 3.1.3), the size of each image was $512 \times 512 \times 2048$ pixels (x,y and k respectively). With the aforementioned parameters, the acquisition time for a single tile is ~ 14 seconds. Large field-of-views were obtained by stitching several tomograms (each having a lateral field-of-view of either 60 μm × 60 μm, or 120 μm × 120 μm) with a 30% overlap between each tile of the mosaic in both directions. Any tilt (angle with respect to the optical axis), was corrected on both axes (x-z and y-z) prior to stitching. The tomogram processing, tilt-correction and stitching were performed through a custom-coded MATLAB (Mathworks) graphical interface. The tomograms presented in Fig. 3.5–3.8 are displayed with the intensity in logarithmic scale for visualisation purposes. The large volume presented here contains 170 tiles, which requires ~ 40 minutes of acquisition time. The tomograms were convolved with a 3D Gaussian kernel ($\sigma_{x,y} = 0.187$ μm, $\sigma_z = 0.22$ μm) and were then resized to obtain an isotropic sampling using ImageJ.

Sample preparation

Mice brain slices

All experiments were carried out in accordance to the Swiss legislation on animal experimentation (LPA and OPAn). The protocols (VD 3056 and VD3058) were approved by the cantonal veterinary authority of the canton de Vaud, Switzerland (SCAV, Département de la sécurité et de l'environnement, Service de la consommation et des affaires vétérinaires) based on the recommendations issued by the regional ethical committee (i.e. the State Committee for animal experiments of canton de Vaud) and are in-line with the 3Rs and follow the ARRIVE guidelines. Brain slices were obtained by perfusing transcardially B6SJL/f1 mice with PBS followed by 10% Formalin (HT501128, Sigma-Aldrich). The mice were injected subcutaneously with Temgesic prior to the perfusion with heparinized PBS. The extracted brains were
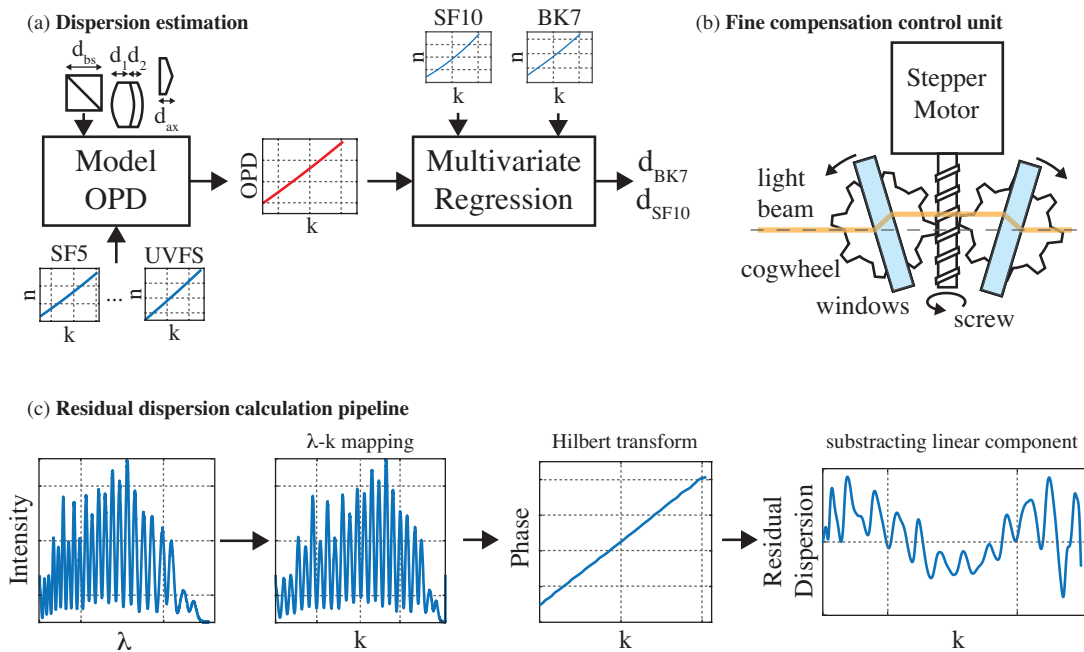
Figure 3.3 – Dispersion compensation strategies: (a) Prior to aligning the optical setup, a first estimation of the dispersion mismatch in the system is performed by modelling the optical path length of the different arms of the interferometer. The thicknesses and dispersion curves of the different glasses are used to model the OPD between the arms of the system. The OPD is then fit with a multivariate regression using the dispersion curves of SF10 and BK7 as set of regressors to obtain the respective thicknesses to fully balance the dispersion in the interferometer. (b) In order to match the dispersion, a compensation unit was devised allowing a fine control of the thickness of the glass. A mechanism comprising a stepper motor and cogwheels allows changing the angle of a pair of glass windows to vary the length of glass traversed by light. (c) During the alignment, the dispersion was matched by observing and minimizing the residual dispersion present in the system, obtained by a simple set of processing steps: The interferogram first undergoes a λ-k mapping step from which the phase is then extracted by a Hilbert transform. The linear component of this phase is then extracted and removed to reveal the residual dispersion.

then left in 4% PFA overnight, and then placed in a solution of 30% glucose. Finally, the brains were cut into slices using a microtome at a thickness of ~30 μm and placed on a glass coverslide. Brain slices from 5xFAD mice, a mice model of amyloid pathology, were obtained using the same protocol. The amyloid plaques were stained using a solution of Methoxy-X04 in DMSO, which was administered through two I.P. injections 24h and 2h before the perfusion, as described by Järhling et al. [166].

Macrophages preparation

In addition to mice brain slice imaging, we imaged live murine macrophages (cell line RAW 264.7) with the visOCM platform. The RAW 264.7 cells were cultured in an incubator at 37°C and 5% CO_2 using DMEM high glucose with pyruvate (4.5 g l-1 glucose, Roti®-CELL DMEM, Roth) supplemented with 10% fetal bovine serum and 1× penicillin-streptomycin (both gibco®, Thermo Fisher Scientific). Prior to imaging (1-2 days), the cells were seeded in FluoroDish Sterile Culture Dishes (35 mm, World Precision Instruments).

3.1.3 Results

System characterization

The system's lateral resolution was characterized by imaging a solution of nanoparticles of 30 nm in diameter embedded in a slab of PDMS. The size of these particles is small enough to interrogate the point-spread function (PSF) of the optical system. The depth-dependence of the lateral resolution was assessed by isolating and averaging multiple (~ 10) measurements of the PSF at 7 different depths. The lateral profile of the measured PSF at each depth was then extracted, and the position of the first zero served as a measure of the lateral resolution. As shown in Fig. 3.4(c) the width of the central lobe is maintained at 400 nm over 40 μm.

The axial resolution of the system was measured by imaging a mirror placed on a glass coverslip in the sample arm. The dark-field diaphragm (mask 2 in Fig. 3.2) was slightly opened to collect the specular reflection from the mirror. The reference power was adjusted to obtain maximum visibility of the interference pattern. The axial PSF, measured as mentioned previously, is plotted in Fig. 3.4(b) and has a FWHM of 0.92 μm in air, corresponding to a width of 0.69 μm in water.

Brain slice imaging

The imaging performance of visOCM was first demonstrated by imaging cortical structures in fixed mice brain slices (~30 μm thick) of both healthy and alzheimeric mice.

The lateral and axial resolution and contrast offered by the visible spectrum allows resolving several different entities present in the brain such as fibers, vascular structures, cell bodies and amyloid plaques.

Neural fibers

Similarly to previous studies performed with OCM at longer wavelengths [75, 83, 85, 86] and in full-field OCT [81], neural fibers appear as bright linear structures through their increased back-scattering. In Fig. 3.5(a) and (c), fibers emerge from the corpus callosum and the cingulum bundle and spread throughout the cortical column. The corpus callosum, shown in Fig. 3.6(d), contains a high density of fibers and

(a) **Spectrum**

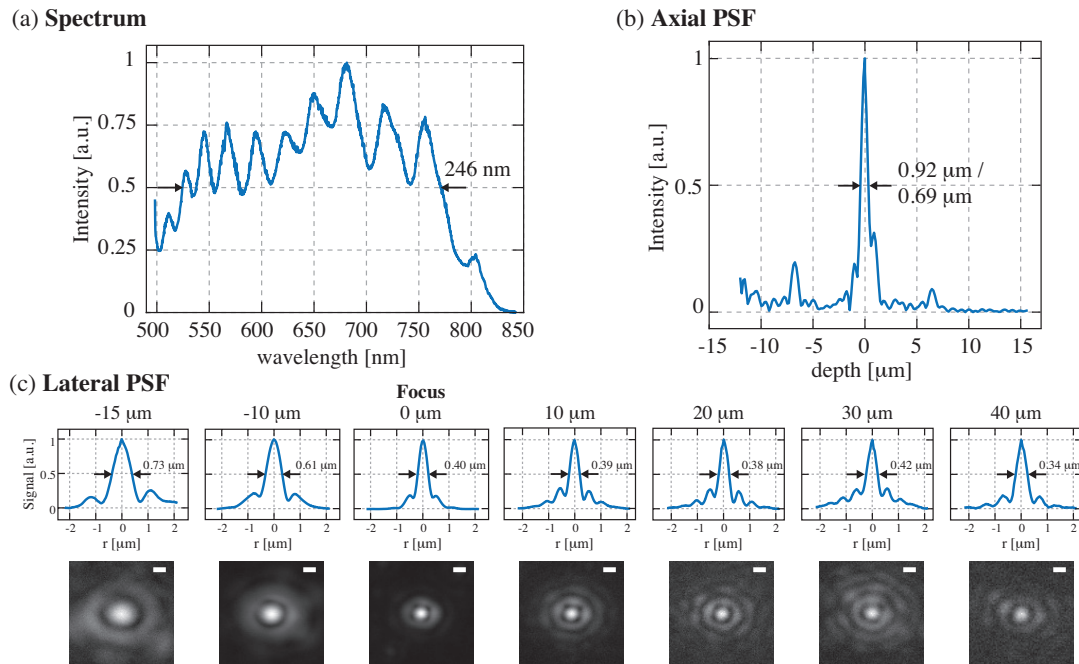(b) **Axial PSF**

(c) **Lateral PSF**

Focus

Figure 3.4 – Characterization of the visOCM system: (a) Illumination spectrum spanning from the visible to the near-infrared range, centred at 647 nm and 246 nm wide. (b)The ultra-broad spectrum leads to a submicrometric optical sectioning capability. (c) Plots and heatmaps (in linear scale) displaying the lateral PSF along the depth of focus of the objective, illustrating that the diameter of the central lobe is maintained at ~400 nm over 40 μm in depth. Scalebar: 500 nm
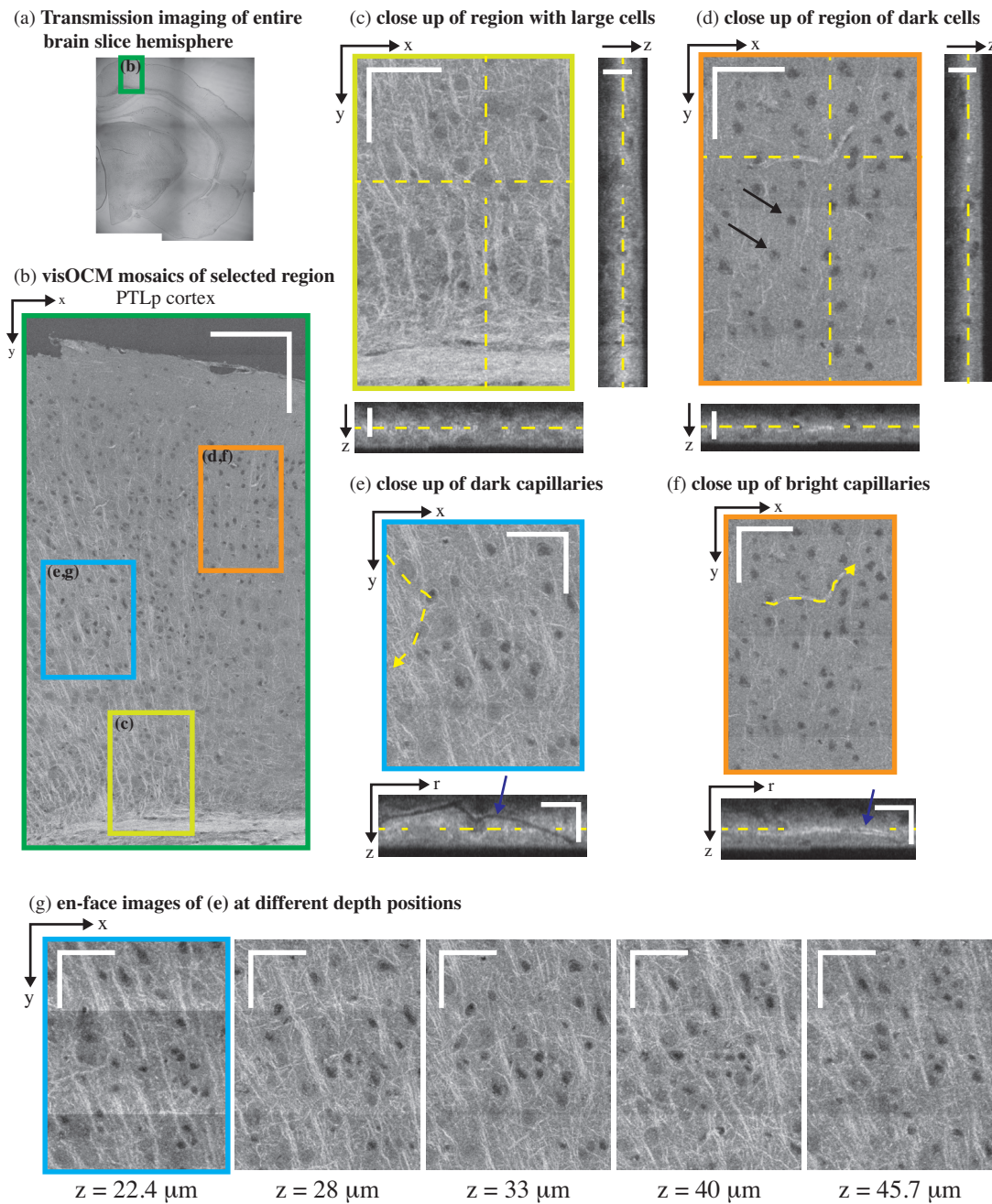
Figure 3.5 – *ex-vivo* visOCM imaging of the PTLp cortex in a B6SJL/f1 mouse brain slice. (a) A transmission image of the entire mouse hemisphere was first acquired to locate the desired area (green rectangle), which was then imaged with visOCM (b). The mosaic of part of the PTLp cortex, acquired with visOCM, reveals a variety of cortical structures, such as fibers, cell bodies and vascular entities (en-face view). In the mosaic, mainly two types of cells can be visualized, large cells as shown in (c) and smaller darker cells as pointed by arrowheads in (d). A depth scan of (c) is shown in Visualization 1. The orthogonal views in (c–d) highlight the three-dimensional repartition of these cell types within the depth of the slice. Capillary vessels can be discriminated from the tissue as either dark or bright structures as shown in (e) and (f) respectively. These different contrasts are further revealed in the orthogonal slices accompanying the close-ups, where one can trace the path of the hollow dark lumen or the bright vessel border, pointed by the arrowheads. En-face images at different depths show that visOCM can perform imaging over >20 μm (g). Scalebars: 150 μm (b), 50 μm for the en-face and 20 μm for the orthogonal views (c–g).
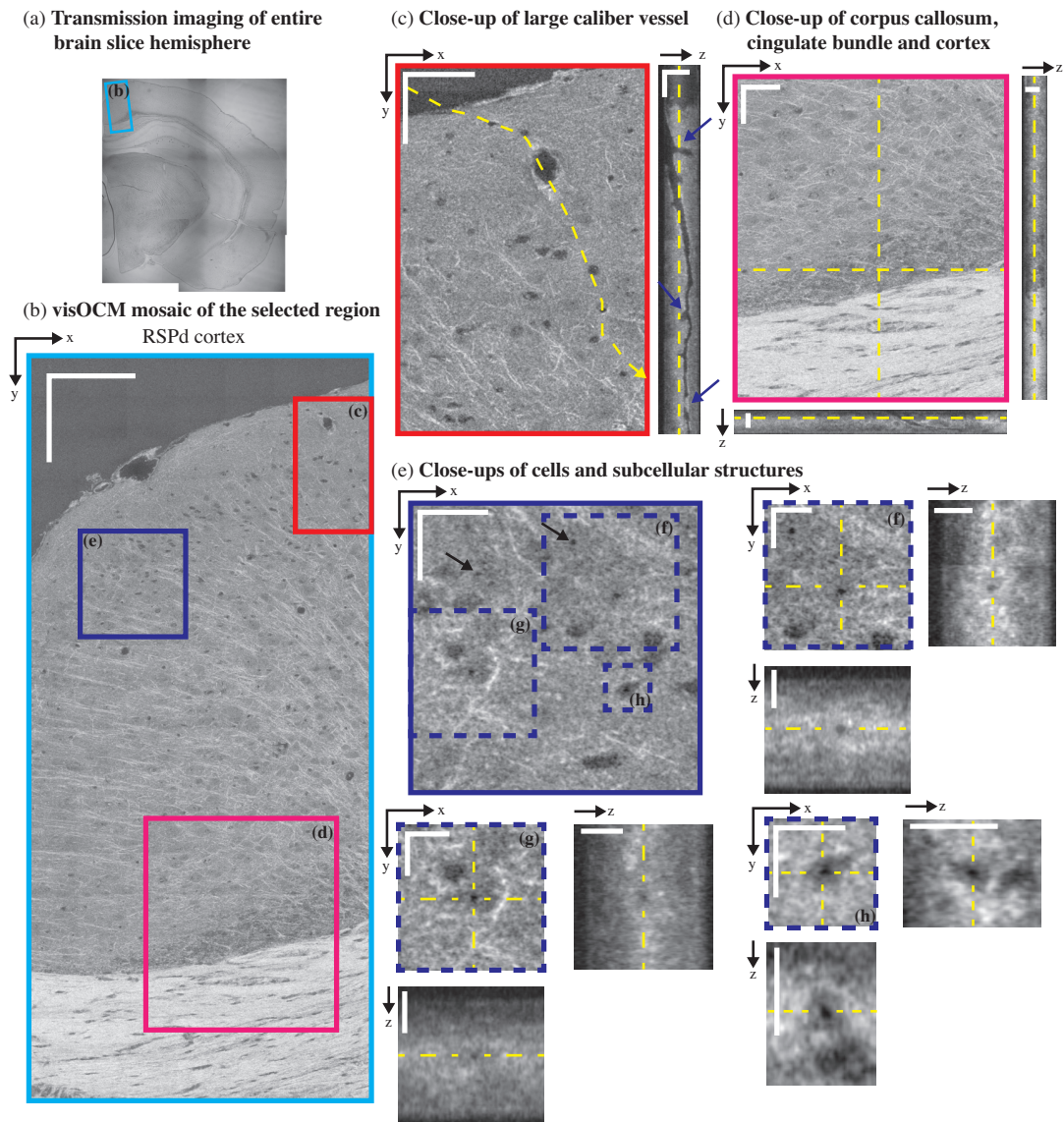
Figure 3.6 – *ex-vivo* visOCM imaging of the RSPd cortex in a B6SJL/f1 mouse brain slice. (a) A transmission image of the entire half hemisphere was performed to locate part of the RSPd cortex (blue rectangle). A mosaic of the area of interest was then obtained with visOCM (b), where one can appreciate the presence of fibers, vessels and cells. A large penetrating vessel (c) can be observed through the difference in contrast between its hollow lumen and the back-scattering of the surrounding tissue. Examples of bifurcations and potential clogging of the vessel are pointed by arrowheads in the orthogonal view (a depth scan is shown in Visualization 2). Fibers appear as thin oriented bright structures and are present in the cortex and in the corpus callosum (d). Finally, sub-cellular features can also be observed as darker spots within the cell bodies, as shown in (e–h) and pointed by arrowheads in (e). Scalebars: 150 μm in (b), 50 μm in the en-face view of (c–d), 20 μm in the orthogonal views of (c–d) and in the en-face view of (e), 10 μm in the en-face and orthogonal views of (f–g).

can be distinguished as a bright region with orientated stripes. The cortex is characterized by a lower density of fibers with a higher variability in their orientation.

Vascular structures

Vascular compartments, from large calibres (penetrating arterioles and ascending venules) to the smallest capillaries can be discriminated from the background tissue as either hollow tubes (from the empty lumen) or as thin bright structures. Figure 3.6(c) shows the en-face and orthogonal slice of a large penetrating vessel where one can distinguish the hollow lumen from the tissue and visualise bifurcations along the propagation of the vessel (Visualization 2). Additionally, the edges of the vessel exhibit an increased signal, which could either be caused by a change in the scattering properties of the vessel's membrane or its surrounding tissue (for example vascular smooth muscle). Smaller vessels, such as capillaries, can also be observed in the tomograms and appear either as dark or bright structures compared to the surrounding tissue. Figures 3.5(e) and (f) show both dark and bright capillary structures and show that it is possible to trace their trajectory regardless of their contrast. Similarly to the large vessel in 3.6(c), the dark contrast is indicative of a lack of scatterers within the lumen of the capillary. The bright contrast, on the other hand, could originate from scatterers filling the vessel's lumen (i.e. clogging during the perfusion procedure) or from the different scattering properties of the vessel's boundary.

Cell bodies

In addition to neuronal fibers and capillaries, visOCM imaging reveals different cell body types through their different contrast with respect to the extracellular space. Figures 3.5(b) and 3.6(b) present mosaics covering parts of the posterior parietal association areas (PTLp1) and the retrosplineal area (RSPd) respectively, where one can observe two main cell body types with different contrasts and shapes. As highlighted in Fig. 3.5(d), some of the cell bodies appear as dark spherical shapes, due to a decreased back-scattering. The second type of cell bodies visible in Fig. 3.5(c) and Visualization 1 have similar contrast than the extracellular space and are larger. In addition to their different shapes and back-scattering properties, the two cell body types also appear to be present in different regions of the cortical column: the darker and smaller cell bodies are denser in the upper layers whereas the larger cell bodies seem more prominent in the deeper layers, closest to the corpus callosum. Cell bodies in the cornu ammonis area 1 (CA1), as shown in Fig. 3.7(b), are also characterized by a darker contrast, similar to the cell bodies in the upmost layers of PTLp1. Additionally, one can notice in the RSPd brain slice the presence of a small darker substructure within the body of certain cells. Figure 3.6(e–h) displays a selection of these cells and their dark sub-cellular structure. Although a more complete study is necessary to elucidate the nature of this feature, our experience in live-cell imaging (results displayed in Fig. 3.8) has shown that a similar contrast is present in what seems to be the nucleus. The orthogonal views and tile (g) of Fig. 3.5 show that the signal acquired with visOCM extends throughout the depth of the tissue slice, although a loss in intensity and blurring can be observed in the deeper layers.

Amyloid plaques

Previous work from our group has shown that amyloid plaques can be distinguished from cerebral tissue using xfOCM operating at 800 nm through their increased scattering [75]. In continuation of this

work, we imaged brain slices of an alzheimeric mouse model with our novel visOCM system, with the expectation that the increased spatial resolution and different illumination wavelength would shed light on the details of these aggregates. We therefore imaged a part of the PTLp cortex and subcortical structures (CA1) of a 5xFAD mouse. As shown in Fig. 3.7(b) and similarly to the results in Fig. 3.5(b) and 3.6(b), the cortex is characterized by a high density of fibers and cell bodies. The subcortical region, below the corpus callosum, has a slightly lower intensity compared to the cortex and presents a line of cell bodies (CA1). Similarly to the results obtained at 800 nm [75], the amyloid plaques manifest themselves as high intensity regions with a darker core. The increased spatial resolution of the system reveals with great detail the irregular shape of these aggregates, as shown in 3.7(c–d). As expected, the plaques are present in cortical (see Visualization 3) and also subcortical regions [167], where the slightly decreased intensity of the cerebral tissue provides a higher contrast between the plaques and the background. The location of the plaques was colocalized with fluorescence imaging of Methoxy-X04 using a commercial widefield microscope (Axiovert 200M, Zeiss), a 20x / 0.5 NA objective and the DAPI filter set (Excitation filter: 365 nm, dichroic mirror: 395 nm, Emission filter: 445/50 nm). As shown the overlay in tiles (c–d) of Fig. 3.7, the locations of the aggregates in visOCM are in agreement with the location of the labelled structures in the fluorescence image (the visOCM and fluorescence are displayed in green and red respectively). Some mismatches between both channels in the overlay are caused by the presence of labelled plaques in a different plane than in the en-face visOCM image (i.e. the fluorescence image was obtained in a conventional fluorescence microscope and does not possess any axial sectioning).

Cell imaging

In addition to the imaging of tissue structures, we performed imaging of live macrophages in a cell culture. A mosaic of tomograms of these macrophages is shown in Fig. 3.8(a). The capabilities of the extended-focus can be appreciated in the orthogonal views of the tomogram, where the signal extends sufficiently in depth to reveal the three-dimensional organisation of the culture, with certain cells lying on top of other cells. The strongly scattering cytoplasm of the cell (pointed in pink in Fig. 3.8(a)) appears as a bright structure surrounding a darker subvolume, which most likely corresponds to the cell nuclei (pointed in green). The increased lateral resolution of the system allows resolving the filopodia on certain cells (pointed in red in Fig. 3.8(a)).

Dynamic signal imaging

In a second step, we analysed the dynamic properties of the scattering signal from living cells. In contrast to previous dynamic signal imaging techniques using the autocorrelation function or the standard deviation of the OCT signal [117, 163, 164], we extracted the dynamic component of the back-scattering through a point-wise subtraction of the complex OCM signal (Fig. 3.8(b)), as developed by Srinivasan et al. for OCT angiography [95]. A time-series of scattering fluctuations per voxel was obtained by sampling each transverse position (B-scan) 32 times with a timestep of $\Delta t = 27$ ms. Each timepoint was then temporally high-pass filtered (through a point-wise complex subtraction) and then averaged. A temporally averaged image was also obtained by averaging the repeated acquisitions. The results of this operation are shown in Fig. 3.8(c) and Fig. 3.8(d) showing the averaged and dynamic signals respectively. Interestingly, in addition to the lower intensity of the cell nucleus already present in the static imaging, the dynamic imaging further reveals details within the cell body. As shown in
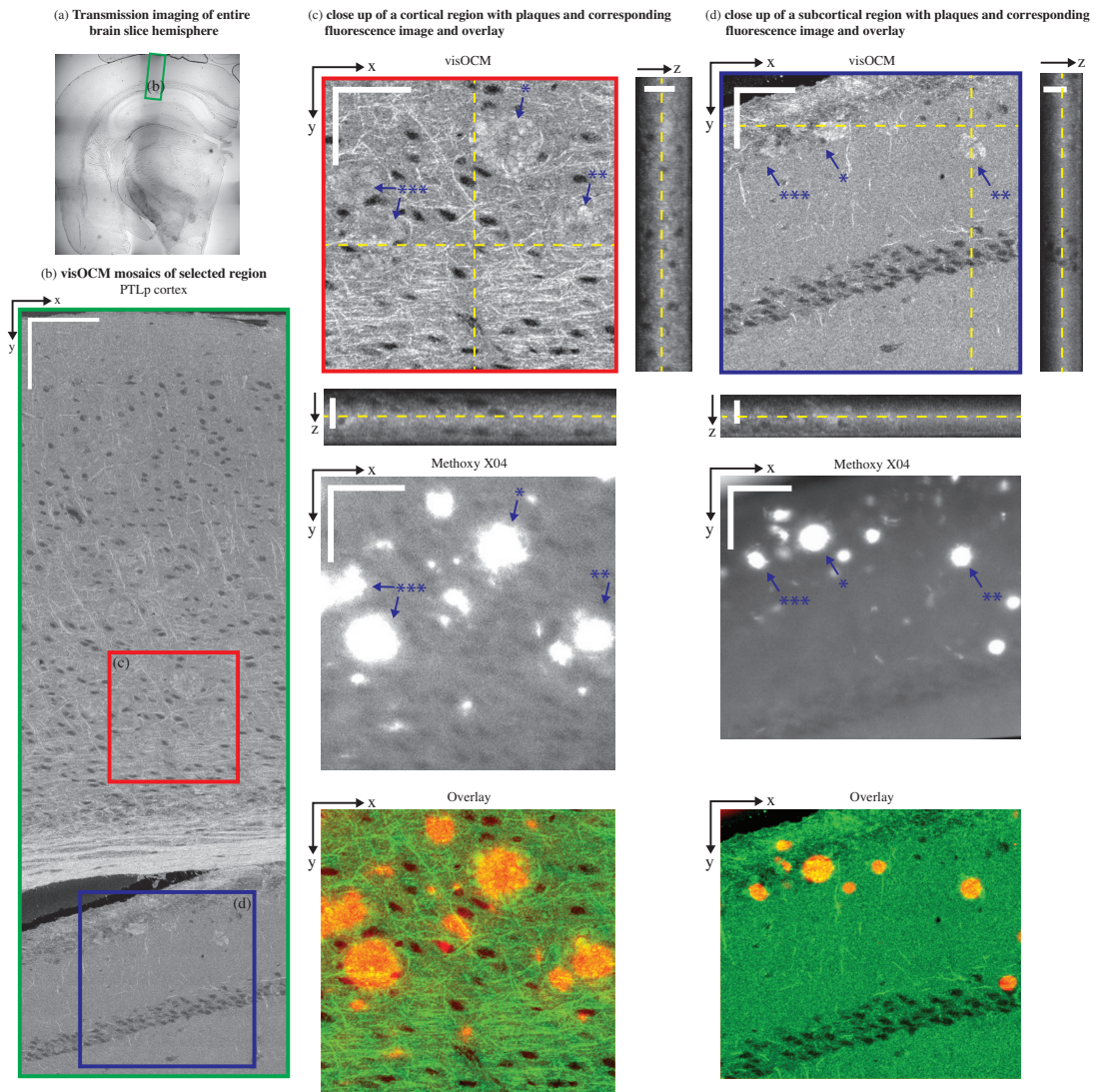
Figure 3.7 – *ex-vivo* imaging of cortical and subcortical structures in a 5xFAD mouse brain slice. (a) A transmission image shows the location of the area where a visOCM image mosaic was obtained (b). The visOCM mosaic reveals fibers, cells and amyloid plaques in both cortical and subcortical structures. Close-ups of areas of interest containing amyloid plaques, in both cortical and subcortical regions, are displayed with their en-face views and corresponding fluorescence image (c–d). Both images are overlayed with the visOCM and the fluorescence in green and red respectively. In the visOCM image, plaques can be seen as irregular high intensity regions (a depth scan of (c) is shown in Visualization 3). Scalebars: 150 μm in (b), 50 μm in the en-face and 20 μm m in the orthogonal views of (c–d).

Fig. 3.8(d), darker regions are present within the nuclei of the cells and brighter spots can be observed within the cytoplasm. Finally, the interface between the nuclei and the cytoplasm appears as a fine dark structure in certain cells. These differences are further revealed in Fig. 3.8(e) and (f) showing close-ups of a selected cell in the temporally averaged and dynamic signal image respectively. The cytoplasm and the nucleus are pointed with pink and green arrows respectively in Fig. 3.8(f).

3.1.4   Conclusion

In this work, we presented a novel OCM system, called visOCM, combining an extended-focus [73], a dark-field detection [77], a high-NA objective and an ultra-broad illumination spanning from the visible to the near-infrared wavelength range. As demonstrated here, the combination of these features provides an almost isotropic submicron resolution, maintained over > 40 µm in depth. The resulting system attains a lateral and axial resolution of 0.4 µm and 0.69 µm in water respectively. These characteristics were obtained by combining both a high-NA objective and a large spectrum centred in the visible wavelength range. A shorter central wavelength requires less spectral bandwidth to obtain a high axial resolution. Ultimately, we obtained an axial resolution of 0.69 µm through a spectrum with a FWHM of 246 nm. At longer central wavelengths, the bandwidth required to obtain the same optical sectioning becomes increasingly large through the quadratic dependency between the axial resolution and the central wavelength. For example, at 1300 nm, the bandwidth of the spectrum would need to be >800 nm. Such large spectrums would be limited by the spectral response and the spatial extent of current line cameras and by the bandwidth of optical elements (fibers, gratings, objectives...).

The visOCM system possesses the advantages of FDOCM systems combined with an extended-focus. As such, it has a higher SNR than time-domain based techniques (such as full-field OCM) [168] and can sample signals over a large range of timescales, from microseconds to minutes, necessary to study tissue and cell dynamics [76, 117, 163]. Moreover, scanning Fourier domain system offer more flexibility as the scanner can be programmed to image a restricted field-of-view at high speed. Through its extended focus, the visOCM system can image over a depth of 40 µm in a single acquisition (A-scan) and can perform volumetric imaging at higher speeds than standard scanning FDOCM systems, which typically require translating the optical focus in depth to obtain a 3D image [83]. Indeed, without an extended focus, the depth-of-field that an FDOCM system can acquire in a single A-scan would be limited to ~ 2 µm (for an equal lateral resolution of 0.4 µm). Therefore, ~ 15 2D beam scans acquired at different depths would need to be stitched together to image the same 40 µm thick volume, requiring significantly more acquisition time.

The capabilities of visOCM were demonstrated by imaging brain tissue slices of healthy and alzheimeric mice as well as macrophages cell cultures. The imaging of brain tissue with visOCM reveals several cortical structures as vessels, capillaries and cell bodies. Interestingly, these different structures exhibited a wide range of contrasts, even within the same structure type. Capillaries could be observed as both dark or bright hollow structures. Although one cannot discard changes in tissue caused by the sample preparation (i.e. clotting and vessel collapsing due to the perfusion), the bright contrast could emanate from the presence of tissue bordering the vessels (such as smooth muscle cells or pericytes). Conversely, the dark contrast arises from a lack of scatterers from the hollow lumen of the vessel. Previous studies involving OCT and OCM imaging of brain tissue showed that certain cell bodies could be identified through their different contrast within the cerebral tissue [81, 82, 83, 86, 117]. Srinivasan et al. and Tamborski et al. observed that certain neuron types could be discriminated
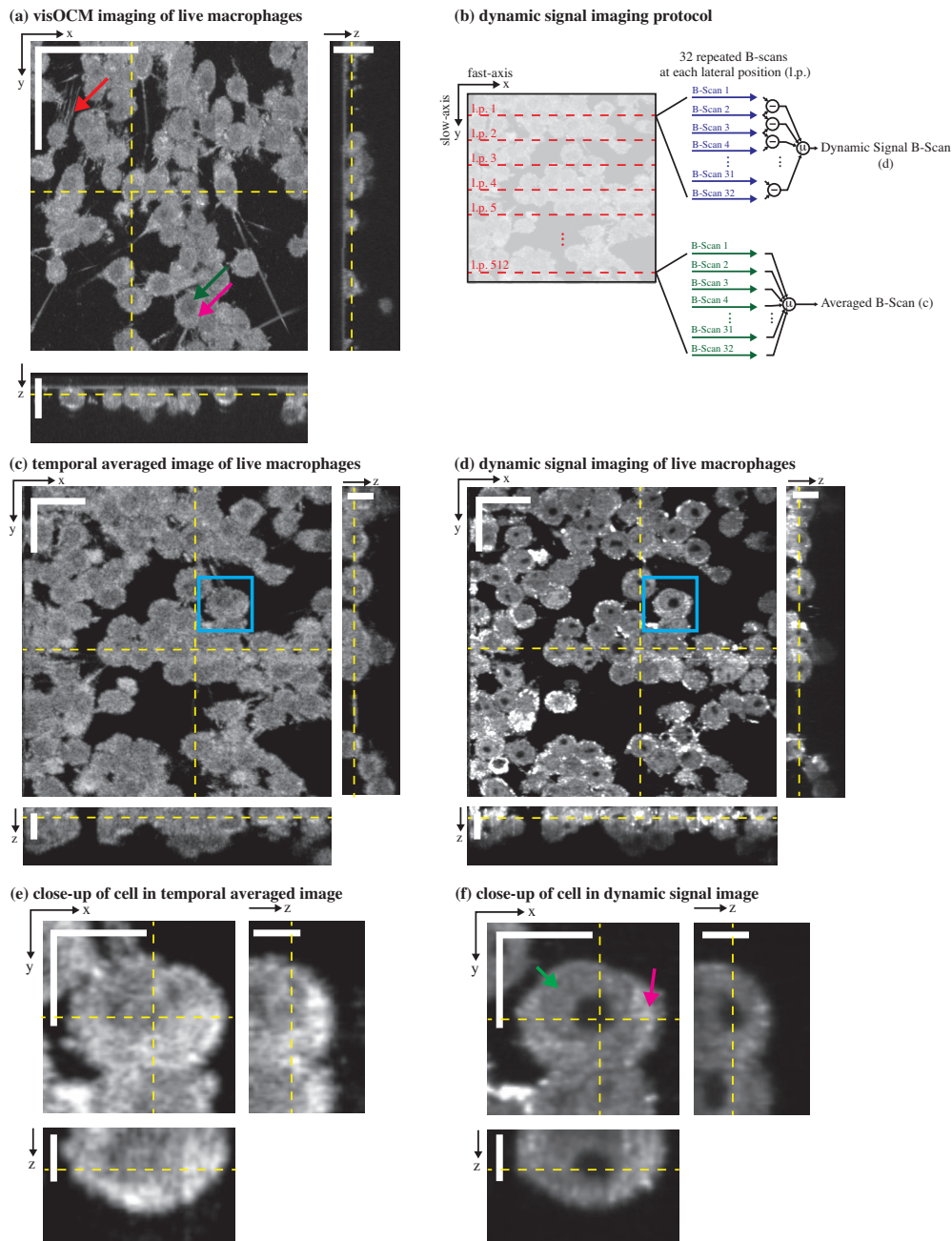
Figure 3.8 – visOCM imaging of murine macrophages. (a) A mosaic of macrophages obtained with visOCM with its orthogonal views reveals the three-dimensional organisation of cells in a culture. Cellular components can be observed such as the filopodia (pointed by the red arrow), the nucleus (pointed by the green arrow) and the cytoplasm (pink arrow). We further explored the capabilities of visOCM by applying a protocol similar to OCT angiography (b). The protocol entails imaging each lateral position along the slow axis 32 times (32 repeated B-scans per location). These 32 B-scans are either averaged or undergo a point-wise complex subtraction to obtain an averaged image (c) or a view of the dynamic components of the tomogram (d) respectively. The averaged image is identical in contrast to (a), whereas the dynamic signal image further reveals compartments within the cell (cytoplasm pointed in pink and nucleus in green), as either darker or brighter subregions (d) Close-ups of a selected cell in (c) and (d) are shown in (e) and (f) respectively, highlighting the differences in contrast between the averaged and dynamic images. Scalebars: 50 μm in the en-face view in (a), 20 μm in the orthogonal views in (a) and in the en-face views of (c–d), 10 μm in the orthogonal views in (c–d) and in the en-face views of (e–f), 5 μm in the orthogonal views in (e–f).

from the tissue by their dark contrast using an OCM operating at 1300 nm and 800 nm respectively [83, 82]. By exploiting a higher lateral resolution and by shifting the illumination spectrum to the visible wavelength range, we show that this intrinsic contrast seems to vary between cell bodies. Furthermore, the increased resolution of the visOCM system reveals features previously unobserved using other OCM systems such as sub-cellular structures (potentially the cell nucleus), thin bright boundaries surrounding capillaries and their hollow lumen. Future work will focus on elucidating the causes of these different contrasts.

In a second step, we built upon a previous study performed at 800 nm by imaging brain slices of alzheimeric mice models with our novel system [75]. Similarly to our aforementioned results, the plaques appear as bright irregular structures in the tomograms obtained with visOCM. Although the exact nature of this particular contrast remains unknown, the presence of metals (such as Fe) in amyloid plaque cores, as described by Plascencia-Villa et al. [169], might provide a first hint into the cause of this phenomenon. In fact, a previous study from our group showed that the contrast of the Langerhans islets in OCM images originated from the presence of Zn crystals [74]. Alternatively, this contrast could also arise from polarization effects as the plaques have been shown to have birefringent properties [170].

Finally, we demonstrated the performance of visOCM by imaging live-cells in cultures. The extended-focus and high acquisition rates available with the platform enable fast imaging of the three-dimensional structure of cell cultures. The shift in illumination wavelength and increase in NA provides the resolution necessary to identify thin structures such as filopodias and sufficient contrast to visualize seemingly sub-cellular structures. Recent studies have highlighted the importance of studying the dynamic properties of cellular back-scattering to understand cellular function [164, 171]. In this context, we explored the possibility to perform dynamic imaging, as already performed in full-field OCM [164], FDOCM [76] and phase imaging [31], with our novel imaging platform to further discriminate between sub-cellular compartments. We applied a protocol devised for OCT angiography [95] and show that a *dynamic* contrast can be obtained in a culture of macrophages. Apelian et al. and Leroux et al. obtain a similar contrast using dynamic full-field OCT and the ACF and demonstrate that their contrast is caused by ATP-consuming motion (likely mitochondria or other organelles) [164, 171]. Although more work is needed to identify the different regions and the nature of the signals obtained here, it is likely that the origin of our contrast involves similar mechanisms. Moreover, further work would be necessary to compare and assess the advantages and differences of the methods for obtaining contrast based on the dynamics of the signal (i.e. auto-correlation function [117, 163, 171], standard deviation [164] and point-wise subtraction [95]). Overall, the combination of the extended-focus, the high isotropic resolution and high acquisition rates make visOCM an ideal platform to monitor fast processes occurring at the sub-cellular level in cell cultures.

In addition to our demonstration of the capabilities of our novel visOCM system, we have introduced a strategy for physical dispersion compensation. We used a multivariate linear regression to model the OPD of the system prior to alignment and present a processing pipeline and a hardware unit to finely minimize the dispersion during the construction of the microscope. In this work, we opted for a hardware dispersion compensation strategy, however numerical dispersion compensation techniques could also have been used and will be explored in future work.

visOCM offers label-free 3D imaging of tissue and cell structures but remains limited through its lack of specificity. Our results show the ability to discriminate between structures in tissue through their individual back-scattering properties and potentially through their dynamic signatures (as revealed by

our dynamic imaging). Nevertheless, these contrast mechanisms are limited and do not always provide the desired molecular specificity. In such regards, the visOCM platform could be augmented with a collinear fluorescence channel, as in multimodal OCT platforms [153, 172, 173]. This configuration would allow molecular-specific fluorescent imaging to be complemented with visOCM imaging, providing information on the overall structural context of the organism under investigation. In addition to fluorescence, the visible spectrum could be used to explore the spectroscopic signatures of specific molecules. Spectroscopic OCT has shown great promise in its ability to provide additional contrast mechanisms [174, 160]. Having an illumination in the visible wavelength range could be used to visualize and discriminate between different endogeneous and/or exogenous contrast agents within the imaged tissue or cells.

Finally, even though the visOCM system was designed for imaging cells and relatively thin layers of tissue ($\sim 30\,\mu m$), thicker tissue slices can be imaged by translating the focus in depth. Placing the focus deeper in a tissue might however cause a loss of resolution through aberrations and increased dispersion, for which numerical and depth-dependent dispersion compensation techniques might be necessary. Ultimately, the imaging depth obtainable in tissue would be limited by the penetration depth of the visible illumination, measured here to be $\sim 110\,\mu m$.

Funding

Acknowledgments

Conflicts of interests

The authors declare that there are no conflicts of interest related to this article.

3.2 Technical notes

3.2.1 Theoretical description of dispersion in OCT

Dispersion arises from the spectral behaviour of the refractive index of materials, leading to a wavelength-dependent optical path length difference between the sample and reference arms of the interferometer. In an effort to understand the effect of dispersion on the axial resolution of the system, let's use the simple interferometer described in 1.2.1 and place a glass window in the sample arm. For simplicity, let's replace the sample by a simple mirror, with reflectivity r_s. The glass prism added to the sample arm has a thickness z_{glass} and a wavenumber dependent refractive index $n_{glass}(k)$. The optical path length (OPL) in the sample arm therefore becomes:

$$OPL_{sample}(k) = z'_s + z_{glass} \cdot n_{glass}(k), \tag{3.3}$$

where z'_s is the length of the part of the sample arm in air, and we considered $n_{air} = 1$. The difference of optical path length (dOPL) between the sample and reference arms becomes:

$$dOPL(k) = OPL_{sample}(k) - OPL_{reference}(k) = z'_s + z_{glass} \cdot n_{glass}(k) - z_r \tag{3.4}$$

Which leads to the following interferogram:

$$
\begin{aligned}
I(k) \quad &\propto \quad S(k) \cdot \cos(k \cdot dOPL(k)) \\
&= \quad S(k) \cdot \cos(k \cdot (z'_s + z_{glass} \cdot n_{glass}(k) - z_r))
\end{aligned} \tag{3.5}
$$

The term driving the modulation of the cosine function is therefore dependent on the wavenumber k. To analyse the effects of dispersion, let's consider an expansion of $n_{glass}(k)$ showing explicitly its dependence with the wavenumber k:

$$
\begin{aligned}
n_{glass}(k) \quad &= \quad n_{g_0} + n_{g_1} \cdot k + n_{g_2} \cdot k^2 + \dots \\
&\approx \quad \sum_{j=0}^{N} n_{g_j} \cdot k^j
\end{aligned} \tag{3.6}
$$

The interferogram therefore becomes (Eq. 3.5):

$$
\begin{aligned}
I(k) \quad &\propto \quad S(k) \cdot \cos(k \cdot (z_{glass} \cdot \sum_{j=0}^{N} n_{g_j} \cdot k^j + z'_s - z_r)) \\
&= \quad S(k) \cdot \cos(z_{glass} \cdot \sum_{j=0}^{N} n_{g_j} \cdot k^{j+1} + (z'_s - z_r) \cdot k))
\end{aligned} \tag{3.7}
$$

By expanding the cosine term into complex exponentials, Eq. 3.7 becomes:

$$I(k) \quad \propto \quad S(k) \cdot \left(e^{i \cdot (k \cdot (z_{glass} \cdot \Sigma_{j=0}^{N} n_{g_j} \cdot k^j + z_s' - z_r))} + C.C. \right)$$

$$= \quad S(k) \cdot \left(e^{i \cdot (k \cdot (z_{glass} \cdot n_{g_0} + z_s' - z_r))} \cdot e^{i \cdot z_{glass} \cdot \Sigma_{j=1}^{N} n_{g_j} \cdot k^{j+1}} + C.C. \right) \tag{3.8}$$

The non-linearity of the refractive index therefore adds a complex exponential term multiplying the term driving the modulation. By analysing the Fourier transform of the first term of Eq. 3.8, one obtains the following:

$$\mathscr{F}^{-1}\{I(k)\}(z) \quad \propto \quad \mathscr{F}^{-1}\{S(k)\}(z) \otimes \mathscr{F}^{-1}\{e^{i \cdot (k \cdot (z_{glass} \cdot n_{g_0} + z_s' - z_r))}\}(z) \otimes \mathscr{F}^{-1}\{e^{i \cdot z_{glass} \cdot \Sigma_{j=1}^{N} n_{g_j} \cdot k^{j+1}}\}(z)$$

$$= \quad \delta(z - (z_{glass} \cdot n_{g_0} + z_s' - z_r)) \otimes \left[\gamma(z) \otimes \mathscr{F}^{-1}\{e^{i \cdot z_{glass} \cdot \Sigma_{j=1}^{N} n_{g_j} \cdot k^{j+1}}\}(z) \right] \tag{3.9}$$

As such, in an interferometer exhibiting no dispersion, or where dispersion is fully balanced between both arms, the last term will become a simple $\delta(z)$ function and a similar expression to Eq. 1.14 is obtained. Nevertheless, in a system where the dispersion is not equal in both arms, an additional term will convolve the coherence length $\gamma(z)$. The PSF of the system will therefore be given by:

$$PSF(z) \quad = \quad \gamma(z) \otimes \mathscr{F}^{-1}\{e^{i \cdot z_{glass} \cdot \Sigma_{j=1}^{N} n_{g_j} \cdot k^{j+1}}\}(z)$$

$$= \quad \gamma(z) \otimes \mathscr{F}^{-1}\{e^{i \cdot z_{glass} \cdot n_{g_1} \cdot k^2}\}(z) \otimes \mathscr{F}^{-1}\{e^{i \cdot z_{glass} \cdot n_{g_2} \cdot k^3}\}(z) \otimes \ldots \tag{3.10}$$

The dispersion in the system will therefore lead to a PSF dictated by the convolution of the coherence length $\gamma(z)$ and multiple complex exponentials non-linearly dependent in k. Practically, this convolution term will result in a broadening of the PSF which will ultimately worsen the axial resolution of the system. Balancing the dispersion and thus cancelling out the non-linear dependency in k of the optical path length difference between both arms is therefore of paramount importance to take fully advantage of the optical sectioning capabilities of OCT imaging.

3.2.2 Dispersion in the visible wavelength spectrum

Balancing the dispersion in an interferometer implies that the optical path lengths of the reference and sample arms are identical for all wavelengths of the illumination spectrum. As shown in Fig. 3.9(a), in the infrared spectral range (from 900 nm and beyond), the refractive index of glass (here BK7, SF10 and UVFS) exhibit mostly a linear behaviour, with similar slopes. As such, adding a single glass element (e.g. BK7) in the reference arm and varying its length will permit reconstructing the OPL of the sample arm and ultimately compensating the dispersion in the system. In the visible wavelength range, the wavelength dependency of the refractive index becomes increasingly non-linear, with notable differences among glass-types. Consequently, matching the dispersion in complex system operating in the visible range is more cumbersome and can require using multiple glass types.

In addition to the central wavelength, the width of the illumination spectrum will impact the dispersion in the system, as the OPL will have to be matched over a larger spectral region. Moreover, in such cases, non-linearities in the refractive indices will have an increased influence on the overall dispersion. To illustrate this phenomenon, we simulated the dispersion caused by a 150 μm BK7 window in a

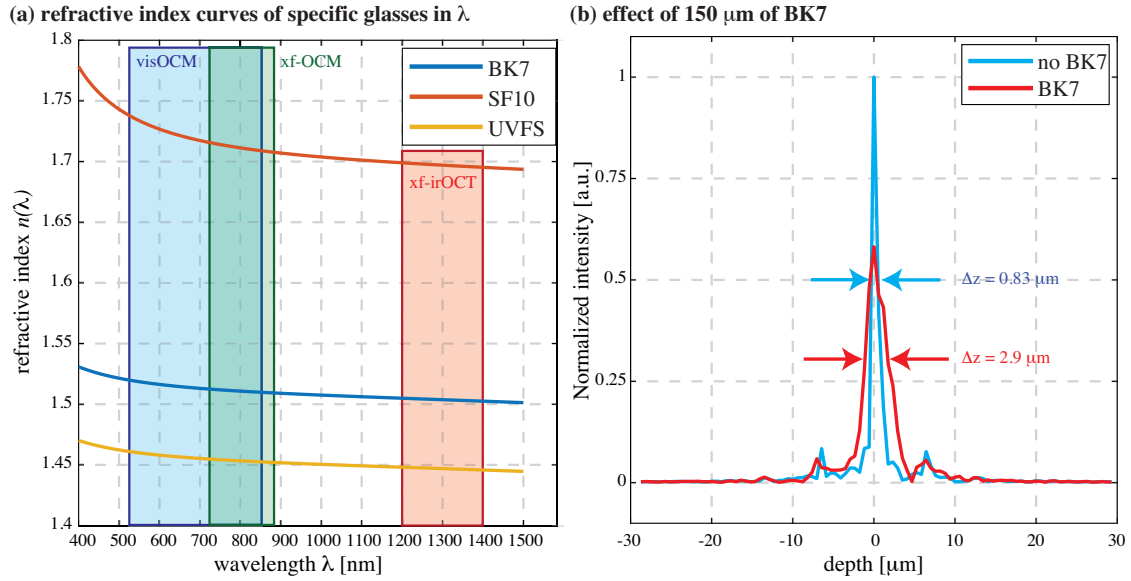**(a) refractive index curves of specific glasses in λ**   **(b) effect of 150 μm of BK7**

Figure 3.9 – Dispersion in OCT systems. (a) The refractive index of glass varies with the wavelength and exhibits increasing non-linearities in the visible wavelength range. The spectral ranges of the xf-OCM and xf-OCT systems presented in this thesis are highlighted by a blue, green and red square. Curves obtained through *www.refractiveindex.info*. (b) By placing 150 μm of BK7 in the sample arm, the axial resolution of the system degrades from an initial 0.83 μm to 2.9 μm due to the dispersion caused by the glass slide.

sample arm. The spectrum of the visOCM, presented in Fig. 3.4 (a), was used and was multiplied by Gaussian with varying widths. The results of this simulation are presented in Table 3.1, showing the bandwidth of the spectrum, the axial resolutions in dispersion-free conditions (measured as the full-width at half maximum), and the effect of the coverslide in [%] on the axial resolution:

Spectrum #	Bandwidth [nm]	Dispersion free resolution [μm]	Percent change caused by glass[%]
# 1	25	6.4	0.14
# 2	75	2.1	15
# 3	110	1.3	65
# 4	166	1.1	113
# 5	190	1	154
Original	246	0.82	252

Table 3.1 – Table summarizing the results of the effect of dispersion and the spectrum's bandwidth on the axial resolution

where the percent change caused by the glass was calculated as $100 \cdot \frac{\Delta z_{dispersed} - \Delta z_{disp.free}}{\Delta z_{disp.free}}$, where $\Delta z_{dispersed}$ and $\Delta z_{disp.free}$ are the simulated axial resolutions measured with and without BK7, respectively. As is illustrated in Table 3.1, increasing the resolution of the system by widening the illumination source results in an interferometer much more susceptible to dispersion. Carefully balancing the dispersion in both arms is therefore crucial to fully benefit from the performance of a high resolution system, such as the visOCM. This effect is also illustrated in Fig. 3.9(b), showing the broadening of the axial PSF caused by the BK7 slide for the total spectrum of the visOCM system (*Original* spectrum in Table 3.1).

Finally, using the framework presented in 3.2.1, it is possible to decouple the effect of the dispersion from the axial resolution by a convolution with a so-called *dispersion kernel* (i.e. the right term in Eq. 3.10). This is illustrated in Fig.3.10, presenting the magnitude of the dispersion-free PSF (left term in Eq. 3.10) and the dispersion kernel, calculated for the case presented above (placing 150 µm of BK7 in the sample arm). The system's axial resolution (dispersed PSF) is retrieved by convolving the dispersion-free PSF with the dispersion kernel, as shown in Fig.3.10(c), which is in agreement with the dispersed PSF shown in Fig. 3.9(b).
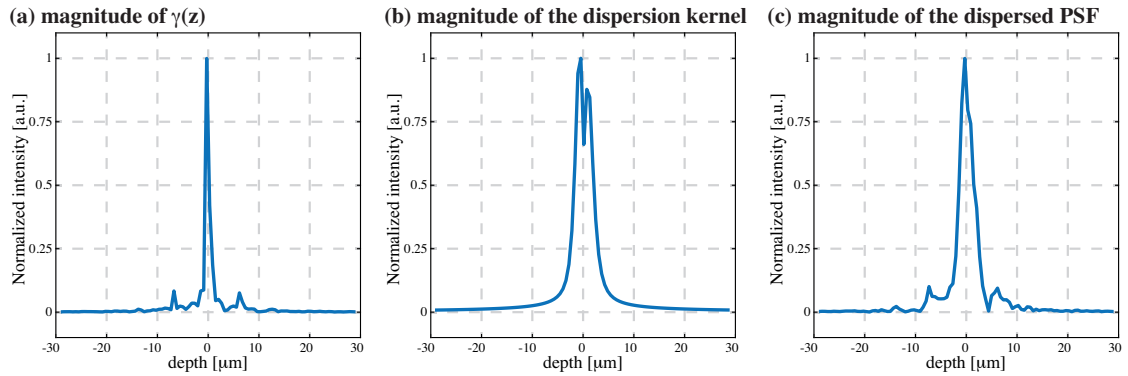
(a) magnitude of γ(z)   **(b) magnitude of the dispersion kernel**   **(c) magnitude of the dispersed PSF**

Figure 3.10 – Dispersion as a convolution with a dispersed PSF, for 150 µm of BK7 in the sample arm (a) The dispersion-free axial PSF is obtained through a Fourier-transform of the source, i.e. the coherence length of the interferometer. (b) The effect of dispersion of the PSF can be viewed as a convolution of the dispersion-free PSF with a kernel modelling its broadening due to dispersion. (c) The axial PSF of the system is obtained by convolving the kernel with the coherence length.

4 *In-vivo* imaging of shallow cortical structures with extended-focus optical coherence microscopy in the visible spectrum

THE PREVIOUS CHAPTER presented the design and implementation of a novel extended-focus OCM operating in the visible wavelength range. The system was conceived to perform very high resolution imaging of thin tissue slices and cell cultures. Yet, although imaging fixed tissue allows identifying specific structures and can provide valuable insight into structural changes caused by diseases, the amount of *functional* information afforded by *ex-vivo* imaging is limited.

In view of imaging mice brains at high resolution *in-vivo*, the visOCM system presented in chapter 3 was adapted to accommodate anaesthetised mice and image over the entire penetration depth of visible light in tissue. Although the high-resolution system previously described reached a lateral resolution of 0.4 µm, its axial extent was set to image fixed tissue slices and thin cellular structures (up to 40 µm in depth). Thicker fixed slices can be imaged by shifting the focus throughout the imaging session but increases the overall imaging time. In an *in-vivo* context, the depth multiplex capability of OCT enables monitoring the activity of various depths concomitantly. The available imaging depth of the modified system, termed extended-focus visOCM (xf-visOCM), was thus increased to fill the entire penetration depth of light in tissue, by reducing the lateral resolution to 1.6 µm. Similarly to previous observations with the visOCM and with other OCM systems, imaging the superficial cortex with xf-visOCM revealed several cerebral structures, such as myelinated axons, capillaries and even neurons in layers II/III, at an unprecedented axial resolution.

4.1   Journal article

In-Vivo high resolution cortical imaging with extended-focus optical coherence microscopy in the visible-NIR wavelength range

Paul J. Marchand,[1] Arno Bouwens,[1] Daniel Szlag,[1] and Theo Lasser[1]

* **These authors contributed equally to this work.**   [1]Laboratoire d'Optique Biomédicale, École Polytechnique Fédérale de Lausanne, CH-1015 Lausanne, Switzerland

Visible light optical coherence tomography has shown great interest in recent years for spectroscopic and high resolution retinal and cerebral imaging. Here, we present an extended-focus optical coherence microscopy system operating from the visible to the near-infrared wavelength range for high axial and lateral resolution imaging of cortical structures *in-vivo*. The system exploits an ultrabroad illumination spectrum centred in the visible wavelength range (λ_c = 650 nm, $\triangle\lambda\sim$ 250 nm) offering a submicron axial resolution ($\sim$ 0.85 μm in water) and an the extended-focus configuration providing a high lateral resolution of $\sim$ 1.4 μm maintained over $\sim$ 150 μm in depth in water. The system's axial and lateral resolution are first characterized using phantoms and its imaging performance is then demonstrated by imaging the vasculature, myelinated axons and neuronal cells in the first layers of the somatosensory cortex of mice *in-vivo*.

4.1.1   Introduction

Optical coherence tomography (OCT)[61] has emerged in the past decade as a valuable tool to study cerebral physiology[66, 75, 117, 175, 86], through its ability to perform three dimensional imaging of tissue and vasculature at very high acquisition rates, with A-scan rates typically ranging from 10 to 100 kHz. Although most OCT systems operate in the infrared spectral range to maximize the penetration depth in tissue, recent studies have exploited a visible light source to benefit from the characteristic spectral signatures of certain endo- and exogenous agents at shorter wavelengths[160, 154]. Such spectrosopic OCT systems have been used to increase the contrast of alzheimeric plaques in brain tissue[87] and to quantify hemoglobin concentration in the retina[161, 176] and in the brain[162, 89]. Shifting the central wavelength additionally enables increasing the axial resolution of OCT systems as it is determined by $\delta z \propto \lambda_c^2/_{\triangle\lambda}$, where λ_c is the central wavelength of the source and $\triangle\lambda$ is its bandwidth. Submicron axial resolutions can thus be reached by employing broadband sources in the visible wavelength range[177, 178, 87, 90, 81]. A higher lateral resolution is also gained through this illumination wavelength shift, as it is proportional to the ratio between the source's central wavelength λ_c and the objective's numerical aperture (NA). However, increasing the lateral resolution in conventional OCT systems reduces the depth-of-field (DOF) by restricting the confocal gating and effectively hampering the multiplexing advantage of Fourier domain OCT. As such, optical coherence microscopy[179] (OCM), the high-NA version of OCT, might require an additional scan in depth to obtain three-dimensional images[83, 85]. This effect can be mitigated by splitting the illumination

and detection modes of the OCM system and by illuminating the sample with so-called diffractionless beams, such as Bessel beams[72]. The resulting system, termed extended-focus OCM (xfOCM)[73] performs three-dimensional images with a high lateral resolution maintained over larger DOFs than conventional OCM setups (typically 3 to 10× larger). Recently, we developed a high resolution xfOCM platform, combining an ultrabroadband source spanning from the visible to the near-infrared wavelength range (from 500 to 850 nm) with high NA optics, to perform submicron resolution imaging of fixed brain slices and living cells[90]. Although its high resolution enables resolving subcellular structures, its ~ 60 µm DOF limits its compatibility with *in-vivo* cortical imaging. We therefore present a novel system based on our previous work, optimized for cortical imaging, where the lateral resolution was reduced to image over the entire penetration depth available with visible light (~ 150 µm). The system's resolution was characterized using a mirror and nanoparticles embedded in PDMS and its imaging performance was assessed by imaging fine cerebral structures, such as myelinated axons, capillaries and neuronal cells in the superficial somatosensory cortex of mice.

4.1.2 Methods

Extended-focus visible/near-infrared optical coherence microscopy system

The extended-focus visible/near-infrared optical coherence microscopy (xf-visOCM) system presented here is based on previous extended-focus OCM implementations[73, 77, 90] and is optimized for high resolution *in-vivo* cortical imaging. Briefly, light from a supercontinuum source (Koheras SuperK Extreme, NKT Photonics) is first filtered to obtain an illumination spectrum from the visible to the near-infrared wavelength range, passes through a polarizing beam splitter and is then coupled into the microscope. As shown in Fig. 4.1, at the microscope's core lies a Mach-Zehnder interferometer to permit splitting the Bessel illumination and Gaussian detection modes. The first beam splitter (BS1) of the interferometric configuration divides the incoming light into the reference and the illumination arm, where an axicon (176°, Asphericon) transforms the initial Gaussian beam into a Bessel beam. A series of telescopes guides the illumination beam through a pair of galvanometric scanners and through the sample arm where it is finally focused on the sample (i.e. mouse cortex) through a 10x objective (NA = 0.3, UPlanFl, Olympus). The backscattered light from the sample is collected by the objective, descanned and then guided to the Gaussian detection path by means of the second beam splitter of the Mach-Zehnder configuration (BS2), and finally coupled into the detection fiber and sent to the spectrometer. The reference arm comprises of a set of prisms of different glasses (BK7, SF6 and UVFS) to balance the dispersion present in the illumination and sample arms and the residual dispersion is precisely balanced through a fine-compensation unit [90]. The interference between the reference and sample light is recorded by a custom spectrometer, comprising of a grating (600 lines/mm, Wasatch Photonics), a custom objective (EFL = 100 mm) and a CMOS line camera (Basler, spL2048-140km). All 2048 pixels of the camera were used to record the spectral interferograms, spanning from 500 to 850 nm in wavelength. As shown in Fig. 4.1(a), a pair of masks are placed after the axicon lens and before the detection coupler to filter the spurious beams generated by the tip of the axicon and specular reflections originating from the sample respectively. Moreover, the polarization state of the illumination was fixed using a polarizing beam-splitter (PBS) and a linear polarizer (P) placed at the entrance of the microscope. In practice, we observed that without this configuration, the visibility of the fringes of the interferogram was low and not constant throughout the spectrum. These effects can be attributed to the spectral and polarization-dependent transmission of certain optical elements,

such as non-polarizing beam-splitters. By controlling the polarization of the illumination, the fringe visibility could ultimately be maximized.

Mouse preparation

All experiments were carried out in accordance to the Swiss legislation on animal experimentation (LPA and OPAn). The protocols (VD 3048) were approved by the cantonal veterinary authority of the canton de Vaud, Switzerland (SCAV, Département de la sécurité et de l'environnement, Service de la consommation et des affaires vétérinaires) based on the recommendations issued by the regional ethical committee (i.e. the State Committee for animal experiments of canton de Vaud) and are in-line with the 3Rs and follow the ARRIVE guidelines. The capabilities of the xf-visOCM system were assessed by imaging the superficial cortex of mice *in-vivo*. To this intend, the cortex of n = 3 c57bl/6 mice (3-4 month old, Charles River) was made optically accessible through an open-skull craniotomy. Mice were first anaesthetized using a solution of ketamine (80-100 mg/kg) and xylazine (14 mg/kg) injected intraperitoneally. Once asleep, their skull was exposed through an incision in the skin of their heads. A circular region of skull of 4 mm in diameter above the somatosensory cortex was drilled, excised and then sealed using a glass coverslip and dental cement. Finally, a fixation ring was placed on the sealed cranial window to minimize motion artefacts and facilitate the localization of the same cortical region over time. After the surgery, mice were allowed to recover for a period of a week. Prior to imaging, mice were anaesthetized using the same ketamine/xylazine mixture as mentioned above and once asleep, were placed on a custom head fixation system for imaging. The mice's eyes were kept moist using eye ointment and their body temperature was maintained at 36°C throughout the surgical procedure and the imaging sessions. Post-operative care consisted in daily subcutaneous injections of dexamethasone (0.2 mg/kg), carprofen (5 mg/kg) and buprenorphine (0.1 mg/kg) for 72 hours from the day of the surgery.

4.1.3 Results

xf-visOCM resolution characterization

The system's axial resolution was assessed using a mirror placed on the sample holder and by changing the length of the reference arm. As shown in Fig. 4.1(b), an axial resolution of ~ 1.1 μm in air (~ 0.85 μm in water) is preserved over the first ~ 200 μm in air (~ 150 μm in water) before significantly increasing and reaching > 5 μm by ~ 400 μm in air. The axial resolution was measured as the full width at half maximum (FWHM) of the axial point spread function (PSF) in linear scale. The lateral PSF of the system was interrogated by imaging a sample of 30 nm gold nanoparticles embedded in PDMS. From the acquired data, an average PSF for 7 different depths was obtained by extracting and averaging over 5 individual PSFs at each plane. The resulting PSFs over depth are displayed in Fig. 4.1(c), where the FWHM of the central lobe is maintained at ~ 1.4 μm over 150 μm in depth. At larger depths, the PSF slightly broadens due to the presence of additional sidelobes and by a decrease in the signal intensity (observable here through an increase in the background noise). This loss in intensity is caused by a combination of the shape of the axial profile of the Bessel beam and by the Gaussian apodization [79] and by the system's roll-off.
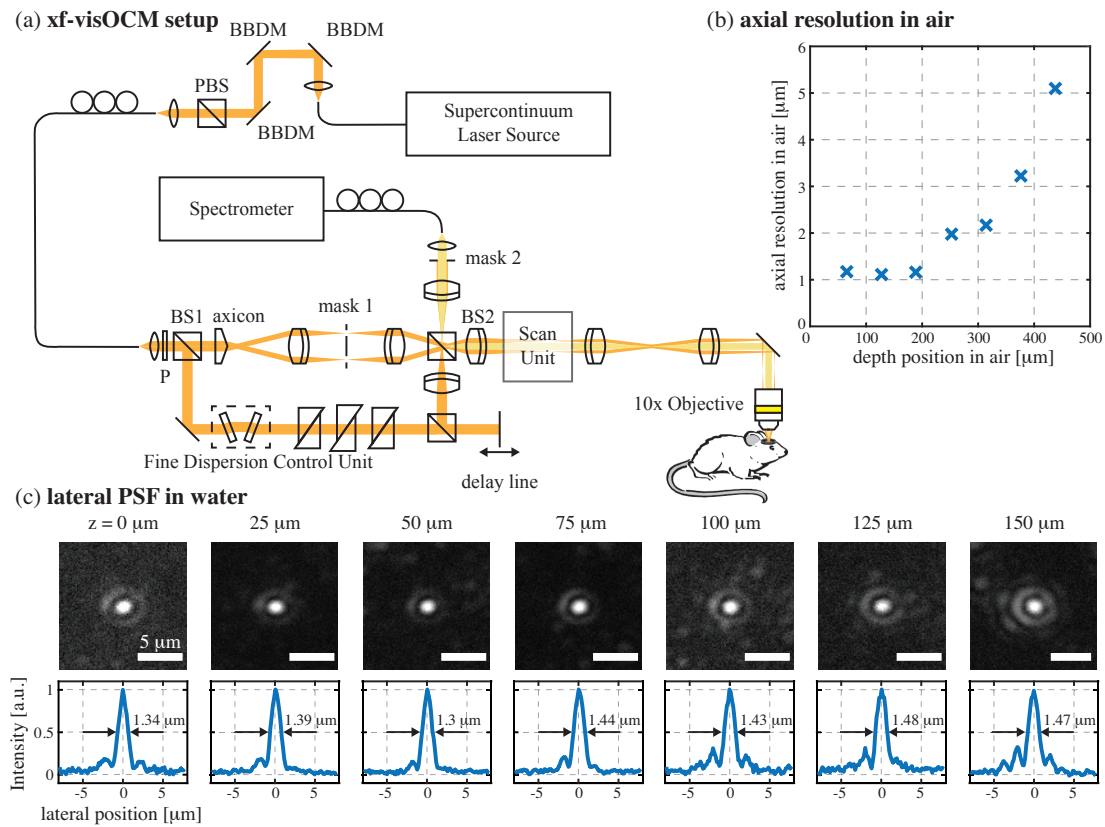
(a) **xf-visOCM setup**

(b) **axial resolution in air**

(c) **lateral PSF in water**

Figure 4.1 – xf-visOCM system and characterization: (a) Schematic of the microscope based on a Mach-Zehnder interferometer comprised of 2 beam-splitters (BS1 and BS2) to split the Bessel illumination and the Gaussian detection paths. A fine-dispersion compensation unit in the reference arm enable precisely compensating the dispersion of the interferometer and a 10x air objective focuses the light in the cerebral cortex of a mouse. BBDM: broadband dielectric mirrors, PBS: polarized beam splitter, P: linear polarizer, BS: beam splitter. (b) The ultrabroadband visible/near-infrared spectrum of the xf-visOCM system provides an axial resolution in air of ~ 1.1 µm over ~ 200 µm in depth before deteriorating to ~ 5 µm in air. (c) The full width at half maximum of the lateral point spread function of the xf-visOCM system is ~ 1.4 µm in water and is maintained over 150 µm in depth through the extended-focus configuration, as shown by both the heatmaps and their corresponding profiles (in linear scales). Scalebar: 5 µm

Chapter 4. *In-vivo* imaging of shallow cortical structures with extended-focus optical coherence microscopy in the visible spectrum

in-vivo **imaging of cortical structures**

With the system characterized, the imaging performance of the xf-visOCM platform was assessed by imaging the superficial cortex of mice. All images presented in this manuscript were acquired at a line rate of 20 kHz, with an incident power on the sample of 0.5 mW and were averaged over 5 volumetric acquisitions, i.e. C-scans. The imaging time for a single volumetric acquisition was from 2 to 4 minutes. Figures 4.2(a) and (b) show a B-scan and en-face views at different depths of the superficial cortex respectively. Similarly to previous observations of cortical structures using OCT[180, 75, 81, 85, 86, 82, 90, 178], dura mater (highlighted by green arrows) and myelinated axons (pointed by yellow arrows) are characterized by a stronger back-scattering than the neuropil and appear as bright layers and fibers respectively. The extended-focus capabilities of the system are illustrated in the en-face views presented in tile (b) showing the ability to resolve the fine bright myelinated axons throughout a depth of 80 μm. Myelinated axons can also be visualized at a depth of 30 μm from the cortical surface in another animal, as shown in Fig. 4.2(c). Additionally, through their increased back-scattering, these structures could be segmented from the parenchyma using a simple thresholding operation, similarly to Chong and Merkle et al. [176]. By adapting the threshold for attenuation in depth, the axons were segmented at different depths to obtain a depth-encoded maximum intensity projection (MIP) as presented in Fig. 4.2(d).

In addition to imaging neural fibers, the high resolution of the system permits discriminating fine features such as capillaries and the boundary of large vessels from the surrounding background. A fine dark region can be discerned within large vessels, below their membranes (blue arrow in Fig. 4.3(a)), as previously reported by Merkle and Chong et al.[178] and identified as a cell-free layer within the lumen of large calibre vessels. Similarly to our previous work in *ex-vivo* slices at higher lateral resolution[90], the lumen of capillaries can be distinguished from the neuropil as dark elongated structures, as shown by the red arrows in Fig. 4.3(a) and by the red arrows in the minimum intensity projections (MinIP) presented in Fig. 4.3(b) and (c) and Fig. 4.4(c). In contrast to slices where the reduced intensity was linked to the absence of scatterers in the lumen of the vessels, here the reduced back-scattering seems to be caused by the dynamic nature of the scattering of red blood cells (RBC). The images displayed Fig. 4.3 and 4.4 were obtained by averaging 8 to 16 B-scans acquired at the same lateral position (in addition to the 5× averaging over C-scans) and represent the low-pass filtered component of the back-scattering (i.e. its static component). Therefore, due to the motion and discrete nature of RBCs flowing in capillaries[118], the static contribution of their back-scattering is weaker than of the surrounding parenchyma, and appear darker than the tissue. The final pixel size of every en-face image shown in Fig. 4.2, Fig. 4.3 and 4.4 after filtering is 512×512.

Conversely, an angiogram, as presented in Fig. 4.3(d) and (e), can be obtained by filtering out the static component of the back-scattering[95, 181] (over 8 and 16 B-scan repetitions respectively). The high-pass filtering operation was performed through a point-wise complex subtraction of each B-scan[95]. The depth encoded MIPs presented in Fig. 4.3(d) and (e) were obtained by normalizing the angiogram with the structure as described by Srinivasan et al.[66, 83] to account for the reduced intensity in depth and alleviate the impact of bright structures in the shadows of large vessels (here mainly bright myelinated axons in the shadows of vessels, visible as bright dots in Fig. 4.3(e)). These angiograms highlight the presence of large pial vessels at the surface and the beginning of the cortical microvascular meshwork in deeper regions. Moreover, the location of capillaries in the angiogram coincide with the dark elongated structures reported in the MinIP Fig. 4.3(b) and (c) of the same figure
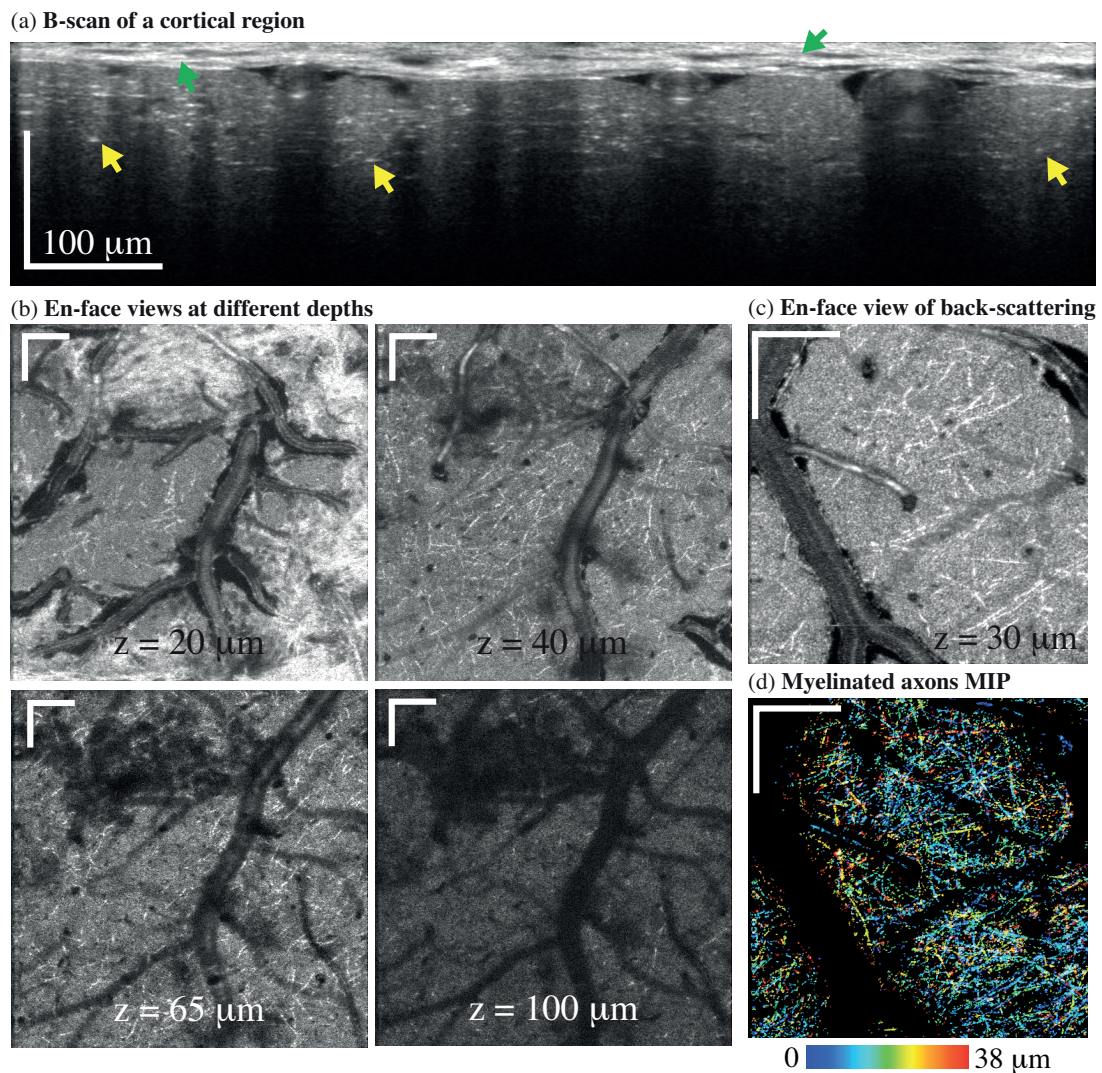
Figure 4.2 – xf-visOCM *in-vivo* imaging: The imaging capabilities of the xf-visOCM system were assessed by imaging the superficial cortex of mice. (a) A B-scan across the first ~100 μm in depth of the cortex highlights the different structures observable, such as bright, myelinated axons (pointed by yellow arrows) and dura mater (pointed by green arrows). (b) The en-face views at different depths present the same structures as in (a) and show the preservation of the lateral resolution in depth. (c) In another animal, myelinated axons can also be visualized in the en-face view at a depth of 30 μm from the cortical surface. A depth-encoded view of segmented myelinated axons exposes the dense distribution of these fibers within the first layer of the brain (d). Scalebars: 100 μm.

Chapter 4. *In-vivo* imaging of shallow cortical structures with extended-focus optical coherence microscopy in the visible spectrum

(a) B-scan of a cortical region

(b) Back-scattering MinIP

(c) Back-scattering MinIP

(d) Angiogram MIP
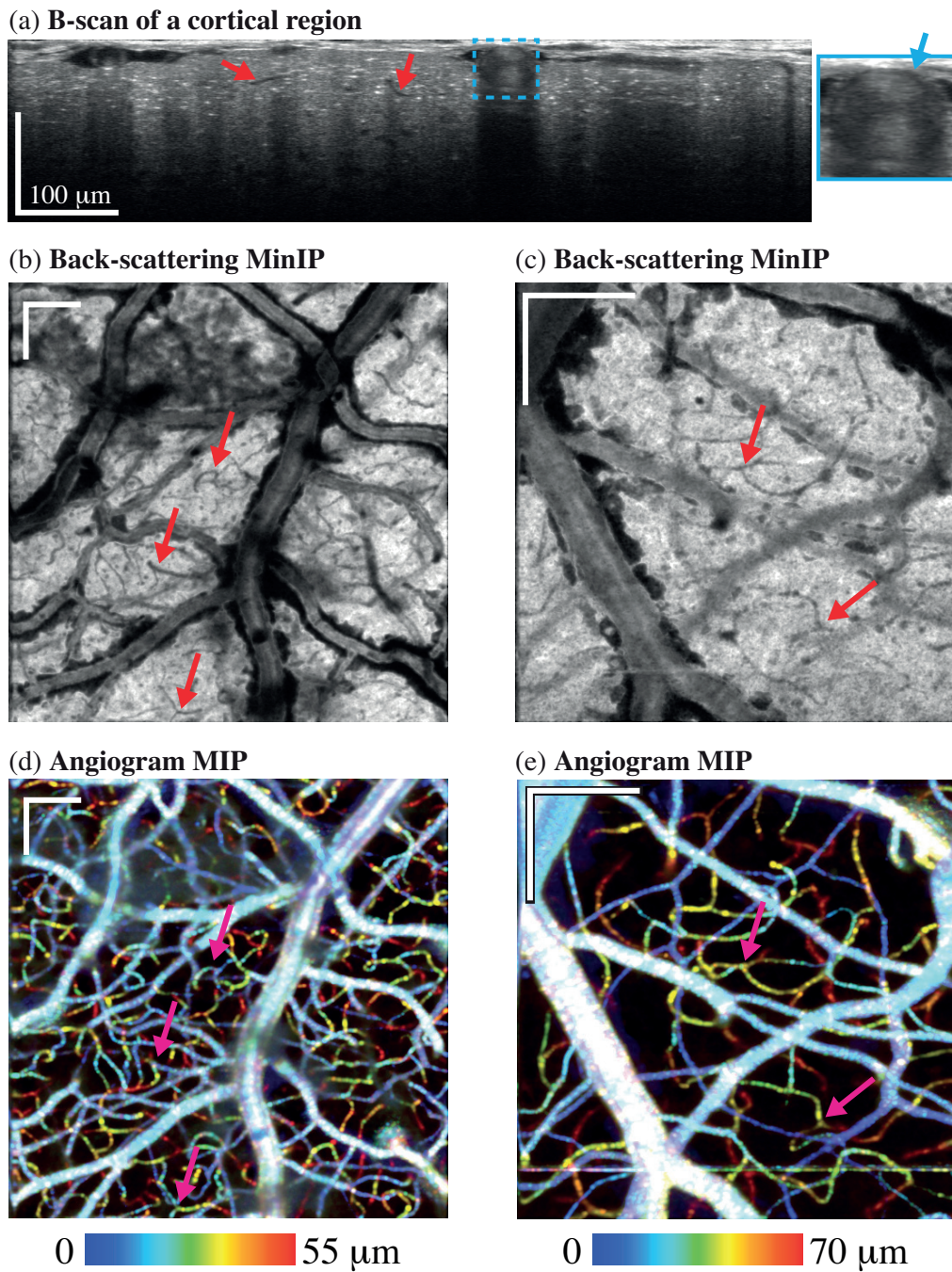

0 — 55 μm

(e) Angiogram MIP

0 — 70 μm

Figure 4.3 – xf-visOCM *in-vivo* vascular imaging: Owing to the high resolution of the xf-visOCM system, the microvasculature can be resolved both in the back-scattering tomograms and in the angiograms. (a) A B-scan covering the first ∼100 μm in depth of the cortex reveals large vessels at the surface and capillaries that can be resolved as dark elongated structures, as pointed by the red arrows. Moreover a close-up on the large caliber vessel reveals a thin dark cell-free layer below the vessels membrane (blue arrow). Vascular structures can be visualized by either performing a minimum intensity projection on the static back-scattering, in (b) and (c), or a maximum intensity projection on the angiogram, (d) and (e). Similar features are highlighted between the two visualizations by red arrows in (b) and (c) and pink arrows in (d) and (e). Scalebars: 100 μm

(a) **B-scan of region with neural cells**

(b) **En-face views of neural cells**

100 µm

z = 105 µm   z = 135 µm

(c) **MinIP from 35 µm to 85 µm**

(d) **MinIP from 85 µm to 120 µm**

(e) **depth encoded MinIP**
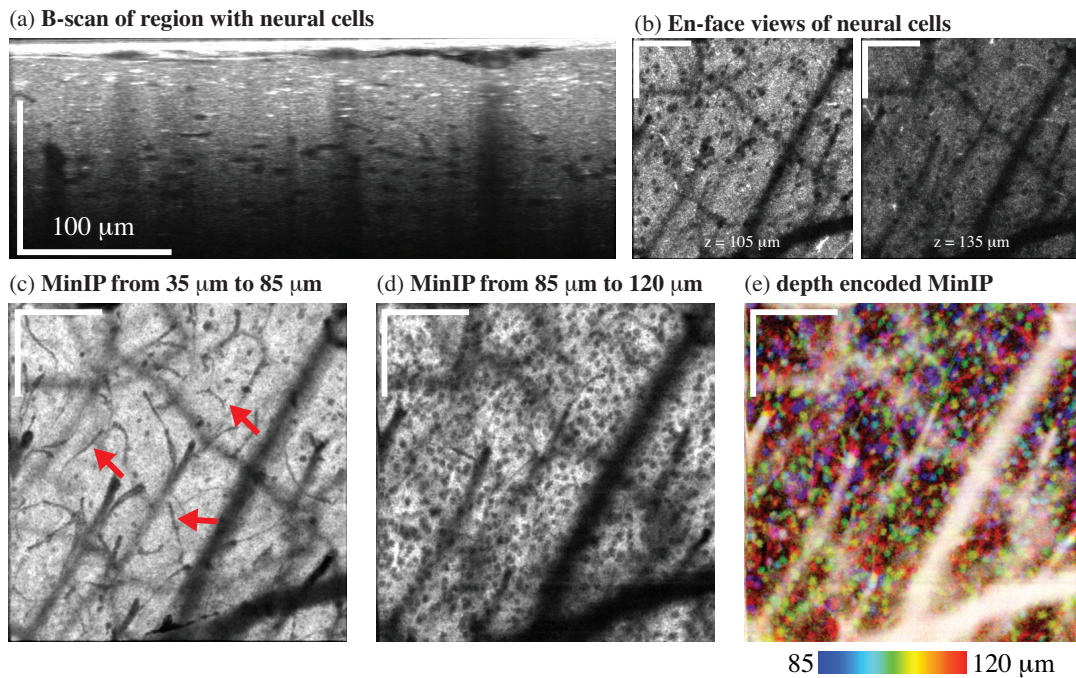
85 ▮▮▮ 120 µm

Figure 4.4 – xf-visOCM *in-vivo* imaging of neural cells: Neural cells can be identified in the back-scattering B-scan (a) and En-face views (b) as dark spheroids surrounded by the neuropil. These cells can be identified up to a depth of ∼ 135 µm. Fine features can be further visualized through minimal intensity projections, highlighting the presence of mainly vascular structures from 35 to 85 µm in depth (c), and neural cells from 85 µm and beyond (d). Capillaries can be identified in the MinIP by their hollow lumen, as highlighted by the red arrows in tile (c). The spatial distribution of these cell bodies can be appreciated by a depth color coded minimum intensity projection (e). Scalebars: 100 µm.

(highlighted by the red and pink arrows on Fig. 4.3(d) and (e) respectively), reinforcing our observation that capillaries can be distinguished as darker structures in the back-scattering images.

In contrast to OCT systems operating at longer wavelengths, the penetration depth of visible light is reduced to ∼ 150 µm in tissue[88, 87]. Nevertheless, as shown in Fig. 4.4, cell bodies located at ∼ 100 µm in depth can be resolved in the B-scan and in the en-face views presented in tiles (a) and (b) (temporally averaged frames). Similarly to other observations of cell bodies in the visible range and using other illumination spectra[83, 81, 117, 85, 82], these cell bodies appear as spheroids with a lower intensity than the surrounding parenchyma and their visualisation can be further enhanced through a minimum intensity projection, as presented in Fig. 4.4(d) and (e). Moreover, MinIPs at different depths, as shown in Fig. 4.4(c–e), hint to the laminar organisation of the cortex, where the first ∼ 85 µm are almost devoid of these cell bodies and display a sparse microvascular network, whereas deeper regions show a dense population of cells. Figures 4.4(d) and (e) were obtained by shifting the focus slightly deeper within the cortex, to counteract the attenuation of light. Overall, the shape, contrast and depth distribution (highlighted in Fig. 4.4(e)) of these cells coincide with the presence of neural cells in the first part of layer II/III of the rodent cortex[83, 117, 82].

Journal article

4.1.4   Conclusion and discussion

In this manuscript, we presented a novel extended-focus optical coherence microscopy system operating from the visible to the near-infrared wavelength range and optimized for *in-vivo* superficial cortical imaging. Although its illumination spectrum inherently limits the depth penetration abilities of the platform, the coherent amplification property of OCT enables imaging up ~ 150 µm. As shown in the system's characterization, the extended-focus configuration maintains a lateral PSF FWHM of ~ 1.4 µm over the entire available penetration depth, and the ultrabroadband spectrum offers a submicron ~ 0.85 µm axial resolution. Although dispersion was balanced between both arms of the interferometer, additional dispersion caused by tissue could affect the optical sectioning at large depths. Moreover, as shown in Fig. 4.1(b), the axial resolution degrades rapidly beyond > 200 µm from the zero delay line, and could further deteriorate the system's performance. Future improvements on the setup will involve using longer line cameras (i.e. with more pixels) to improve the spectrum's sampling as used by Lichtenegger et al.[87]. We used the system to image the first layers of the somatosensory cortex of mice, showing the ability of the xf-visOCM system to resolve cerebral structures such as myelinated axons, vessels through both static and dynamic back-scattering and neural cells. The combined extended-focus property of the Bessel-Gauss configuration and the broadband spectrum enabled imaging at a high lateral resolution over the entire penetration depth and at a submicron axial resolution. Overall, we believe that the performance and imaging capabilities of the xf-visOCM system make it an attractive tool to study cerebral physiology in health and in disease[75, 182], *in-vivo* and at high resolution.

Disclosures

The authors declare that there are no conflicts of interest and no competing interests related to this article.

5 Deep cortical imaging with extended-focus OCT

U NDERSTANDING brain function requires imaging deep within cerebral tissue *in-vivo*, as several neuronal processes occur between the cortex and deeper regions and neuropathological disorders, such as Alzheimer's and Parkinson's disease, affect subcortical structures. In view of this, two main avenues have been pursued to enable imaging deeper with OCT, by either increasing the central wavelength of the system or by using optimized sources. Shifting the illumination spectrum to the infrared range reduces the scattering experienced by light in tissue and enables imaging at larger depths. However, as tissue is primarily composed of water, care must be taken when selecting the spectral region as its absorption also increases in the infrared. As such, so-called *imaging windows* exist in the infrared: up to 1.4 µm, between 1.6 and 1.8 µm and between 2 and 2.2 µm [183, 184]. Although no OCT systems currently operate in this latter range, OCT technology at 1.3 µm is already mature and an increasing number of setups at 1.7 µm are being developed. The lack of optimized line cameras and optics beyond 1.6 µm initially restricted the development of OCT platform to time-domain systems which enabled reaching a depth of ~ 1.2 mm in the brain [185]. Recently, spectral domain systems have emerged in this spectral window using novel frequency-swept sources [119] and custom line-cameras [88, 186]. Chong et al. developed such a Fourier-domain system to image subcortical structures in the brain *in-vivo* up to a depth of 1.5 mm with a 5.6 µm axial resolution in tissue [88]. Kawagoe et al. developed an OCT system with an ultrabroad spectrum spanning from 1.4 µm to 2 µm to reach deep structures while maintaining a high axial resolution of 3.6 µm in tissue [186]. Nevertheless, line cameras in the IR being limited in pixels, imaging such a broad spectrum reduced the available imaging depth. As such, a phase modulation system was implemented to eliminate the complex conjugate term of Eq. 1.14, also termed ghost artefact, overlapping at large depths, similarly to Bachmann et al. [187]. Overall, these systems enabled reaching larger depths and imaging subcortical structures but are still limited by the lack of optimized optics and cameras (although swept-source systems already exist, with a limited bandwidth [119]). The alternative path towards reaching larger depths with OCT deals with optimizing the system parameters such as the system's roll-off. To this end, Choi et al. used a novel MEMS VCSEL swept-source system at 1.3 µm with an extremely low roll-off (through very narrow frequency lines) and demonstrated its capabilities in reaching 2.3 mm in depth in the mouse brain *in-vivo* [188]. Nevertheless, most swept-source systems suffer from phase instabilities and have small bandwidths, limiting their axial resolution. Ultimately, although such systems allow imaging deeper structures,

their lateral resolutions are typically low (i.e. $\sim$ 15 μm) and decay rapidly throughout the imaging depth, hampering their use for concurrently tracking hemodynamic changes over the entire depth range. In this regard, xf-OCT systems are ideally suited as they provide a diffraction-less illumination in depth. Such configurations have been developed in the IR for dermatology using relatively narrowband frequency-swept sources, reaching powers of 7 mW at the sample with a low axial resolution of 10 to 12 μm [78, 189, 190]. Conversely, current xf-OCT systems designed for cerebral imaging all operate at shorter central wavelengths and have high lateral and axial resolutions, but are limited in penetration to the first layers of the cortex (up to layer IV) [75, 82, 191]. In view of this, the journal article in this chapter presents an xf-OCT system using a broadband SLD source centred at 1.3 μm optimized for deep tissue cerebral imaging at high axial resolution, with a lateral resolution maintained over almost the entire cortical depth.

5.1 Journal article

Imaging of cortical structures and microvasculature using extended-focus optical coherence tomography at 1.3 μm

Paul J. Marchand,[1] Daniel Szlag, [1] Jérôme Extermann, [1]Arno Bouwens,[1] David Nguyen, [1] Markus Rudin,[2] and Theo Lasser[1]

[1]Laboratoire d'Optique Biomédicale, École Polytechnique Fédérale de Lausanne, CH-1015 Lausanne, Switzerland;

[2] Institute for Biomedical Engineering, Swiss Federal Institute of Technology (ETH) Zurich, Wolfgang-Pauli-Strasse 10, 8093 Zurich, Switzerland

Extended-focus optical coherence tomography (xf-OCT) is a variant of optical coherence tomography (OCT) wherein the illumination and/or detection modes are engineered to provide a constant diffraction-less lateral resolution over an extended depth of field (typically 3 to 10× the Rayleigh range). xf-OCT systems operating at 800 nm have been devised and used in the past to image brain structures at high resolution *in-vivo* but are limited to ~ 500 μm in penetration depth due to their short illumination wavelength. Here, we present an xf-OCT system optimized to image deeper within the cortex by using a longer illumination central wavelength of 1310 nm. The system offers a lateral resolution of 3 μm and 6.5 μm, over a depth of 900 μm and >1.5 mm using a 10× and 5× objective respectively, in air. We characterize the system's resolution using microbeads embedded in PDMS and demonstrate its capabilities by imaging the cortical structure and microvasculature in anesthesized mice to a depth of ~ 0.8 mm. Finally, we illustrate the difference in penetration depths obtainable with the new system and an xf-OCT system operating at 800 nm.

Over the past decades, optical coherence tomography (OCT)[61] has become an important tool for studying cortical physiology and hemodynamics, through its ability to perform label-free imaging of large volumes at high-acquisition rates [66, 75, 89, 188, 84]. Recent interest has been focused on increasing the depth penetration of OCT in brain tissue by shifting the illumination to longer wavelengths [192, 88, 185] or by minimizing the system's roll-off [188]. However, increasing the depth of field (DOF) of conventional OCT systems typically comes at the cost of a lower lateral resolution (>15 μm), preventing the imaging of small features such as capillaries. Extended-focus configurations have been devised for OCT (xf-OCT), where the illumination and detection beams are engineered to increase the DOF while maintaining a constant transverse resolution [73]. Although some xf-OCT systems operate in the infrared spectral range [78, 189], to our knowledge, none have been designed and used for *in-vivo* cortical imaging. Current xf-OCT systems used for cerebral imaging operate at 800 nm [75, 82], where the strong tissue scattering limits the imaging depth to ~ 500 μm. We present here a novel xf-OCT system, operating at 1.3 μm, optimized for cortical imaging. The instrument combines a broadband illumination in the infrared spectral range, with two magnifications (5× and 10×) for

capillary-level resolution imaging over a large depth of field (almost an entire cortical column).
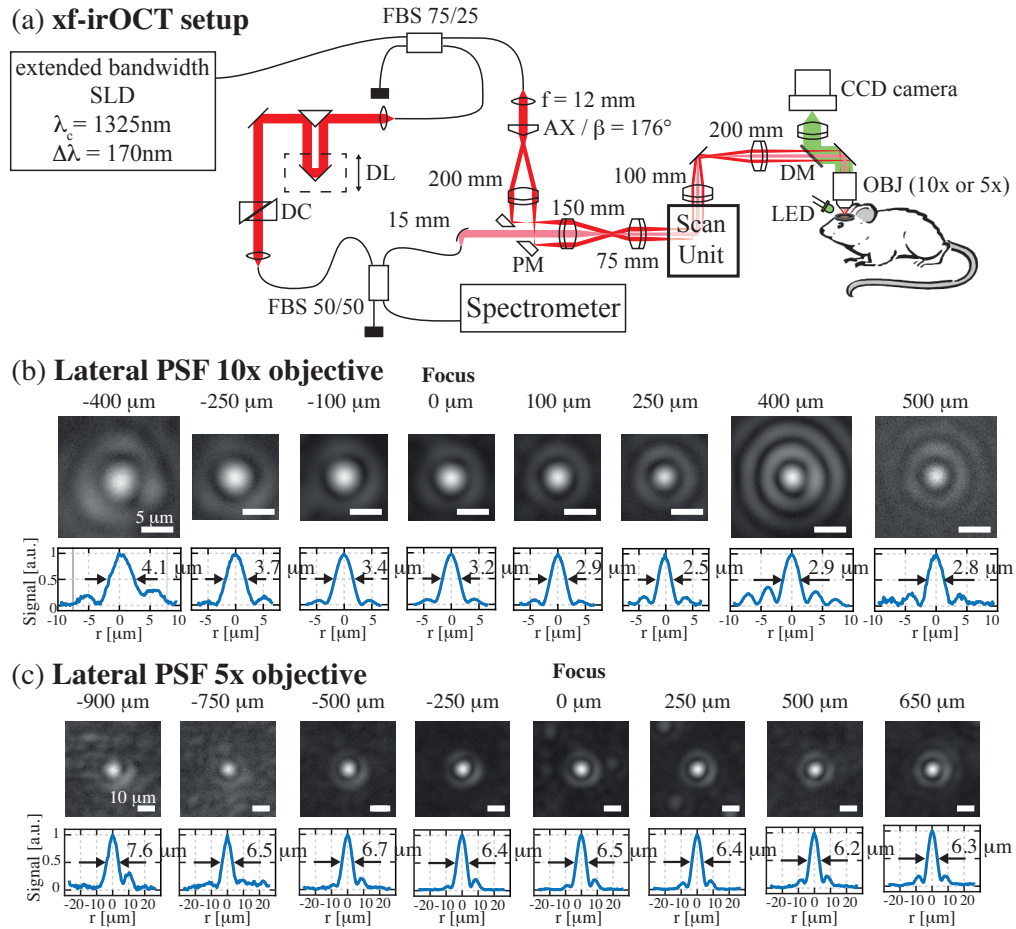

Figure 5.1 – xf-irOCT system design and performance: (a) Simplified schematic showing the fiber based xf-irOCT system, with a pierced mirror (PM) splitting the illumination and detection modes. Light is focused on the sample by either a 5× or a 10× objective. DC: disperison correction, DL: delay line, FBS: fiber beamsplitter, AX: axicon, DM: dichroic mirror, OBJ: objective.(b) The 10× objective provides a lateral resolution of ~ 3 µm maintained over ~ 900 µm in depth, whereas with the 5× objective, a lateral resolution of ~ 6.5 µm is obtained, conserved through ~ 1.5 mm in depth (c). All measurements are in air. Scalebar: 5 µm.

The extended-focus infrared OCT system (xf-irOCT) is based on a Mach-Zehnder interferometer, allowing the illumination and detection modes to be split. Briefly, and as shown in Fig. 5.1(a), light from an extended-bandwidth SLD (LS2000C, Thorlabs, NJ) is divided into the illumination and reference arm with a 75/25 splitting ratio. The illumination beam passes through a 176° axicon (X25-020FPX-U-C, Asphericon), is reflected by a pierced mirror and is then relayed through the scan-unit (6210H, CamTech) and the rest of the microscope by telescopes, where it is finally focused on the sample by either a 5× or a 10× IR objective (LMPLN5XIR, LMPLN10XIR, Olympus). The back-scattered light is collected by the objective, descanned by the scan-unit, passes through the pierced mirror and is then coupled to the detection mode fiber. The reference and detection light are coupled by a second fiber beam splitter (50/50 ratio) and the interference pattern is recorded by a custom spectrometer comprising an InGaAs linescan camera (1024-LDH2, Sensors Unlimited). Overall, the core of the xf-irOCT system is based on previous xf-OCT platforms with an emphasis on minimizing power losses and

increasing the efficiency of the system's illumination. In contrast to systems operating at 800 nm using femtosecond sources offering up to 400 mW, the power available with current broadband sources at 1.3 µm is significantly lower, typically ~ 10 mW. We therefore traded a beamsplitter for a custom-designed pierced mirror (Eksma optics), with a 4 mm diameter inner hole to split the illumination and detection modes, reflecting the ~ 6.2 mm diameter Bessel ring and transmitting the ~ 2.7 mm diameter Gaussian beam. We also used a 75/25 fiber beamsplitter to increase the illumination power and finally optimized the overall optical design so as to improve the efficiency of the Bessel illumination. We opted for a smaller axicon angle and a shorter axial extent to minimize the illumination's Fresnel number (here N≃7) [193]. The power at the input of the illumination path and after the objective are ~ 6.5 mW and ~ 2.5 mW respectively. These power losses are mainly attributed to imperfections in the axicon. A list of the optical parts used for the system is available on https://wiki.epfl.ch/xf-iroct.

The lateral point spread function (PSF) of the system was interrogated using a sample consisting of 1 µm polystyrene beads embedded in a PDMS slab. The lateral resolution was measured as the full width at half maximum of the lateral PSF. Figures 5.1(b) and (c) show the resulting PSFs at different depths for both 10× and 5× objectives, which demonstrate the preservation of a ~ 3 µm and ~ 6.5 µm lateral resolution over 900 µm and 1.5 mm for the 10× and 5× objectives respectively. At large distances from the focus, the transverse extent of the Gaussian detection is enlarged and the PSFs show additional side rings, a typical characteristic of the Bessel illumination. Moreover, a slight broadening of the Bessel's central lobe is observed at -250 µm and beyond with the 10× objective, which is likely caused by imperfections of the axicon's tip. The axial resolution of the system, given by the source's coherence length and thus related to its bandwidth, was measured to be 4.6 µm in tissue and the roll-off of the spectrometer was measured as 7.5 dB/mm.

Having characterized the system's resolution, we imaged the cortex of mice *in-vivo*. Optical access to the brain was obtained in ~ 3-month-old c57bl/6 mice (Charles River, n = 8) through a 4 mm diameter circular open-skull craniotomy over the somatosensory area, which was covered by a glass coverslide and sealed with dental cement.

All experiments were carried out in accordance to the Swiss legislation on animal experimentation (LPA and OPAn). The protocols (VD 3048) were approved by the cantonal veterinary authority of the canton de Vaud, Switzerland (SCAV, Département de la sécurité et de l'environnement, Service de la consommation et des affaires vétérinaires) based on the recommendations issued by the regional ethical committee (i.e. the State Committee for animal experiments of canton de Vaud) and are in-line with the 3Rs and follow the ARRIVE guidelines. The mice were anesthetized with a mix of ketamine/xylazine (80-100 mg/kg, 14 mg/kg) for both the cranial window implantation and the imaging sessions. Pre- and post-operative care consisted in subcutaneous injections of Buprenorphine (0.1 mg/kg), Carprofen (5 mg/kg) and Dexamethasone (0.2 mg/kg). For all of the measurements presented in this manuscript, the camera's frame rate was set to 23 kHz and the average power incident on the sample was measured to be ~ 2.5 mW for both objectives.

An assessment of the *in-vivo* imaging performance of both objectives (5× and 10×) is presented in Fig. 5.2, showing cross-sectional imaging of both vasculature and back-scattering (panels (a) and (e)) and en-face maximum intensity projections (MIP) of the vasculature at selected depths (panels (b) and (f)) and their corresponding close-ups. The static back-scattering and vasculature were obtained through a low-pass and high-pass filtering over 8 repeated B-scan acquisitions at the same transverse location respectively. In practice, the low-pass operation was obtained by averaging of the complex OCT signal over the inter-frame repetitions, whereas a complex point-wise subtraction was used for

Journal article

the high-pass filtering [95]. Phase correction was applied prior to filtering [?]. The achievable depth of both angiographic and static back-scattering imaging differ significantly. Using a 5× objective, the deepest resolvable vessel is observable at ∼ 800 µm in depth, whereas static back-scattering seemingly is collected throughout almost the entire imaging depth range (∼ 1.4 mm), and could enable imaging subcortical structures, as hinted to in Fig.5.3. The diameter of capillaries was measured at selected depths, as shown in Fig. 5.2(c), showing an almost constant preservation of the lateral resolution from the surface and up to ∼ 700 µm. The increase in capillary diameter shown at 800 µm can be caused by the lower SNR of the angiogram at this depth or by a loss in resolution caused by tissue. Profiles of capillaries were also measured at different depths and are presented in Fig. 5.2(d), highlighting the ability of xf-irOCT to perform angiography up to 800 µm in depth. With the 10× objective, a reduced depth of field is traded for a higher lateral resolution, as illustrated in the angiogram cross-section of Fig. 5.2(c). Similarly to the 5× objective, back-scattering signal is collected over a larger depth than in the angiogram, and almost throughout the entire depth of the cortex. By placing the focus at ∼ 500 µm from the cortical surface, the capillary bed could be resolved from ∼ 400 µm to ∼ 700 µm in depth, as shown in the en-face MIPs and zoom-ins of Fig 5.2(f). Capillary diameters and profiles were also measured at selected depths, as shown in Fig. 5.2(g) and (h) respectively, showing a preservation of the resolution from 400 µm to 700 µm in depth.

As mentioned in the introduction, the penetration depth in cortical tissue of previous xf-OCT systems is limited to ∼ 500 µm due to their shorter illumination wavelength. Shifting the source into the infrared spectral range enables imaging deeper, i.e. throughout the entire depth of the mouse's cortex. This is illustrated in Fig. 5.3, where we performed back-scattering and angiographic imaging on the same mouse with an xf-OCT at 800 nm [75] and our novel xf-irOCT system. Although the axial and lateral resolution of the near-infrared system is higher (∼ 1.5 µm and ∼ 2.5 µm respectively, in water) as the central wavelength is shorter, the signal intensity decades rapidly beyond ∼ 400 µm in the back-scattering tomogram. This effect is more pronounced in the angiogram, where the deepest detectable vessel lies at ∼ 300 µm from the cortical surface. For this comparison, the 800 nm xf-OCT system's acquisition frequency was set at 23 kHz and the illumination power was measured as ∼ 12 mW after the objective. In contrast, the xf-irOCT system can reach depths of ∼ 1.2 mm and ∼ 800 µm for back-scattering and angiographic imaging, respectively, with a power of ∼ 2.5 mW.

Overall, we presented a novel xf-irOCT system for cortical imaging, wherein its design was optimized to minimize power losses and its illumination wavelength was shifted to the infrared to increase the penetration depth in cortical tissue compared to previous xf-OCT instruments used for brain imaging. In contrast to xf-OCT at 800 nm reaching depths of ∼ 500 µm in tissue, the xf-irOCT system can image the vasculature and the static back-scattering up to ∼ 800 µm and >1.2 mm in depth, respectively. In addition to the increased penetration depth, the conservation of the system's lateral resolution is of paramount importance for OCT velocimetric methods, where the size of the focal volume typically influences the accuracy of the metric [148, 119, 84]. Using a Bessel illumination could therefore increase the axial extent of the measurements and provide more accurate measurements away from the focus, if the Bessel's sidelobes are adequately dealt with. The current implementation is limited by the power losses throughout the system (i.e. imperfections of the axicon's tip) and the available power of current broadband SLD sources. Using higher power sources, novel frequency swept-sources and ultimately even longer illumination wavelengths could allow imaging deeper by increasing the number of collected photons, relaxing the deleterious roll-off of spectral domain systems and reducing light scattering [188, 88, 185]. Future work will also focus on validating the optical system for velocimetric
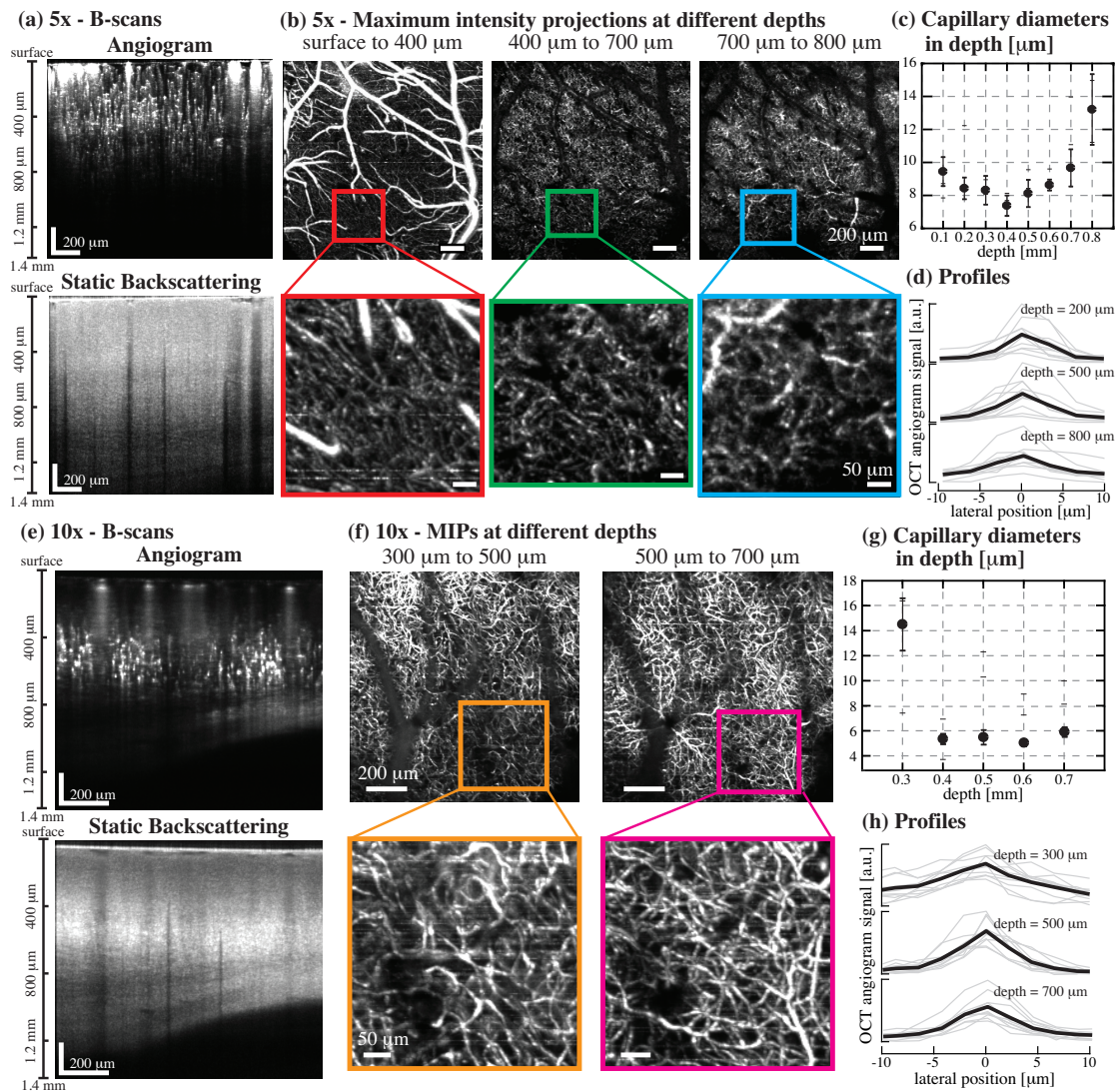
(a) 5x - B-scans

(b) 5x - Maximum intensity projections at different depths

(c) Capillary diameters in depth [μm]

(d) Profiles

(e) 10x - B-scans

(f) 10x - MIPs at different depths

(g) Capillary diameters in depth [μm]

(h) Profiles

Figure 5.2 – Cortical imaging using xf-irOCT: The system's performance for two objectives (5× and 10×) was assessed through back-scattering and angiographic imaging of a mouse's cortex. Tissue back-scattering and vasculature images were obtained by placing the focus of the objective in the middle layers of the cortex, as shown in B-scans (a). The en-face MIPs at selected depths and their corresponding zoom-ins show the xf-irOCT's capability to resolve vascular structures up to 800 μm in depth. Measurements of the diameters of capillaries across depth highlight the preservation of the resolution throughout ∼ 700 μm in brain tissue (c). Profiles of capillaries at different depths are shown in (d) where the mean profile is highlighted in bold. Using a 10× objective, the lateral resolution is increased, resulting in a shorter axial extent, as visible in the cross-sectional images of vasculature and tissue back-scattering (e). Nevertheless, its higher lateral resolution enables finely resolving the vasculature in the en-face MIPs at various depths (f) Using the 10× configuration, capillary diameters can be measured from 400 to 700 μm in depth in brain tissue. Profiles of capillaries measured using the 10× objective are shown in (h). Scalebars: 200 μm for all images apart from the zoom-ins, 50 μm for the zoom-ins.

(a) xfOCT at 800 nm

surface

(b) angiography xfOCT at 800 nm

200 μm

400 μm

600 μm

200 μm

200 μm

(c) xfOCT at 1.3 μm

surface

(d) angiography xfOCT at 1.3 μm

200 μm

400 μm

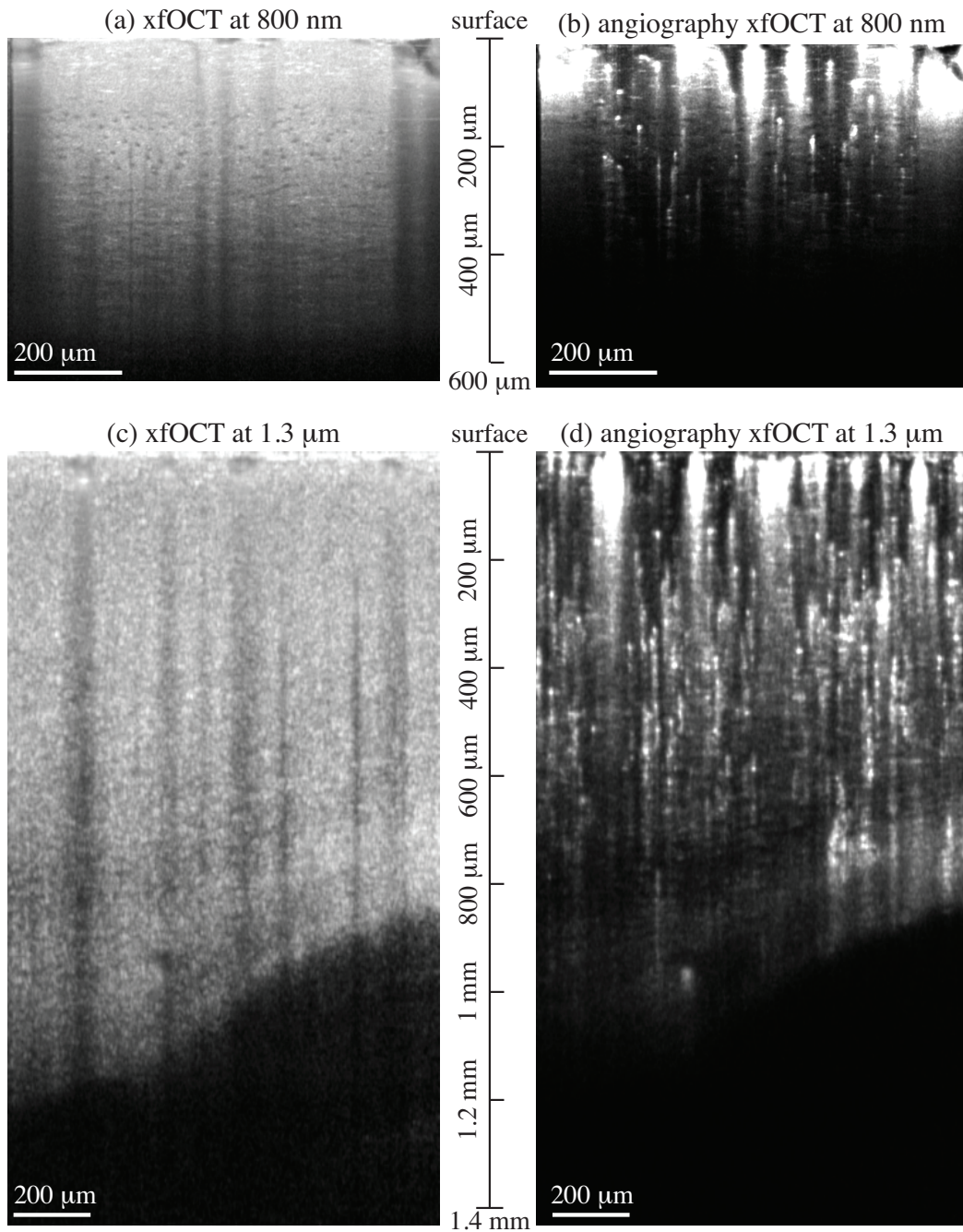600 μm

800 μm

1 mm

1.2 mm

1.4 mm

200 μm

200 μm

Figure 5.3 – xf-OCT 800 nm versus 1.3 μm comparison: The depth performance of both systems for back-scattering and angiographic imaging were assessed on the same mouse. The 800 nm system enables imaging across ~ 400 μm and ~ 250 μm in back-scattering and in angiograms, as shown in the cross-sectional images (a) and (b). Whereas the xf-irOCT can resolve structures (c) and vessels (d) up to >1.2 mm and >800 μm respectively. Scalebars: 200 μm.

measurements using Doppler OCT and other existing OCT velocimetry protocols.

Funding Information

Journal article

5.2 Technical notes

5.2.1 Optical design

The xf-irOCT system was designed to achieve deep cortical imaging at a high axial resolution, while maintaining a capillary-level lateral resolution throughout an extended imaging depth. Ultimately, the desired system should have a lateral resolution of ~ 3.5 μm and 7 μm, maintained over > 500 μm and 1 mm, with a 10× and 5× objective respectively. As mentioned in the journal article, in contrast to previous xf-OCM implementations (xf-OCM and visOCM) where the source could deliver > 50 mW, broadband SLDs in the IR spectral range are limited to ~ 10 mW. The system was therefore designed so as to minimize power losses and increase the illumination's efficiency. Bessel beams contain a large amount of power in their sidelobes, making them less susceptible to obstructions along their propagation [70]. Nevertheless, this power distribution ultimately leads to less power in the central lobe and thus a lower illumination efficiency [193]. Moreover, it might be tempting to design an elongated Bessel beam along the axial dimension, to ensure a large imaging depth and a good resolution preservation. However, in the context of illumination efficiency, such a design would be problematic for two reasons. The first relates to the presence of siderings in the detections: as mentioned before, the most common design of xf-OCT systems combines a Bessel illumination with a Gaussian detection. As such, the detection beam is dictated by Gaussian beam propagation and thus experiences defocus. Consequently, far from the focus, the total PSF of the system (obtained by multiplying the illumination and detection PSFs) will exhibit several sidelobes, unfiltered by the large support of the defocused Gaussian spot. This will therefore deteriorate the overall lateral resolution of the system. Secondly, an analysis by Lorenser et al. revealed that such a design (very extended and narrow Bessel beam) requires a large amount of power to be distributed in the Bessel's siderings, reducing the power in the central lobe and hindering the illumination efficiency [193]. Based on their observations, they prone the use of the system's Fresnel number to evaluate the design's power efficiency. In the case of Bessel illuminations, the Fresnel number is given by $N = \frac{w \cdot \beta}{\lambda}$, where w is the waist of the Gaussian beam prior to its conversion into a Bessel beam, β is the axicon's angle (also called axicon's numerical aperture) and λ is the central wavelength of the source. According to the authors, an xf-OCT system with a Fresnel number N<10 is a good compromise between depth of focus extension and illumination efficiency (SNR penalty). In addition to improving the illumination's efficiency, the design of the interferometer was also modified from our previous implementations (xf-OCM at 800nm and visOCM system) to minimize power losses throughout the system. Similarly to Blatter et al., the illumination and detection modes were split spatially [78]. Instead of a small mirror placed at the Fourier plane of the axicon, we used a pierced mirror to facilitate the alignment. This feature requires the detection and illumination modes to be spatially separated. Moreover, as in Blatter et al., the ratio of the fiber-beamsplitter delivering the source to the reference and illumination paths departed from the 50/50 configuration of previous implementations (here we used a 75/25 splitter).

By developing the relation given by Leitgeb et al. [73], the position of the first zero of the Bessel function after propagating through the entire illumination system, shown in Fig. 5.4(a), is given by:

$$r_\beta = \frac{1.202 \cdot \lambda_c}{\pi} \cdot \frac{1}{n \cdot \sin\left(\beta \cdot \frac{f_{ill_1}}{f_{det_1}} \cdot \frac{f_{scan_1}}{f_{scan_2}} \cdot M'_{obj}\right)}, \tag{5.1}$$
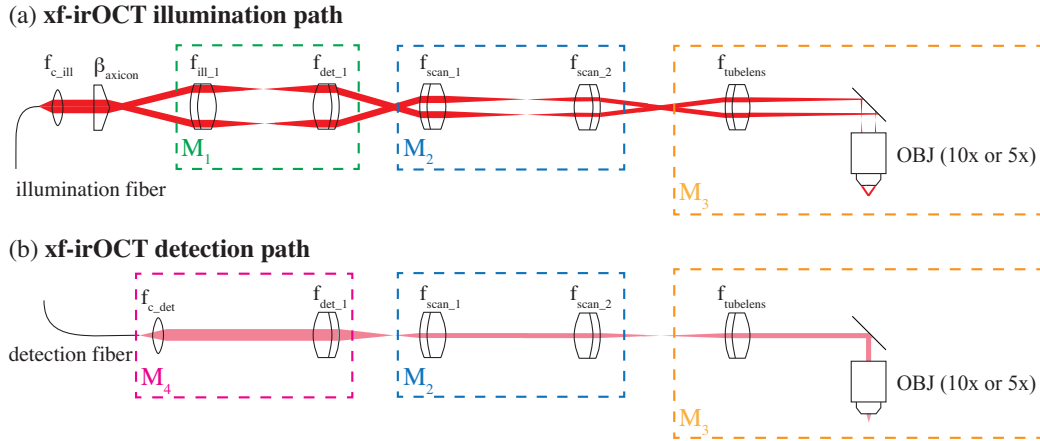
(a) **xf-irOCT illumination path**

(b) **xf-irOCT detection path**

Figure 5.4 – Design of the xf-irOCT system splitting the illumination (a) and detection arms (b) of the interferometer

where λ_c is the central wavelength of the source, n is the immersion's refractive index, β is the angle of the axicon and f_{ill1}, f_{det1}, f_{scan1} and f_{scan2} are the focal lengths of the different lenses in the system, as depicted in Fig. 5.4(a). The magnification of the objective M'_{obj} is adjusted to account for the potential change in the tubelens' focal length (i.e. not using a 180 mm tubelens for Olympus objectives).

The axial extent of the Bessel beam is given by:

$$z_\beta = 0.8 \cdot \frac{w}{\tan(\beta) \cdot \left(\frac{f_{ill_1}}{f_{det_1}}\right)^2 \cdot \left(\frac{f_{scan_1}}{f_{scan_2}}\right)^2 \cdot \left(M'_{obj}\right)^2}, \tag{5.2}$$

where w is the waist of the Gaussian beam prior to traversing the axicon, and is defined by the focal length of the collimator $f_{c_{ill}}$ and the mode-field diameter of the fiber w_{MFD}:

$$w = \frac{\lambda_c \cdot f_{c_{ill}}}{\pi \cdot \frac{w_{MFD}}{2}} \tag{5.3}$$

The lateral resolution of the Gaussian detection is given by imaging the mode-field diameter of the detection fiber through the detection system[a], as depicted by Fig. 5.4(b):

$$r_G = \frac{w_{MFD}}{2} \cdot \frac{f_{det_1}}{f_{c_{det}}} \cdot \frac{f_{scan_2}}{f_{scan_1}} \cdot \frac{1}{M'_{obj}} \tag{5.4}$$

Using these equations, the Fresnel number and the fact that the illumination and detection modes need to be spatially separated, the system was designed as shown in Table 5.1. The performance of the system using these parameters is presented in Table 5.2. using Eq. 5.1, 5.2, 5.3 and 5.4 and $M'_{obj} = \frac{180}{f_{tube}} \cdot M_{obj}$.

As such, the requirements listed at the beginning of this section are fulfilled. The resolution obtained for the 10× configuration are in good agreement with the performance of the final system shown in

---

[a] Provided the NA of the objective is sufficient to image the fiber at the sample.

Optical element	Optical parameter	Value
Source	central wavelength λ_c	1310 nm
Axicon	angle β	176°
Fiber	Mode-field diameter w_{MFD}	9.2 μm
	$f_{c_{det}}$	15 mm
	$f_{c_{ill}}$	12 mm
	f_{ill_1}	200 mm
	f_{det_1}	150 mm
Lens	f_{scan_1}	75 mm
	f_{scan_2}	100 mm
	f_{tube}	200 mm
	M_{obj}	5× or 10×
	NA_{obj}	0.1 or 0.3
Immersion	$n_{immersion}$	1

Table 5.1 – xf-irOCT design parameters

Parameter	Value	
	10× configuration	5× configuration
Bessel first zero r_β	2.9 μm	5.8 μm
Bessel axial extent z_β	557 μm	2240 μm
Gaussian waist r_G	5.5 μm	11 μm
Fresnel number N	6.48	6.48

Table 5.2 – xf-irOCT design parameters

Fig. 5.1, despite the small increase in the central lobe size at shallow regions in the actual system. The resolution of the 5× configuration is underestimated in this mathematical description. These divergences might be due to differences in the metrics used of both measurements (i.e. although in our observations the first zero position fits well with the full-width at half maximum measurements) and to experimental artefacts not accounted for in these simple calculations (i.e. imperfections of the axicon and aberrations). Moreover, the mode-field diameter w_{MFD} has a significant impact of the axial length of the Bessel, the Fresnel Number and the detection's lateral resolution and is difficult to estimate in practice. The value here was taken from the website of Thorlabs.

5.2.2 Simulations

In addition to the theoretical description provided above, a simulation using the Fast-Focal Fields framework of Leutenegger et al. [194] was conducted to assess the performance of the system, using the same parameters as listed in Table 5.1. The results of the simulation for both 10× and 5× objectives are displayed in Fig. 5.5, showing in panels (a) and (c) the intensity profile in dB of the Gaussian detection, the Bessel illumination and the overall system for the 10× and 5× configurations respectively. Panels (b) and (d) display the PSF in linear scale at different depths for both magnifications. Interestingly, although the resolutions are in the similar range than in the theoretical calculation and the practical implementation, they are consistently smaller in the simulation. For the 10× configuration, the lateral resolution is around 2.5 μm in the simulation, whereas it was measured around 3 μm experimentally. The discrepancy is more pronounced in the 5× case, where a difference of >1 μm is observed. Overall, similarly to the theoretical calculation, these inconsistencies can be explained by imperfections in the

optical components, such as the axicon's tip and the collimation of the beam throughout the microscope. Nevertheless, simulating the PSF of the system provides a good estimate on the performance of the system.
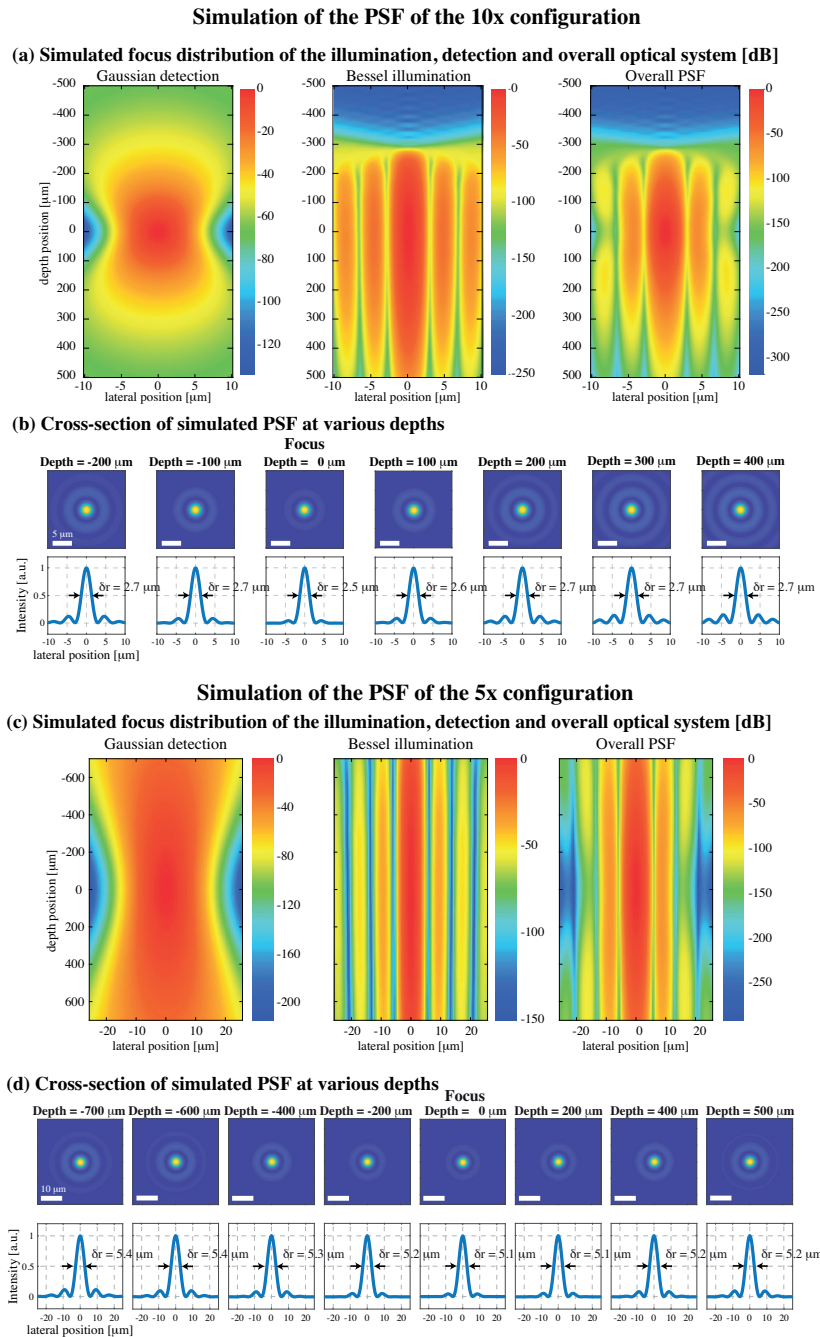

Figure 5.5 – Simulation results for the PSF of the 10× and 5× configurations, displaying the depth distribution of the PSF in dB for the detection, the illumination and the overall system (a) and (c). Cross-sections of the PSF are shown in tiles (b) and (d) highlighting the preservation of a central lobe of 2.5 μm throughout 600 μm.

6 Image gallery

A<small>N UNARGUABLE ADVANTAGE</small> of doing a PhD thesis in microscopy is the satisfaction of acquiring breath-taking images. However, as only the best ones end up in publications, some get discarded and end up collecting digital dust in hard-drives. This chapter will therefore present four of the nicest images obtained that were unfortunately never published.
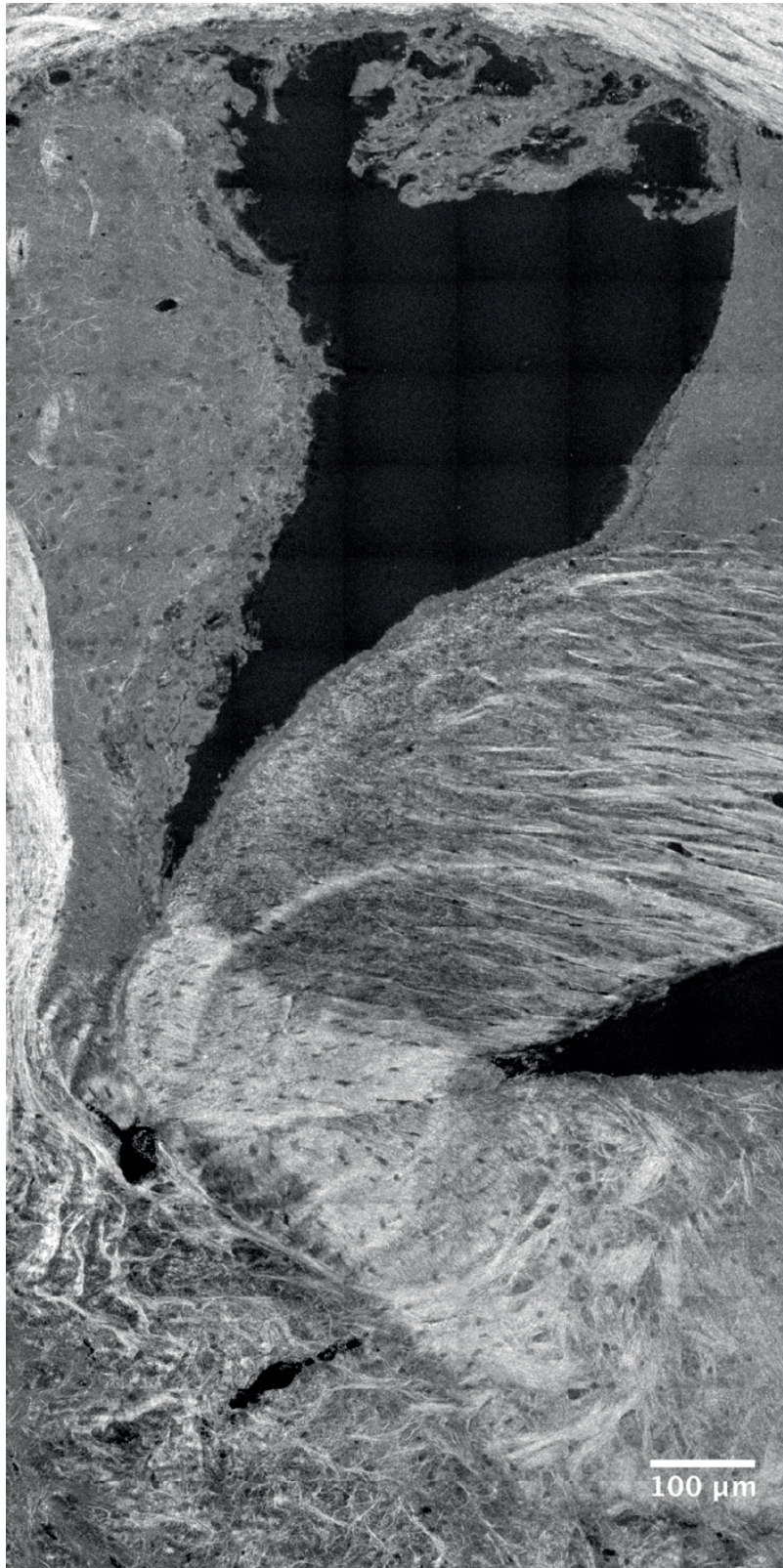
Figure 6.1 – A subcortical region of a mouse brain slice imaged using the visOCM system. Fiber bundles can be viewed as white fasciles and bright lines whereas neurons appear as darker structures

The scale bar reads 150 μm.
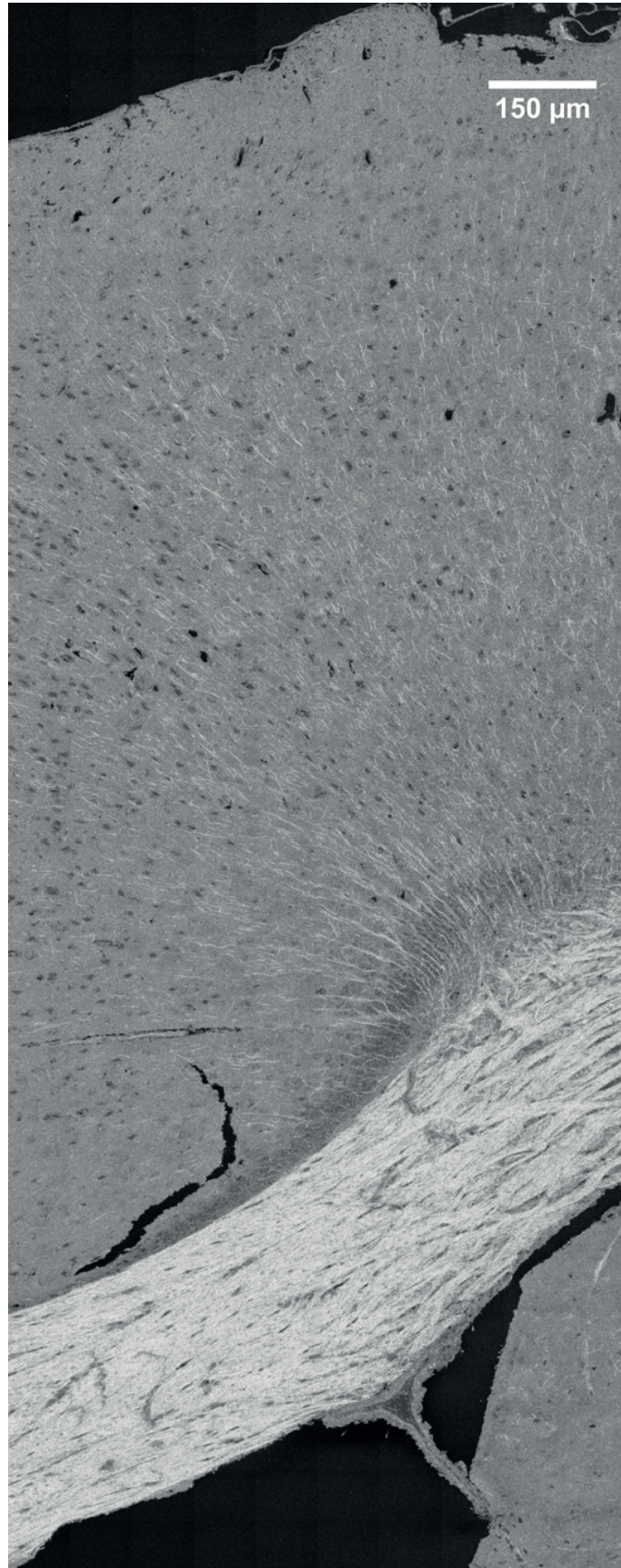
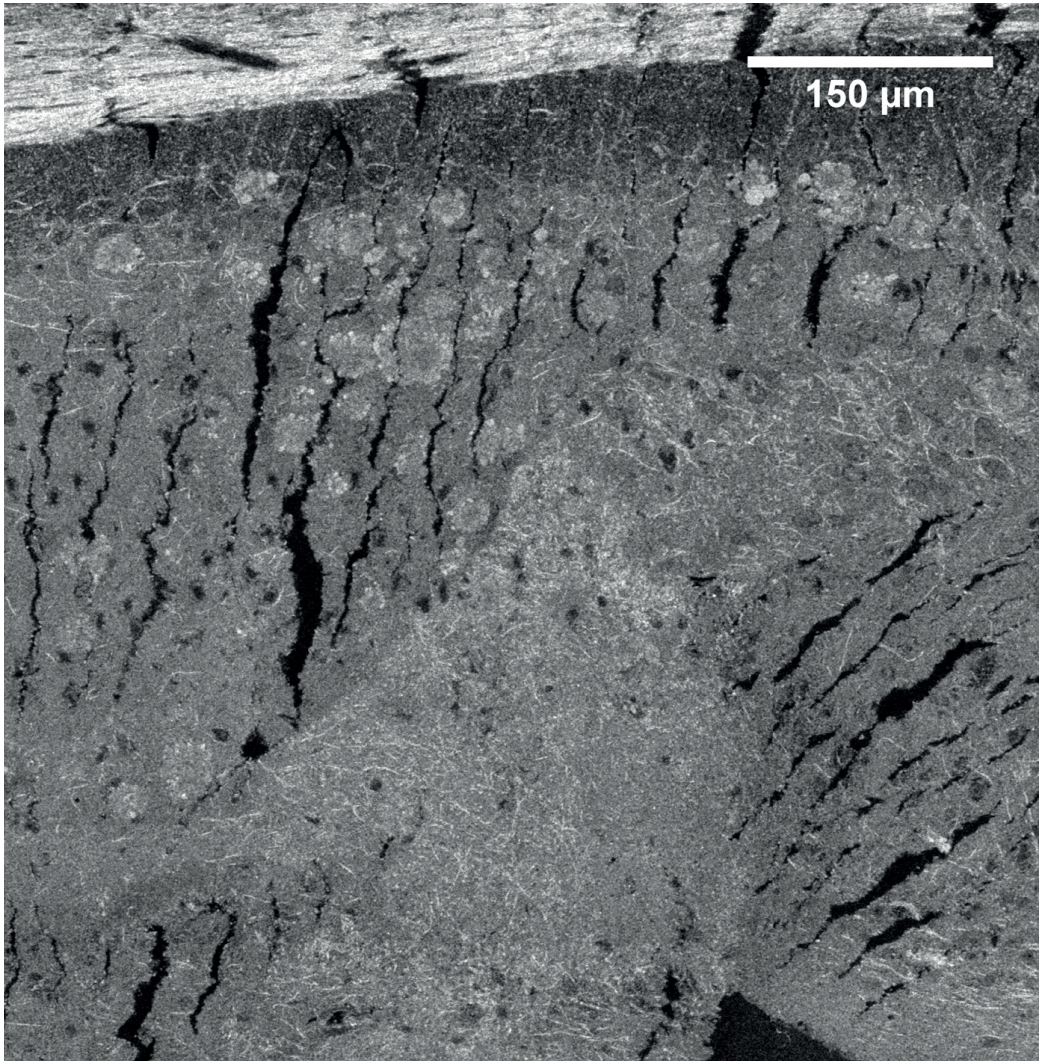**Figure 6.2 –** A cortical region of a mouse brain slice imaged using the visOCM system.

Figure 6.3 – A subcortical region of an alzheimeric mouse brain slice imaged using the visOCM system, where amyloid plaques can be discerned from the neuropil as brighter circular structures.
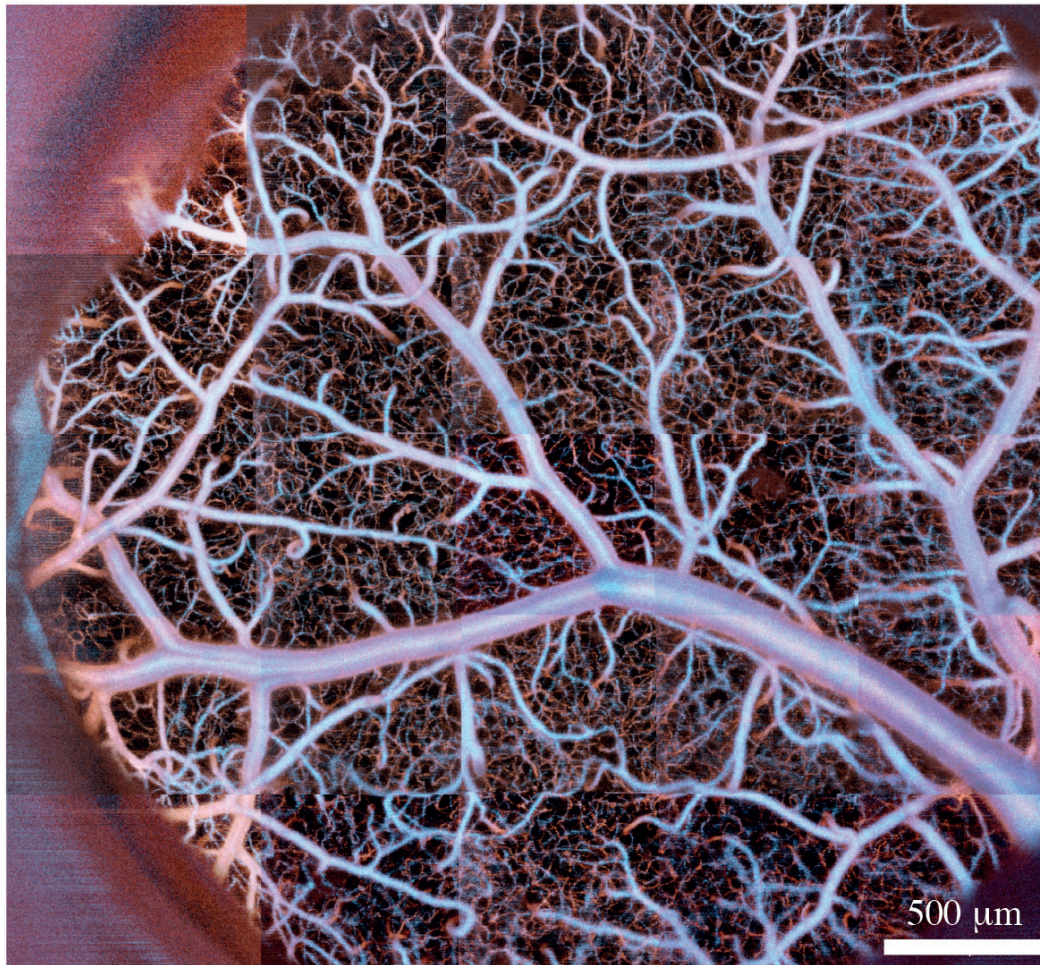
Figure 6.4 – An angiogram over the somatosensory cortex of a mouse obtained using the xf-OCM system at 800 nm.

Conclusion and perspectives

THE MAIN GOAL of the research presented in this thesis was to demonstrate the suitability of xf-OCT and xf-OCM imaging in studying the structure and function of the brain. In view of this goal, three microscopes were designed and constructed operating at illuminations spanning from the visible to the infrared spectral range for specific applications in brain imaging, from high-resolution imaging of subcellular structures in brain slices to imaging of entire microvascular networks deep in the cerebral cortex. Moreover, in an effort to bridge the gap existing between powerful statistical tools routinely used in fMRI and high-resolution functional brain imaging techniques, we adapted the SPM framework to quantitative blood flow measurements obtained using xf-OCM. This optimized SPM pipeline includes processing steps for quantitative blood estimation and uses angiographic imaging to segment vascular compartments and extract velocity time traces. Ultimately, compartment-resolved statistical parametric maps were obtained, reflecting the intrinsic heterogeneity of blood flow responses to stimulation. As mentioned in the journal article [90], this framework could be used in future studies to analyse hemodynamics alterations caused by neurovascular diseases [149]. Ultimately, the xf-OCM system used for this study was limited in penetration depth due to its relatively short illumination wavelength. As such, performing a similar study using the novel xf-irOCT system would enable generating statistical parametric maps over the entire cortical depth and could further highlight specific differences of the hemodynamic response across cortical layers (typically by using regressors reflecting changes in the temporal spread and lag of the responses). The implementation of total blood flow velocity used in chapter 2 showed some limitations in dynamic range and sensitivity to slow flow (especially in capillaries). In view of this, the algorithm could be adapted using a similar strategy than developed by Tang et al. [123], through a finer temporal oversampling and a filtering step to remove any bias caused by static tissue. Considerations regarding the effect of the filter on the final flow estimation should be thoroughly examined, especially in cases where the velocity vector is almost perpendicular to the optical axis, wherein the static and dynamic components would spectrally overlap, potentially biasing the estimation. The oversampling could greatly enhance the sensitivity to capillary flows by alleviating the effect of discrete flow on the Doppler spectrum [121]. Moreover, although the oversampling would strongly reduce the temporal resolution of the technique, it would permit performing simultaneous angiographic imaging, and thus would potentially enable measuring several hemodynamic parameters concurrently, i.e. RBC concentration [101], linear density (by measuring the peaks in the intensity time traces [118]) and RBC velocity. Ultimately, a similar study as performed by Srinivasan et al. [126] could be performed using this novel paradigm, shedding light on the laminar organisation of evoked blood responses in a quantitative manner [12]. Additionally, the results should

be compared to measurements obtained with other optical imaging modalities and metrics, such as LSCI and OIS, in an overarching effort to bridge microscopic and macroscopic techniques. More specifically, analysing changes in the shape of the hemodynamic response function using different vascular metrics (i.e. velocity, hematocrit, oxygenation, etc. . .) at different scales might provide novel insights into the role of specific vascular compartments in the overall macroscopic recorded signal.

Two implementations of high-resolution visible OCM were presented for *ex-vivo* imaging of fine cerebral structures and living cells and for *in-vivo* imaging of the superficial layers of the cortex respectively. The visOCM system, designed for *ex-vivo* tissue and live-cell imaging, possesses a submicron axial and lateral resolution, maintained over approximatively 40 μm in depth and has enabled imaging fine structures within cortical regions, such as myelinated axons, amyloid plaques, different types of neuronal cells, capillaries and even subcellular structures (i.e. nucleus of certain cells). Although more fundamental research is necessary to understand the underlying mechanisms responsible for the contrast observed in our images [169, 195], the unarguable imaging performance of the system makes it an attractive tool for structural brain imaging at high resolutions. The extended-focus configuration of the high-resolution visible OCM system enabled increasing the DOF by a factor >10 in comparison to traditional OCM implementations, enabling imaging of relatively thick slices of tissue without the need for axial scanning of the probing beam. Nevertheless, although the use of Bessel beams provided a high lateral resolution throughout an extended DOF, deviations from the pure Bessel PSF shape were observed at the extremities of the axial support, which we attribute mainly to unfiltered imperfections arising from the tip of the axicon.

An interesting application of the system would be for serial OCT imaging [139], as it would provide subcellular imaging of cerebral structures with an increased contrast with respect to current systems operating at 1.3 μm. An intrinsic drawback of visible OCT is its limited penetration depth, which would result in the need for a fine serial sectioning, leading to potential tissue deformation. Coupling the system with a multiphoton source would alleviate this issue by offering the possibility of slicing through ablation [134], as well as the opportunity for colinear 2PEF imaging. Alternatively, clearing agents could be used to increase the penetration depth [85, 87] and potentially generate new types of contrasts [196], at the cost of losing the chemical integrity of the tissue. The visOCM's capabilities for live-cell imaging also show great promise for studying cellular mechanisms in a label-free fashion and at very fast acquisition rates and has been subsequently used to perform three-dimensional imaging of living C. Elegans [197]. Moreover, as shown in chapter 3, using an OCT angiography protocol provided an additional contrast mechanism, based on the motion of subcellular structures [164], which could ultimately be used to assess functional parameters, such as cell viability [171].

The current implementation of the visOCM system would greatly benefit from a longer line-camera, to alleviate the broadening of the axial PSF observed for larger depths and enable a finer spectral sampling for spectroscopic imaging [87]. Additionally, using recently available supercontinuum sources enhanced in the UV would permit further increasing the axial sectioning capabilities by shifting the spectrum towards shorter central wavelengths, provided the impact of UV light on living samples is carefully taken into consideration, especially when imaging cell cultures and micro-organisms such as C. Elegans. Ultimately, applying spectroscopic OCT processing tools on samples imaged with the visOCM would provide interesting opportunities for molecular imaging at high spatio-temporal resolutions.

The second OCM system in the visible presented here, termed xf-visOCM, was designed for high-resolution *in-vivo* imaging of the first layers of the cortex, wherein the resolution was slightly decreased

with respect to the visOCM configuration, enabling imaging over a larger field-of-view (FOV) at a longer depth-of-focus. Similarly to its high-resolution counterpart, the xf-visOCM system could resolve cerebral structures such as myelinated fibres, cerebral capillaries and even neuronal cell bodies without the need for exogenous contrast agents. Interestingly, the high resolution afforded by the system was sufficient to distinguish capillaries as dark structures in the structural tomograms (without the need for OCT angiographic protocols). To our knowledge, the xf-visOCM system provides the highest axial resolution imaging of neuronal cells *in-vivo*. Ultimately, the instrument could be used to study demyelination associated to neurodegenerative disorders (such as multiple sclerosis) [182] and capillary oxygenation [52], by performing spectroscopic imaging [162]. Furthermore, the high resolution of the system could increase the accuracy of total blood flow measurements and offer a higher sensitivity for low flows, as decreasing the size of the focal volume would emphasize the Doppler broadening cause by moving particles [148]. Moreover, as capillaries can be identified already as dark structures in the back-scattering images, the contribution of static tissue to the flow estimation would be significantly reduced compared to low-resolution techniques, and would decrease the bias observed by Tang et al. [123].

Interestingly, both visible xf-OCM implementations showed a discrepancy between the simulated and the experimental PSFs, reflected primarily as a broadening of the central lobe of the Bessel function. Although this additional deviation of the PSF can be attributed once again to imperfection in the axicon tip, another likely explanation involves the role of the large bandwidth source and the wavelength-dependant angle of the axicon lens. Indeed, axicon's are in fact an UVFS prism, and as such, variations in the refractive index of glass results in a change in the refractive angle of the conical lens, thus changing the central lobe width of the Bessel. For such large bandwidths, this might explain the underestimation of the PSF obtained from simulation, wherein this effect was not modelled. Furthermore, this chromatic refraction from the axicon might result in a *wash-out* effect, reducing the amplitude of the Bessel sidelobes (as different wavelengths would result in different sidelobe diameters). Simulating these effects should be the focus of future work, in an effort to understand the origins of these discrepancies and offer potential novel ways of increasing the performance of extended-focus schemes. The effect of this chromatic refraction should also be considered in the context of compensating the overall dispersion of the system, and attain a perfectly dispersion-compensated system.

Finally, the last instrument designed and constructed during this thesis is the xf-irOCT system, which is an extension of the xf-OCM system at 800 nm devised specifically for deep cortical hemodynamic imaging. The central wavelength was shifted to the infrared wavelength range to reduce the effect of light scattering and enable reaching depths up to 1.5 mm in tissue. As mentioned in chapter 5, combining an extended-focus configuration with a broadband SLD required minimizing power losses within the instrument and managing the efficiency of the Bessel illumination. To our knowledge, it is the first time that such considerations, formalized by Lorenser et al. [193], were taken into account in designing an xf-OCT system. The Fresnel number of the ir-xfOCT system was calculated as ~ 7, whereas previous extended-focus configurations (including the visOCM system) reached a N>20. Overall, the ir-xfOCT instrument provides two magnifications characterized by a resolution of ~3 μm and ~6.5 μm maintained over ~900 μm and 1.5 mm in air respectively. These performances were assessed in an *in-vivo* setting by performing back-scattering and angiographic imaging of cortical structures in anaesthetized mice. The microvascular network could be imaged throughout almost the entire depth of the cortex using both objectives, although the axial extent available with the high-resolution implementation (10× objective) was slightly reduced to ~500 μm in depth. This reduction in depth-of-field in

the angiograms is mainly attributed to the smaller axial extent of the 10× configuration (relative to the 5× configuration) and the stronger impact of defocus at the edges of the depth-of-field. Although both magnifications provide similar information, the 10× would be more suited for quantitative studies, wherein a high lateral resolution is required. As mentioned earlier, the accuracy of total blood flow measurements and other quantitative hemodynamic metrics (e.g. RBC velocity metric devised by Lee et al. [118]) depend strongly on the lateral resolution, therefore the 10× would be more suited for such measurements. Conversely, the 5× objective trades a slightly worse lateral resolution for a larger DOF and field-of-view (FOV) and would therefore be ideal for studies requiring a high temporal resolution.

From a technological standpoint, the xf-irOCT system would greatly benefit from novel strategies currently developed in 2PEF for ultrawide FOV and multi-region synchronous imaging, two features which could further enhance its capabilities for functional brain imaging. Wide FOV imaging has recently gained interest within the 2PEF community as it allows imaging over approximately ten squared millimetres while maintaining a high lateral resolution, thus enabling the tracking of the spread of phenomenons occurring at the cellular level over entire cortical regions. In this context, Tsai et al. designed an ultra-large FOV two-photon microscope using off-the-shelf optics [198], able to image over areas of 10 mm × 8 mm while maintaining a micron-scale resolution. Similarly, Sofroniew et al. devised a so-called two-photon mesoscope (also called two-photon random access mesoscope, 2p-RAM) combining correction optics for large FOV imaging, galvanometric scanners and a remote-focusing unit for fast three-dimensional imaging over large areas [56]. Reaching such performances in 2PEF is challenging as decreasing the lateral resolution in 2PEF (i.e. broadening of the lateral PSF) increases the axial extent of the focal volume and thus decreases the fluorescence excitation efficiency and the axial resolution, resulting in the need for higher powers and lower attainable penetration depths. Conversely, OCT does not suffer from this limitation as its optical sectioning capabilities are obtained through the coherent gating of the source and are thus uncoupled from the microscope's lateral resolution. As such, OCT can reach large FOV simply by decreasing the objective NA. Nevertheless, as mentioned earlier, a high lateral resolution is required to obtain accurate functional information, such as good estimates of total velocity and fine-detailed angiograms. Combining high resolution OCT with an ultra-large field-of-view would thus enable fully exploiting the large selection of tools available with OCT. Overall, the xf-OCM configuration can already be viewed as a first step towards ultra-wide FOV OCT, as it enables maintaining a high lateral resolution over a large depth-of-field. Implementing similar correction optics as in Tsai et al. and Sofroniew et al. on an xf-OCM system is thus a logical step towards novel OCT systems dedicated to brain imaging. Such a system would then allow tracking changes in total blood flow and hematocrit (through OCT angiography) over large areas and over hubs of resting-state functional networks [16]. In addition to *in-vivo* functional imaging, a high resolution wide FOV OCM system would be of great interest for *ex-vivo* brain mapping efforts, as it would enable high-resolution imaging of intrinsic back-scattering over large areas. Moreover, potentially entire mouse brain sections could be imaged without displacing the sample and stitching mosaics, thus increasing the imaging speed and alleviating the post-processing load. Furthermore, recent efforts in digital adaptive optics (DAO) with OCT present a tantalizing opportunity to enable such increases in FOV without the need for intricate correction optics, wavefront sensors nor SLMs [199, 200, 201]. Although effects as vignetting would require changes in the optical design, aberrations at the edges of the FOV could be corrected using such strategies. As both angiographic and blood flow measurements typically require oversampling [95, 109], few modifications of the acquisition protocol would be necessary to perform such aberrations corrections. Overall, OCT technology is unarguably

compatible with such technological improvements.

The second main avenue for functional brain imaging with 2PEF is simultaneous imaging of spatially remote brain areas, both in depth and laterally. Although several systems have been implemented to simultaneously monitor the activity of different depths with 2PEF, through the use of temporal focusing and electrically tunable lenses, few studies have focused on monitoring over separate lateral areas. An interesting solution was presented by Stirman et al., wherein the pulses of a femtosecond source were split and delayed using a polarizing beam-splitter and two distinct optical paths [202]. Both arms are then guided to individual steering units (galvo-scanners) before being injected into the 2PEF microscope. As such, two field of views can be monitored simultaneously, through temporal multiplexing (the overall repetition frequency of the pulses is doubled, but each second pulse excites a different spatial location). Through correction optics, the attainable field of view spans over 9.5 mm^2 and can image over distinct areas of the visual cortex, distant by a few millimetres. An alternative strategy for such simultaneous imaging of multiple planes was presented by Yang et al. using an SLM to produce beamlets imaging distinct spatial regions and exploiting advanced computational tools to reconstruct the signal from both areas [203]. This simultaneous imaging capability would be particularly interesting for studies in functional connectivity networks, as it would allow tracking hemodynamic and neuronal changes simultaneously over large areas.

Such a system was implemented in OCT by Song et al. using a swept-source system at 1300 nm. Swept-sources are particularly interesting as they typically exhibit very low roll-off, can image over several millimetres (up to 20 mm) and thus are ideal for axial multiplexing, i.e. multiplexing over depth. The system designed by Song et al. is based on a conventional OCT system, where a second arm is added, impinging on the galvo-scanners at the same position as the original beam, but with a configurable angle [204]. As the scan-unit is placed in a plane conjugate to the image plane, this angle then translates into a displacement at the sample. Moreover, the length of the second beam path is set to be slightly longer than the original path (by a few millimeters). As both beams interfere with the same reference arm, they will be imaged one after the other in the tomogram, and thus will be axially separated. Song et al.'s system can therefore perform simultaneous imaging of remote areas by exploiting the low roll-off of the source. Additionally, their system was designed to enable varying the focal position of various lenses, resulting in a change of the axial focal position of both beams independently. Amongst many potential applications, augmenting the current xf-irOCT system with such a configuration would enable tracking the hemodynamic response of distinct cortical areas simultaneously, and would allow shedding light on the specificity of functional hyperaemia and on its temporal propagation, particularly in the case of electrical stimulation in mice, wherein a lack of specificity is observed and attributed to a cardiovascular systemic response. Alternatively, in view of imaging deeper into tissue, a novel xf-irOCT system could be designed operating a longer wavelengths, similarly to the work of Chong et al. and Kawagoe et al. to image subcortical areas [88, 186], at the cost of a potential loss in lateral resolution for a given NA.

Overall, the xf-irOCT system devised here would provide an ideal tool to study cortical hemodynamics and could shed light on processes involved in blood flow regulation at the capillary level, over the entire cortical depth. Moreover, as hinted at in chapter 1, the xf-irOCT could be used to underpin the origins of hemodynamic events observed in fMRI. A recent study by Schroeter et al. reported the presence of unspecific evoked hemodynamic responses to electrical stimulation of paws in mice [205]. These widespread changes, attributed to arousal-related cardiovascular responses, spread over both hemispheres and overruled the contribution of contra-lateral functional hyperaemia. Although this

study concluded that a neuronal contribution to these phenomenons is negligible using acallosal mice models (mice models wherein the communication between both cerebral hemispheres is weak or non-existent), questions relating to the involvement of different vascular compartments to the measured signal remain to be answered. Combining the stimulation paradigm employed by Schroeter et al., the SPM framework devised here and imaging with the xf-irOCT would allow studying the dynamics of these arousal-related responses at the capillary level, and could provide a microvascular view of these phenomenons. Moreover, the unspecific vascular change caused by this arousal-related response could provide an opportunity to study capillary regulation devoid of neuronal activation. Recent studies have raised the question of the existence of an active flow regulation system operating at the capillary level, through various cells of the neurovascular unit (e.g. pericytes) [130, 131, 206]. Nevertheless, the laminar organisation of capillary hemodynamics observed by Yu et al. [12] and Srinivasan et al. [126] could also reflect the natural geometry of the vascular tree and could therefore be entirely passive [207]. As such, comparing the laminar characteristics of the arousal-response in various brain regions could shed light on the existence or non-existence of this microvascular regulation system.

Acknowledgements

During the past four years spent at LOB, doing research and writing, I have had the chance to work with a lot of interesting people and make new friendships. None of the work presented in this thesis would have possible without their help and without the support of my friends and family.

I would first like to thank Prof. Theo Lasser, without whom none of the work presented in this thesis would have been possible. Theo's mentorship started even before my PhD Thesis, when I was still a neophyte in the field of microscopy, and continued throughout the entirety of my thesis. Through our shared passion for early-morning coffee and science, I learned a lot about microscopy, philosophy, history and even a bit of carpentry! I am truly grateful for his support, his guidance and his everlasting optimism, which I will remember forever. I would also like to thank my thesis co-director Prof. Markus Rudin of ETH Zürich for our discussions and his precious insight into fMRI technology and brain physiology. Finally, I would like to express my gratitude to Prof. Stéphanie Lacour, who kindly greeted me in her laboratory for the last three months of my thesis.

I would also like to thank Prof. Rainer Leitgeb, Prof. Thomas Huser, Prof. Dimitri Van de Ville and Prof. Hans Peter Hertzig for kindly accepting to be part of my thesis committee. I really appreciated the discussions and their comments regarding the work presented in this thesis.

A special thank you goes to Dr. Arno Bouwens, who supervised me during my master thesis at LOB and then helped me throughout this PhD Thesis. I sincerely appreciated our numerous discussions on OCM, microscopy, Japanese food and other non-scientific subjects (e.g. frog rains). I would also like to thank Arno for the time he spent helping me plan experiments and for proof-reading my manuscripts.

I would also like to thank Dr. Severine Coquoz and David Nguyen with whom I shared the office throughout most of the past 4 years. Thank you Severine for your light-hearted and not so light-hearted stories and for the funny moments we shared in the office. A special thanks goes to David for understanding my sometimes strange sense of humour and for sharing my interest for old-school video games and internet memes. Overall, thank you Severine and David for your support, patience and for the laughs we shared in BM 5139.

Thank you also to the rest of what Corinne called LOB's *crazy* generation, Dr. Miguel Sison and Dr. Azat Sharipov, who introduced me to Filipino and Russian culture respectively, who shared my struggles in the lab and who made me laugh on numerous occasions.

Bibliography

[1] N. K. Logothetis, M. Auguth, A. Oeltermann, J. Pauls, and T. Trinath. A neurophysiological investigation of the basis of the BOLD signal in fMRI. *Nature*, 412(6843):150–157, 2001.

[2] S. Ogawa, T.-M. Lee, A. S. Nayak, and P. Glynn. Oxygenation-sensitive contrast in magnetic resonance image of rodent brain at high magnetic fields. *Magn. Reson. Med*, 14(1):68–78, 1990.

[3] R. L. Buckner. Event-related fMRI and the hemodynamic response. *Hum. Brain Mapp.*, 6(5-6):373–377, 1998.

[4] M. Fox and D. Zhang. The global signal and observed anticorrelated resting state brain networks. *J. Neurophysiol.*, 101(6):3270–3283, 2009.

[5] N. U. F. Dosenbach, B. Nardos, A. L. Cohen, D. a. Fair, J. D. Power, J. a. Church, S. M. Nelson, G. S. Wig, A. C. Vogel, C. N. Lessov-Schlaggar, K. A. Barnes, J. W. Dubis, E. Feczko, R. S. Coalson, J. R. Pruett, D. M. Barch, S. E. Petersen, and B. L. Schlaggar. Prediction of individual brain maturity using fMRI. *Science*, 329(5997):1358–61, sep 2010.

[6] N. Leonardi, J. Richiardi, M. Gschwind, S. Simioni, J.-M. Annoni, M. Schluep, P. Vuilleumier, and D. Van De Ville. Principal components of functional connectivity: A new approach to study dynamic brain connectivity during rest. *NeuroImage*, 83:937–950, 2013.

[7] A. W. Bero, A. Q. Bauer, F. R. Stewart, B. R. White, J. R. Cirrito, M. E. Raichle, J. P. Culver, and D. M. Holtzman. Bidirectional relationship between functional connectivity and amyloid-β deposition in mouse brain. *J. Neurosci.*, 32(13):4334–40, mar 2012.

[8] Y. I. Sheline, M. E. Raichle, A. Z. Snyder, J. C. Morris, D. Head, S. Wang, and M. A. Mintun. Amyloid Plaques Disrupt Resting State Default Mode Network Connectivity in Cognitively Normal Elderly. *Biol. Psychiatry*, 67(6):584–587, 2010.

[9] K. Uludag and P. Blinder. Linking brain vascular physiology to hemodynamic response in ultra-high field MRI. *NeuroImage*, (February), 2016.

[10] X. Yu, D. Glen, S. Wang, S. Dodd, Y. Hirano, Z. Saad, R. Reynolds, A. C. Silva, and A. P. Koretsky. Direct imaging of macrovascular and microvascular contributions to BOLD fMRI in layers IV-V of the rat whisker-barrel cortex. *NeuroImage*, 59(2):1451–1460, 2012.

[11] X. Yu, Y. He, M. Wang, H. Merkle, S. J. Dodd, A. C. Silva, and A. P. Koretsky. Sensory and optoge-netically driven single-vessel fMRI. *Nat. Methods*, 13(4):337–340, 2016.

Bibliography

[12] X. Yu, C. Qian, D.-y. Chen, S. J. Dodd, and A. P. Koretsky. Deciphering laminar-specific neural inputs with line-scanning fMRI. *Nat. Methods*, 11(1):55–8, 2014.

[13] X. Hu and E. Yacoub. The story of the initial dip in fMRI. *NeuroImage*, 62(2):1103–1108, 2012.

[14] P. C. M. van Zijl, J. Hua, and H. Lu. The BOLD post-stimulus undershoot, one of the most debated issues in fMRI. *NeuroImage*, 62(2):1092–1102, 2012.

[15] A. T. Winder, C. Echagarruga, Q. Zhang, and P. J. Drew. Weak correlations between hemodynamic signals and ongoing neural activity during the resting state. *Nat. Neurosci*, 20(12):1761–1769, 2017.

[16] C. Mateo, P. M. Knutsen, P. S. Tsai, A. Y. Shih, and D. Kleinfeld. Entrainment of Arteriole Vasomotor Fluctuations by Neural Activity Is a Basis of Blood-Oxygenation-Level-Dependent "Resting-State" Connectivity. *Neuron*, 96(4):936–948.e3, 2017.

[17] J. R. Bumstead, A. Q. Bauer, P. W. Wright, and J. P. Culver. Cerebral functional connectivity and Mayer waves in mice: Phenomena and separability. *J. Cereb. Blood Flow Metab.*, 37(2):471–484, 2016.

[18] L. Gagnon, S. Sakadžić, F. Lesage, J. J. Musacchia, J. Lefebvre, Q. Fang, M. A. Yucel, K. C. Evans, E. T. Mandeville, J. Cohen-Adad, J. R. Polimeni, M. A. Yaseen, E. H. Lo, D. N. Greve, R. B. Buxton, A. M. Dale, A. Devor, and D. A. Boas. Quantifying the Microvascular Origin of BOLD-fMRI from First Principles with Two-Photon Microscopy and an Oxygen-Sensitive Nanoprobe. *J. Neurosci.*, 35(8):3663–3675, 2015.

[19] A. Urban, L. Golgher, C. Brunner, A. Gdalyahu, H. Har-Gil, D. Kain, G. Montaldo, L. Sironi, and P. Blinder. Understanding the neurovascular unit at multiple scales: Advantages and limitations of multi-photon and functional ultrasound imaging. *Adv. Drug Deliv. Rev.*, 119:73–100, 2017.

[20] D. H. Evans, J. A. Jensen, and M. B. Nielsen. Ultrasonic colour Doppler imaging. *Interface Focus*, 1(4):490–502, 2011.

[21] E. Mace E., G. Montaldo, I. Cohen, M. Baulac, M. Fink, and M. Tanter. Functional ultrasound imaging of the brain. *Nat. Methods*, 8(8):662–664, 2011.

[22] C. Errico, B. F. Osmanski, S. Pezet, O. Couture, Z. Lenkei, and M. Tanter. Transcranial functional ultrasound imaging of the brain using microbubble-enhanced ultrasensitive Doppler. *NeuroImage*, 124:752–761, 2016.

[23] A. Urban, E. Mace, C. Brunner, M. Heidmann, J. Rossier, and G. Montaldo. Chronic assessment of cerebral hemodynamics during rat forepaw electrical stimulation using functional ultrasound imaging. *NeuroImage*, 101:138–149, jul 2014.

[24] B.-F. Osmanski, S. Pezet, A. Ricobaraza, Z. Lenkei, and M. Tanter. Functional Ultrasound Imaging of Intrinsic Connectivity in the Living Rat Brain with High Spatiotemporal Resolution. *Nat. Commun.*, 5(5023), 2014.

[25] C. Errico, J. Pierre, S. Pezet, Y. Desailly, Z. Lenkei, O. Couture, and M. Tanter. Ultrafast ultrasound localization microscopy for deep super-resolution vascular imaging. *Nature*, 527(7579):499–502, 2015.

[26] J. Yao and L. V. Wang. Photoacoustic brain imaging: from microscopic to macroscopic scales. *Neurophotonics*, 1(1):011003, 2014.

[27] S. Hu and L. V. Wang. Neurovascular photoacoustic tomography. *Frontiers in Neuroenergetics*, 2(June):1–7, 2010.

[28] S. Hu, K. Maslov, and L. V. Wang. Noninvasive label-free imaging of microhemodynamics by optical-resolution photoacoustic microscopy. *Opt. Express*, 17(9):7688–93, 2009.

[29] M. Nasiriavanaki, J. Xia, H. Wan, A. Q. Bauer, J. P. Culver, and L. V. Wang. High-resolution photoacoustic tomography of resting-state functional connectivity in the mouse brain. *Proc. Natl. Acad. Sci. USA PNAS*, 111(1):21–6, jan 2014.

[30] S. Hu, P. Yan, K. Maslov, J.-M. Lee, and L. V. Wang. Intravital imaging of amyloid plaques in a transgenic mouse model using optical-resolution photoacoustic microscopy. *Opt. Lett.*, 34(24):3899–3901, 2009.

[31] L. Ma, G. Rajshekhar, R. Wang, B. Bhaduri, S. Sridharan, M. Mir, A. Chakraborty, R. Iyer, S. Prasanth, L. Millet, M. U. Gillette, and G. Popescu. Phase correlation imaging of unlabeled cell dynamics. *Sci. Rep.*, 6(March):32702, 2016.

[32] F. F. Jobsis. Noninvasive, infrared monitoring of cerebral and myocardial oxygen sufficiency and circulatory parameters. *Science*, 198(4323):1264–1267, 1977.

[33] M. B. Bouchard, B. R. Chen, S. A. Burgess, and E. M. C. Hillman. Ultra-fast multispectral optical imaging of cortical oxygenation, blood flow, and intracellular calcium dynamics. *Opt. Express*, 17(18):15670–78, 2009.

[34] D. A. Boas and A. K. Dunn. Laser speckle contrast imaging in biomedical optics. *J. Biomed. Opt.*, 15(1):011109, 2014.

[35] A. Serov and T. Lasser. High-speed laser Doppler perfusion imaging using an integrating CMOS image sensor. *Opt. Express*, 13(17):6416–28, 2005.

[36] A. Raabe, D. Vandeville, M. Leutenegger, A. Szelenyi, E. Hattingen, R. Gerlach, V. Seifert, C. Hauger, A. Lopez, R. Leitgeb, D. Van De Ville, M. Leutenegger, A. Szel\'{e}nyi, E. Hattingen, R. Gerlach, V. Seifert, C. Hauger, A. Lopez, R. Leitgeb, M. Unser, E. J. Martin-Williams, and T. Lasser. Laser Doppler imaging for intraoperative human brain mapping. *NeuroImage*, 44(4):1284–1289, 2009.

[37] S. M. S. Kazmi, A. B. Parthasarthy, N. E. Song, T. A. Jones, and A. K. Dunn. Chronic imaging of cortical blood flow using Multi-Exposure Speckle Imaging. *J. Cereb. Blood Flow Metab.*, 33(6):798–808, 2013.

[38] H. Slovin. Long-Term Voltage-Sensitive Dye Imaging Reveals Cortical Dynamics in Behaving Monkeys. *J. Neurophysiol.*, 88(6):3421–3438, 2002.

[39] J. Akerboom, T.-W. Chen, T. J. Wardill, L. Tian, J. S. Marvin, S. Mutlu, N. C. Calderón, F. Esposti, B. G. Borghuis, X. R. Sun, A. Gordus, M. B. Orger, R. Portugues, F. Engert, J. J. Macklin, A. Filosa, A. Aggarwal, R. a. Kerr, R. Takagi, S. Kracun, E. Shigetomi, B. S. Khakh, H. Baier, L. Lagnado, S. S.-H. Wang, C. I. Bargmann, B. E. Kimmel, V. Jayaraman, K. Svoboda, D. S. Kim, E. R. Schreiter, and L. L.

Looger. Optimization of a GCaMP calcium indicator for neural activity imaging. *J. Neurosci.*, 32(40):13819–40, oct 2012.

[40] C. Stosiek, O. Garaschuk, K. Holthoff, and A. Konnerth. In vivo two-photon calcium imaging of neuronal networks. *Proc. Natl. Acad. Sci. U.S.A.*, 100(12):7319–24, jun 2003.

[41] C. Du, N. D. Volkow, A. P. Koretsky, and Y. Pan. Low-frequency calcium oscillations accompany deoxyhemoglobin oscillations in rat somatosensory cortex. *Proc. Natl. Acad. Sci. USA PNAS*, 111(43):E4677–4686, oct 2014.

[42] A. Rayshubskiy, T. J. Wojtasiewicz, C. B. Mikell, M. B. Bouchard, D. Timerman, B. E. Youngerman, R. a. McGovern, M. L. Otten, P. Canoll, G. M. McKhann, and E. M. C. Hillman. Direct, intraoperative observation of ~0.1Hz hemodynamic oscillations in awake human cortex: Implications for fMRI. *NeuroImage*, 87:323–331, 2014.

[43] B. R. White, A. Q. Bauer, A. Z. Snyder, B. L. Schlaggar, J.-M. Lee, and J. P. Culver. Imaging of functional connectivity in the mouse brain. *PLoS ONE*, 6(1):e16322, jan 2011.

[44] A. Q. Bauer, A. W. Kraft, P. W. Wright, A. Z. Snyder, J.-M. Lee, and J. P. Culver. Optical imaging of disrupted functional connectivity following ischemic stroke in mice. *NeuroImage*, 99C:388–401, may 2014.

[45] E. Guevara, N. Sadekova, H. Girouard, and F. Lesage. Optical imaging of resting-state functional connectivity in a novel arterial stiffness model. *Biomed. Opt. Express*, 4(11):2332–46, jan 2013.

[46] S. W. Paddock. Principles and practices of laser scanning confocal microscopy. *Mol. Biotechnol.*, 16(2):127–149, oct 2000.

[47] J. Mertz. Optical sectioning microscopy with planar or structured illumination. *Nat. Methods*, 8(10):811–9, jan 2011.

[48] R. Heintzmann and T. Huser. Super-Resolution Structured Illumination Microscopy. *Chemical Reviews*, page acs.chemrev.7b00218, 2017.

[49] F. Helmchen and W. Denk. Deep tissue two-photon microscopy. *Nat. Methods*, 2(12):932–940, 2005.

[50] W. Denk, J. H. Strickler, and W. W. Webb. Two-photon laser scanning fluorescence microscopy. *Science*, 248(4951):73–6, 1990.

[51] K. Svoboda and R. Yasuda. Principles of two-photon excitation microscopy and its applications to neuroscience. *Neuron*, 50(6):823–39, jun 2006.

[52] S. Sakadžić, E. Roussakis, M. a. Yaseen, E. T. Mandeville, V. J. Srinivasan, K. Arai, S. Ruvinskaya, A. Devor, E. H. Lo, S. a. Vinogradov, and D. a. Boas. Two-photon high-resolution measurement of partial pressure of oxygen in cerebral vasculature and tissue. *Nat. Methods*, 7(9):755–759, 2010.

[53] J. Lecoq, A. Parpaleix, E. Roussakis, M. Ducros, Y. Goulam Houssen, S. A. Vinogradov, and S. Charpak. Simultaneous two-photon imaging of oxygen and blood flow in deep cerebral vessels. *Nat. Med.*, 17(7):893–8, jul 2011.

[54] J. K. Hefendehl, D. Milford, D. Eicke, B. M. Wegenast-Braun, M. E. Calhoun, S. A. Grathwohl, M. Jucker, and C. Liebig. Repeatable target localization for long-term in vivo imaging of mice with 2-photon microscopy. *J. Neurosci. methods*, 205(2):357–63, apr 2012.

[55] A. Y. Shih, J. D. Driscoll, P. J. Drew, N. Nishimura, C. B. Schaffer, and D. Kleinfeld. Two-photon microscopy as a tool to study blood flow and neurovascular coupling in the rodent brain. *J. Cereb. Blood Flow Metab.*, 32(7):1277–309, jul 2012.

[56] N. J. Sofroniew, D. Flickinger, J. King, and K. Svoboda. A large field of view two-photon mesoscope with subcellular resolution for in vivo imaging. *eLife*, 5(JUN2016):1–20, 2016.

[57] P. Rupprecht, A. Prendergast, C. Wyart, and R. W. Friedrich. Remote z-scanning with a macroscopic voice coil motor for fast 3D multiphoton laser scanning microscopy. *Biomed. Opt. Express*, 7(5):1656, 2016.

[58] E. Papagiakoumou, V. de Sars, V. Emiliani, and D. Oron. Temporal focusing with spatially modulated excitation. *Opt. Express*, 17(7):5391–401, mar 2009.

[59] A. Cheng, J. T. Gonçalves, P. Golshani, K. Arisaka, and C. Portera-Cailliau. Simultaneous two-photon calcium imaging at different depths with spatiotemporal multiplexing. *Nat. Methods*, 8(2):139–42, mar 2011.

[60] D. Kobat, N. G. Horton, and C. Xu. In vivo two-photon microscopy to 1.6-mm depth in mouse cortex. *J. Biomed. Opt.*, 16(10):106014, oct 2011.

[61] A. F. Fercher, W. Drexler, C. K. Hitzenberger, and T. Lasser. Optical coherence tomography - development, principles, applications. *Rep. Prog. Phys.*, 66:239–303, 2003.

[62] D. Huang, E. A. Swanson, C. P. Lin, J. S. Schuman, W. G. Stinson, W. Chang, M. R. Hee, T. Flotte, K. Gregory, C. A. Puliafito, and J. G. Fujimoto. Optical coherence tomography. *Science*, 254(5035):1178–1181, 1991.

[63] B. J. Vakoc, R. M. Lanning, J. A. Tyrrell, T. P. Padera, L. A. Bartlett, T. Stylianopoulos, L. L. Munn, G. J. Tearney, D. Fukumura, R. K. Jain, and B. E. Bouma. Three-dimensional microscopy of the tumor microenvironment in vivo using optical frequency domain imaging. *Nat. Med.*, 15(10):1219–23, oct 2009.

[64] U. Baran, Y. Li, R. K. Wang, U. T. K. U. B. Aran, and Y. L. I. Uandong. In vivo tissue injury mapping using optical coherence tomography based methods. *Appl. Opt.*, 54(21):6448–6453, 2015.

[65] C. Berclaz, J. Goulley, M. Villiger, C. Pache, A. Bouwens, E. Martin-Williams, D. Van de Ville, A. C. Davison, A. Grapin-Botton, and T. Lasser. Diabetes imaging-quantitative assessment of islets of Langerhans distribution in murine pancreas using extended-focus optical coherence microscopy. *Biomed. Opt. Express*, 3(6):1365–80, jun 2012.

[66] V. J. Srinivasan, D. N. Atochin, H. Radhakrishnan, J. Y. Jiang, S. Ruvinskaya, W. Wu, S. Barry, A. E. Cable, C. Ayata, P. L. Huang, and D. A. Boas. Optical coherence tomography for the quantitative study of cerebrovascular physiology. *J. Cereb. Blood Flow Metab.*, 31(6):1339–45, jun 2011.

Bibliography

[67] A. D. Aguirre, C. Zhou, H.-C. Lee, O. O. Ahsen, and J. G. Fujimoto. Optical Coherence Microscopy, pages 865–911. Springer International Publishing, Cham, 2015. ISBN 978-3-319-06419-2.

[68] R. A. Leitgeb, T. Lasser, and M. Villiger. OCM with Engineered Wavefront, pages 913–940. Springer International Publishing, Cham, 2015. ISBN 978-3-319-06419-2.

[69] R. Arimoto, C. Saloma, T. Tanaka, and S. Kawata. Imaging properties of axicon in a scanning optical system. *Appl. Opt*, 31(31):6653–7, nov 1992.

[70] Y. Chen and J. T. Liu. Characterizing the beam steering and distortion of Gaussian and Bessel beams focused in tissues with microscopic heterogeneities. *Biomed. Opt. Express.*, 6(4):1318, mar 2015.

[71] A. Curatolo, M. Villiger, D. Lorenser, P. Wijesinghe, A. Fritz, B. F. Kennedy, and D. D. Sampson. Ultrahigh-resolution optical coherence elastography. *Opt. Lett.*, 41(1):21–24, 2016.

[72] Z. Ding, H. Ren, Y. Zhao, J. S. Nelson, and Z. Chen. High-resolution optical coherence tomography over a large depth range with an axicon lens. *Opt. Lett.*, 27(4):243, 2002.

[73] R. A. Leitgeb, M. Villiger, A. H. Bachmann, L. Steinmann, and T. Lasser. Extended focus depth for Fourier domain optical coherence microscopy. *Opt. Lett.*, 31(16):2450, 2006.

[74] C. Berclaz, A. Schmidt-Christensen, D. Szlag, J. Extermann, L. Hansen, A. Bouwens, M. Villiger, J. Goulley, F. Schuit, A. Grapin-Botton, T. Lasser, and D. Holmberg. Longitudinal three-dimensional visualisation of autoimmune diabetes by functional optical coherence imaging. *Diabetologia*, 59(3):550–559, 2016.

[75] T. Bolmont, A. Bouwens, C. Pache, M. Dimitrov, C. Berclaz, M. Villiger, B. M. Wegenast-Braun, T. Lasser, and P. C. Fraering. Label-free imaging of cerebral β-amyloidosis with extended-focus optical coherence microscopy. *J. Neurosci.*, 32(42):14548–56, oct 2012.

[76] M. Sison, S. Chakrabortty, J. Extermann, A. Nahas, P. J. Marchand, A. Lopez, T. Weil, and T. Lasser. 3D Time-lapse Imaging and Quantification of Mitochondrial Dynamics. *Sci. Rep.*, 7(January):1–8, 2017.

[77] M. Villiger, C. Pache, and T. Lasser. Dark-field optical coherence microscopy. *Opt. Lett.*, 35(20):3489–3491, 2010.

[78] C. Blatter, B. Grajciar, C. M. Eigenwillig, W. Wieser, B. R. Biedermann, R. Huber, and R. A. Leitgeb. Extended focus high-speed swept source OCT with self-reconstructive illumination. *Opt. Express*, 19(13):12141–55, jun 2011.

[79] M. Villiger and T. Lasser. Image formation and tomogram reconstruction in optical coherence microscopy. *J. Opt. Soc. Am.*, 27(10):2216–2228, 2010.

[80] J. A. Izatt, M. A. Choma, and A.-H. Dhalla. Theory of Optical Coherence Tomography, pages 65–94. Springer International Publishing, Cham, 2015. ISBN 978-3-319-06419-2.

[81] O. Assayag, K. Grieve, B. Devaux, F. Harms, J. Pallud, F. Chretien, C. Boccara, and P. Varlet. Imaging of non-tumorous and tumorous human brain tissues with full-field optical coherence tomography. *Neuroimage Clin.*, 2(1):549–557, 2013.

[82] S. Tamborski, H. C. Lyu, H. Dolezyczek, M. Malinowska, G. Wilczynski, D. Szlag, T. Lasser, M. Wojtkowski, and M. Szkulmowski. Extended-focus optical coherence microscopy for high-resolution imaging of the murine brain. *Biomed. Opt. Express*, 7(11):4400–14, 2016.

[83] V. J. Srinivasan, H. Radhakrishnan, J. Y. Jiang, S. Barry, and A. E. Cable. Optical coherence microscopy for deep tissue imaging of the cerebral cortex with intrinsic contrast. *Opt. Express*, 20(3):2220–39, jan 2012.

[84] V. J. Srinivasan, H. Radhakrishnan, E. H. Lo, E. T. Mandeville, J. Y. Jiang, S. Barry, and A. E. Cable. OCT methods for capillary velocimetry. *Biomed. Opt. Express.*, 3(3):612–29, mar 2012.

[85] C. Leahy, H. Radhakrishnan, and V. J. Srinivasan. Volumetric imaging and quantification of cytoarchitecture and myeloarchitecture with intrinsic scattering contrast. *Biomed. Opt. Express*, 4(10):1978–90, jan 2013.

[86] C. Magnain, J. C. Augustinack, E. Konukoglu, M. P. Frosch, S. Sakadžić, A. Varjabedian, N. Garcia, V. J. Wedeen, D. a. Boas, and B. Fischl. Optical coherence tomography visualizes neurons in human entorhinal cortex. *Neurophotonics*, 2(1):015004, 2015.

[87] A. Lichtenegger, D. J. Harper, M. Agustin, P. Eugui, M. Muck, J. Gesperger, C. K. Hitzenberger, A. Woehrer, and B. Baumann. Spectroscopic imaging with spectral domain visible light optical coherence microscopy in Alzheimer ' s disease brain samples. *Biomed. Opt. Express*, 8(9):4007–25, 2017.

[88] S. P. Chong, C. W. Merkle, D. F. Cooke, T. Zhang, H. Radhakrishnan, L. Krubitzer, and V. J. Srinivasan. Noninvasive, in vivo imaging of subcortical mouse brain regions with 1.7 μm optical coherence tomography. *Opt. Lett.*, 40(21):4911, 2015.

[89] S. Chen, Q. Liu, X. Shu, B. Soetikno, S. Tong, and H. F. Zhang. Imaging hemodynamic response after ischemic stroke in mouse cortex using visible-light optical coherence tomography. *Biomed. Opt. Express*, 7(9):3377, 2016.

[90] P. J. Marchand, A. Bouwens, T. Bolmont, V. K. Shamaei, D. Nguyen, D. Szlag, J. Extermann, and T. Lasser. Statistical parametric mapping of stimuli evoked changes in total blood flow velocity in the mouse cortex obtained with extended-focus optical coherence microscopy. *Biomed. Opt. Express.*, 8(1):1, 2017.

[91] R. A. Leitgeb, R. M. Werkmeister, C. Blatter, and L. Schmetterer. Doppler Optical Coherence Tomography. *Progress in Retinal and Eye Research*, 41(1):26–43, 2014.

[92] A. G. Borovoi, E. I. Naats, and U. G. Oppel. Scattering of light by a red blood cell. *J. Biomed. Opt.*, 3:3–9, 1998.

[93] J. Zhu, C. Merkle, M. Bernucci, S. Chong, and V. Srinivasan. Can OCT Angiography Be Made a Quantitative Blood Measurement Tool? *Applied Sciences*, 7(7):687, 2017.

[94] V. J. Srinivasan, S. Sakadžić, I. Gorczynska, S. Ruvinskaya, W. Wu, J. G. Fujimoto, and D. a. Boas. Quantitative cerebral blood flow with optical coherence tomography. *Opt. Express*, 18(3):2477–94, feb 2010.

[95] V. J. Srinivasan, J. Y. Jiang, M. A. Yaseen, H. Radhakrishnan, W. Wu, S. Barry, A. E. Cable, and D. A. Boas. Rapid volumetric angiography of cortical microvasculature with optical coherence tomography. *Opt. Lett.*, 35(1):43–5, jan 2010.

[96] W. Wei, J. Xu, U. Baran, S. Song, W. Qin, X. Qi, and R. K. Wang. Intervolume analysis to achieve four-dimensional optical microangiography for observation of dynamic blood flow. *J. Biomed. Opt.*, 21(3):036005, 2016.

[97] M. S. Mahmud, D. W. Cadotte, B. Vuong, C. Sun, T. W. H. Luk, A. Mariampillai, and V. X. D. Yang. Review of speckle and phase variance optical coherence tomography to visualize microvascular networks. *J. Biomed. Opt*, 18(5):50901, may 2013.

[98] D. Y. Kim, J. Fingler, J. S. Werner, D. M. Schwartz, S. E. Fraser, and R. J. Zawadzki. In vivo volumetric imaging of human retinal circulation with phase-variance optical coherence tomography. *Biomed. Opt. Express.*, 2(6):1504–13, jun 2011.

[99] J. Fingler, D. Schwartz, C. Yang, and S. E. Fraser. Mobility and transverse flow visualization using phase variance contrast with spectral domain optical coherence tomography. *Opt. Express*, 15(20):12636–53, 2007.

[100] R. K. Wang and L. An. Doppler optical micro-angiography for volumetric imaging of vascular perfusion in vivo. *Opt. Express*, 17(11):8926–40, may 2009.

[101] W. J. Choi, W. Qin, C.-L. Chen, J. Wang, Q. Zhang, X. Yang, B. Z. Gao, and R. K. Wang. Characterizing relationship between optical microangiography signals and capillary flow using microfluidic channels. *Biomed. Opt. Express*, 7(7):2709, 2016.

[102] J. Enfield, E. Jonathan, and M. Leahy. In vivo imaging of the microcirculation of the volar forearm using correlation mapping optical coherence tomography (cmOCT). *Biomed. Opt. Express*, 2(5):1184–1193, 2011.

[103] A. S. Nam, I. Chico-Calero, and B. J. Vakoc. Complex differential variance algorithm for optical coherence tomography angiography. *Biomed. Opt. Express.*, 5(11):3822–3832, nov 2014.

[104] J. Tokayer, Y. Jia, A.-H. Dhalla, and D. Huang. Blood flow velocity quantification using split-spectrum amplitude-decorrelation angiography with optical coherence tomography. *Biomed. Opt. Express.*, 4(10):1909–24, 2013.

[105] L. Yu and Z. Chen. Doppler variance imaging for three-dimensional retina and choroid angiography. *J. Biomed. Opt.*, 15(1):016029, 2010.

[106] V. J. Srinivasan, E. Yu, H. Radhakrishnan, A. Can, M. Climov, C. Leahy, C. Ayata, and K. Eikermann-Haerter. Micro-heterogeneity of flow in a mouse model of chronic cerebral hypoperfusion revealed by longitudinal Doppler optical coherence tomography and angiography. *J. Cereb. Blood Flow Metab.*, (April):1–9, 2015.

[107] J. You, C. Du, N. D. Volkow, and Y. Pan. Optical coherence Doppler tomography for quantitative cerebral blood flow imaging. *Biomed. Opt. Express*, 5(9):3217–30, aug 2014.

[108] M. Szkulmowski, A. Szkulmowska, T. Bajraszewski, A. Kowalczyk, and M. Wojtkowski. Flow velocity estimation using joint spectral and time-domain optical coherence tomography. *Opt. Express*, 16(9):6008–6025, 2008.

[109] A. Bouwens, T. Bolmont, D. Szlag, C. Berclaz, and T. Lasser. Quantitative cerebral blood flow imaging with extended-focus optical coherence microscopy. *Opt. Lett.*, 39(1):37–40, jan 2014.

[110] F. Schmid, M. J. Barrett, P. Jenny, and B. Weber. Vascular density and distribution in neocortex. *NeuroImage*, 2017.

[111] J. You, A. Li, C. Du, and Y. Pan. Volumetric Doppler angle correction for ultrahigh-resolution optical coherence Doppler tomography. *Appl. Phys. Lett.*, 110(1), 2017.

[112] R. Haindl, W. Trasischker, A. Wartak, B. Baumann, M. Pircher, and C. K. Hitzenberger. Total retinal blood flow measurement by three beam Doppler optical coherence tomography. *Biomed. Opt. Express*, 7(2):287–301, 2016.

[113] R. Michaely, A. H. Bachmann, M. L. Villiger, C. Blatter, T. Lasser, and R. A. Leitgeb. Vectorial reconstruction of retinal blood flow in three dimensions measured with high resolution resonant Doppler Fourier domain optical coherence tomography. *J. Biomed. Opt.*, 12(4):041213, 2007.

[114] H. Ren, K. M. Brecke, Z. Ding, Y. Zhao, J. S. Nelson, and Z. Chen. Imaging and quantifying transverse flow velocity with the Doppler bandwidth in a phase-resolved functional optical coherence tomography. *Opt. Lett.*, 27(6):409–11, mar 2002.

[115] D. Piao, L. L. Otis, and Q. Zhu. Doppler angle and flow velocity mapping by combined Doppler shift and Doppler bandwidth measurements in optical Doppler tomography. *Opt. Lett.*, 28(13):1120–2, jul 2003.

[116] J. Lee, W. Wu, J. Y. Jiang, B. Zhu, and D. a. Boas. Dynamic light scattering optical coherence tomography. *Opt. Express*, 20(20):22262–77, sep 2012.

[117] J. Lee, H. Radhakrishnan, W. Wu, A. Daneshmand, M. Climov, C. Ayata, and D. a. Boas. Quantitative imaging of cerebral blood flow velocity and intracellular motility using dynamic light scattering-optical coherence tomography. *J. Cereb. Blood Flow Metab.*, 33(6):819–25, jun 2013.

[118] J. Lee, W. Wu, F. Lesage, and D. A. Boas. Multiple-capillary measurement of RBC speed, flux, and density with optical coherence tomography. *J. Cereb. Blood Flow Metab.*, 33(11):1707–10, nov 2013.

[119] B. Li, H. Wang, B. Fu, R. Wang, S. Sakadžić, and D. A. Boas. Impact of temporal resolution on estimating capillary RBC-flux with optical coherence tomography. *J. Biomed. Opt.*, 22(1):016014, 2017.

[120] H. Ren, C. Du, K. Park, N. D. Volkow, and Y. Pan. Quantitative imaging of red blood cell velocity invivo using optical coherence Doppler tomography. *Appl. Phys. Lett.*, 100(23):4–8, 2012.

[121] Y. Pan, J. You, N. D. Volkow, K. Park, and C. Du. Ultrasensitive detection of 3D cerebral microvascular network dynamics in vivo. *NeuroImage*, 103:492–501, sep 2014.

[122] C. W. Merkle, C. Leahy, and V. J. Srinivasan. Dynamic contrast optical coherence tomography images transit time and quantifies microvascular plasma volume and flow in the retina and choriocapillaris. *Biomed. Opt. Express.*, 7(10):752–755, 2016.

[123] J. Tang, S. E. Erdener, B. Fu, and D. A. Boas. Capillary red blood cell velocimetry by phase-resolved optical coherence tomography. *Opt. Lett.*, 42(19):3976, 2017.

[124] H. Radhakrishnan and V. J. Srinivasan. Compartment-resolved imaging of cortical functional hyperemia with OCT angiography. *Biomed. Opt. Express.*, 4(8):1255, jul 2013.

[125] V. J. Srinivasan, S. Sakadžić, I. Gorczynska, S. Ruvinskaya, W. Wu, J. G. Fujimoto, and D. a. Boas. Depth-resolved microscopy of cortical hemodynamics with optical coherence tomography. *Opt. Lett.*, 34(20):3086–8, oct 2009.

[126] V. J. Srinivasan and H. Radhakrishnan. Optical Coherence Tomography angiography reveals laminar microvascular hemodynamics in the rat somatosensory cortex during activation. *NeuroImage*, 102 Pt 2:393–406, nov 2014.

[127] J. Lee, J. Y. Jiang, W. Wu, F. Lesage, and D. A. Boas. Statistical intensity variation analysis for rapid volumetric imaging of capillary network flux. *Biomed. Opt. Express.*, 5(4):1160, mar 2014.

[128] J. Lee, W. Wu, and D. A. Boas. Early capillary flux homogenization in response to neural activation. *J. Cereb. Blood Flow Metab.*, 0(0):1–6, 2015.

[129] P. M. Rasmussen, S. N. Jespersen, and L. Ostergaard. The effects of transit time heterogeneity on brain oxygenation during rest and functional activation. *J. Cereb. Blood Flow Metab.*, (October):1–11, dec 2014.

[130] M. D. Sweeney, S. Ayyadurai, and B. V. Zlokovic. Pericytes of the neurovascular unit: key functions and signaling pathways. *Nat. Neurosci.*, 19(6):771–783, 2016.

[131] C. N. Hall, C. Reynell, B. Gesslein, N. B. Hamilton, A. Mishra, B. A. Sutherland, F. M. O'Farrell, A. M. Buchan, M. Lauritzen, and D. Attwell. Capillary pericytes regulate cerebral blood flow in health and disease. *Nature*, 508(7494):55–60, 2014.

[132] K. Kisler, A. R. Nelson, A. Montagne, and B. V. Zlokovic. Cerebral blood flow regulation and neurovascular dysfunction in Alzheimer disease. *Nat. Rev. Neurosci.*, 18(7):419–434, 2017.

[133] A. Li, H. Gong, B. Zhang, Q. Wang, C. Yan, J. Wu, L. Qian, S. Zeng, and Q. Luo. Micro-Optical Sectioning Tomography. *Science*, 1404(2010):1404–1408, 2010.

[134] P. S. Tsai, B. Friedman, A. I. Ifarraguerri, B. D. Thompson, V. Lev-Ram, C. B. Schaffer, Q. Xiong, R. Y. Tsien, J. A. Squier, and D. Kleinfeld. All-optical histology using ultrashort laser pulses. *Neuron*, 39(1):27–41, 2003.

[135] K. Chung and K. Deisseroth. CLARITY for mapping the nervous system. *Nat. Methods*, 10(6):508–13, jun 2013.

[136] C. Magnain, J. C. Augustinack, M. Reuter, C. Wachinger, M. P. Frosch, T. Ragan, T. Akkin, V. J. Wedeen, D. A. Boas, and B. Fischl. Blockface histology with optical coherence tomography: A comparison with Nissl staining. *NeuroImage*, 84:524–533, 2014.

[137] H. Wang, C. Lenglet, and T. Akkin. Structure tensor analysis of serial optical coherence scanner images for mapping fiber orientations and tractography in the brain. *J. Biomed. Opt.*, 20(3):036003, 2015.

[138] E. Min, J. Lee, A. Vavilin, S. Jung, S. Shin, J. Kim, and W. Jung. Wide-field optical coherence microscopy of the mouse brain slice. *Opt. Lett.*, 40(19):4420–4423, 2015.

[139] J. Lefebvre, A. Castonguay, P. Pouliot, M. Descoteaux, and F. Lesage. Whole mouse brain imaging using optical coherence tomography: reconstruction, normalization, segmentation, and comparison with diffusion MRI. *Neurophotonics*, 4(4):041501, 2017.

[140] H. Wang, C. Magnain, S. Sakadžić, B. Fischl, D. A. Boas, E. C. C Cauberg, D. M. de Bruin, D. J. Faber, T. M. de Reijke, M. Visser, J. J. de la Rosette, T. G. van Leeuwen, C. Kut, K. L. Chaichana, J. Xi, S. M. Raza, X. Ye, E. R. McVeigh, F. J. Rodriguez, A. Quiñones-Hinojosa, and X. Li. Characterizing the optical properties of human brain tissue with high numerical aperture optical coherence tomography. *Biomed. Opt. Express*, 8(12):5617–5636, 2017.

[141] H. Wang, C. Magnain, R. Wang, J. Dubb, A. Varjabedian, L. S. Tirrell, A. Stevens, J. C. Augustinack, E. Konukoglu, I. Aganj, M. P. Frosch, J. D. Schmahmann, B. Fischl, and D. A. Boas. as-PSOCT: Volumetric microscopic imaging of human brain architecture and connectivity. *NeuroImage*, 165(October 2017):56–68, 2018.

[142] N. Hadjikhani, A. K. Liu, A. M. Dale, P. Cavanagh, and R. B. Tootell. Retinotopy and color sensitivity in human visual cortical area V8. *Nat. Neurosci.*, 1(3):235–41, 1998.

[143] J. Warnking, M. Dojat, A. Guérin-Dugué, C. Delon-Martin, S. Olympieff, N. Richard, A. Chéhikian, and C. Segebarth. fMRI retinotopic mapping - Step by step. *NeuroImage*, 17(4):1665–1683, 2002.

[144] C. M. Wessinger, M. H. Buonocore, C. L. Kussmaul, and G. R. Mangun. Tonotopy in human auditory cortex examined with functional magnetic resonance imaging. *Human Brain Mapping*, 5(1):18–25, 1997.

[145] S. Ogawa and T. Lee. Brain magnetic resonance imaging with contrast dependent on blood oxygenation. *Proc. Natl. Acad. Sci. U.S.A.*, 87(24):9868–72, 1990.

[146] K. Friston. Chapter 2 - Statistical parametric mapping. In K. Friston, J. Ashburner, S. Kiebel, T. Nichols, and W. Penny, editors, Statistical Parametric Mapping, pages 10–31. Academic Press, London, 2007. ISBN 978-0-12-372560-8.

[147] L. Lindvere, R. Janik, A. Dorr, D. Chartash, B. Sahota, J. G. Sled, and B. Stefanovic. Cerebral microvascular network geometry changes in response to functional stimulation. *NeuroImage*, 71:248–59, may 2013.

[148] A. Bouwens, D. Szlag, M. Szkulmowski, T. Bolmont, M. Wojtkowski, and T. Lasser. Quantitative lateral and axial flow imaging with optical coherence microscopy and tomography. *Opt. Express*, 21(15):17711–17729, 2013.

[149] C. Iadecola. Neurovascular regulation in the normal brain and in Alzheimer's disease. *Nat. Rev. Neurosci*, 5(5):347–360, 2004.

[150] D. Kleinfeld, P. P. Mitra, F. Helmchen, and W. Denk. Fluctuations and stimulus-induced changes in blood flow observed in individual capillaries in layers 2 through 4 of rat neocortex. *Proc. Natl. Acad. Sci. USA PNAS*, 95(26):15741–15746, 1998.

[151] F. Schlegel, A. Schroeter, and M. Rudin. The hemodynamic response to somatosensory stimulation in mice depends on the anesthetic used: Implications on analysis of mouse fMRI data. *NeuroImage*, 116:40–49, 2015.

[152] M. A. Franceschini, H. Radhakrishnan, K. Thakur, W. Wu, S. Ruvinskaya, S. Carp, and D. A. Boas. The effect of different anesthetics on neurovascular coupling. *NeuroImage*, 51(4):1367–77, jul 2010.

[153] O. Thouvenin, K. Grieve, P. Xiao, C. Apelian, and A. C. Boccara. En face coherence microscopy [Invited]. *Biomed. Opt. Express.*, 8(2):622, 2017.

[154] X. Shu, L. Beckmann, and H. F. Zhang. Visible-light optical coherence tomography: a review. *J. Biomed. Opt.*, 22(12):1, 2017.

[155] J. B. Pawley. Handbook of Biological Confocal Microscopy, Second Edition. *Optical Engineering*, 35(9):2765–2766, 1996.

[156] J. Huisken, J. Swoger, F. Del Bene, J. Wittbrodt, and E. H. K. Stelzer. Optical Sectioning Deep Inside Live Embryos by Selective Plane Illumination Microscopy. *Science*, 305(5686):1007–1009, 2004.

[157] T. Kim, R. Zhou, M. Mir, S. D. Babacan, P. S. Carney, L. L. Goddard, and G. Popescu. White-light diffraction tomography of unlabelled live cells. *Nat. Photonics*, 8(3):256–263, 2014.

[158] L. Tian and L. Waller. 3D intensity and phase imaging from light field measurements in an LED array microscope. *Optica*, 2(2):104–111, 2015.

[159] S. Broillet, D. Szlag, A. Bouwens, L. Maurizi, H. Hofmann, T. Lasser, and M. Leutenegger. Visible light optical coherence correlation spectroscopy. *Opt. Express*, 22(18):21944, 2014.

[160] F. E. Robles, C. Wilson, G. Grant, and A. Wax. Molecular imaging true-colour spectroscopic optical coherence tomography. *Nat. Photonics*, 5(12):744–747, 2011.

[161] J. Yi, Q. Wei, W. Liu, V. Backman, and H. F. Zhang. Visible-light optical coherence tomography for retinal oximetry. *Opt. Lett.*, 38(11):1796, 2013.

[162] S. P. Chong, C. W. Merkle, C. Leahy, H. Radhakrishnan, V. J. Srinivasan, C. W. Merkle, S. P. Chong, H. Radhakrishnan, and V. J. Srinivasan. Quantitative microvascular hemoglobin mapping using visible light spectroscopic Optical Coherence Tomography. *Biomed. Opt. Express*, 6(4):1422–1429, 2015.

[163] A. Oldenburg, X. Yu, T. Gilliss, O. Alabi, R. I. Taylor, and M. Torester. Inverse-power-law behavior of cellular motility reveals stromal - epithelial cell interactions in 3D co-culture by OCT fluctuation spectroscopy. *Optica*, 2(10):877–885, 2015.

[164] C. Apelian, F. Harms, O. Thouvenin, and A. C. Boccara. Dynamic full field optical coherence tomography: subcellular metabolic contrast revealed in tissues by interferometric signals temporal analysis. *Biomed. Opt. Express.*, 7(4):1511, 2016.

[165] M. Wojtkowski, V. J. Srinivasan, T. H. Ko, J. G. Fujimoto, A. Kowalczyk, and J. S. Duker. Ultrahigh-resolution, high-speed, Fourier domain optical coherence tomography and methods for dispersion compensation. *Opt. Express*, 12(11):707–709, 2004.

[166] N. Jährling, K. Becker, B. M. Wegenast-Braun, S. A. Grathwohl, M. Jucker, and H. U. Dodt. Cerebral β-amyloidosis in mice investigated by ultramicroscopy. *PLoS ONE*, 10(5):1–13, 2015.

[167] S. Jawhar, A. Trawicka, C. Jenneckens, T. A. Bayer, and O. Wirths. Motor deficits, neuron loss, and reduced anxiety coinciding with axonal degeneration and intraneuronal Abeta aggregation in the 5XFAD mouse model of Alzheimer's disease. *Neurobiol. Aging*, 33(1):196.e29–196.e40, 2012.

[168] R. Leitgeb, C. Hitzenberger, and A. Fercher. Performance of fourier domain vs time domain optical coherence tomography. *Opt. Express*, 11(8):889, 2003.

[169] G. Plascencia-Villa, A. Ponce, J. Collingwood, M. Josefina Arellano-Jiménez, X. Zhu, J. Rogers, I. Betancourt, M. José-Yacamán, and G. Perry. High-resolution analytical imaging and electron holography of magnetite particles in amyloid cores of Alzheimer's disease. *Sci. Rep.*, 6(April):1–12, 2016.

[170] B. Baumann, A. Woehrer, G. Ricken, M. Augustin, C. Mitter, M. Pircher, G. G. Kovacs, and C. K. Hitzenberger. Visualization of neuritic plaques in Alzheimer's disease by polarization-sensitive optical coherence microscopy. *Sci. Rep.*, 7(October 2016):43477, 2017.

[171] C.-E. Leroux, F. Bertillot, O. Thouvenin, and C. Boccara. Intracellular dynamics measurements with full field optical coherence tomography suggest hindering effect of actomyosin contractility on organelle transport. *Biomed. Opt. Express.*, 7(11):14057–14064, 2016.

[172] E. Auksorius, Y. Bromberg, M. Rå«ta, A. Pieretti, L. Liu, E. Coron, J. Aranda, A. M. Goldstein, B. E. Bouma, A. Kazlauskas, and G. J. Tearney. Dual-modality fluorescence and full-field optical coherence microscopy for biomedical imaging applications. *Biomed. Opt. Express.*, 3(3):661, 2012.

[173] H. Makhlouf, K. Perronet, G. Dupuis, S. Lévêque-Fort, and A. Dubois. Simultaneous optically sectioned fluorescence and optical coherence microscopy with full-field illumination. *Opt. Lett.*, 37(10):1613, 2012.

[174] U. Morgner, W. Drexler, F. X. Kärtner, X. D. L. Pitris C., E. P. Ippen, J. G. Fujimoto, X. D. Li, and C. Pitris. Spectroscopic optical coherence tomography. *Opt. Lett.*, 25(2):111, 2000.

[175] U. Baran, Y. Li, and R. K. Wang. Vasodynamics of pial and penetrating arterioles in relation to arteriolo-arteriolar anastomosis after focal stroke. *Neurophotonics*, 2(2):025006, 2015.

[176] S. P. Chong, M. Bernucci, H. Radhakrishnan, and V. J. Srinivasan. Structural and functional human retinal imaging with a fiber-based visible light OCT ophthalmoscope. *Biomed. Opt. Express*, 8(1):4083–4097, 2017.

[177] J. Yi, S. Chen, X. Shu, A. A. Fawzi, and H. F. Zhang. Human retinal imaging using visible-light optical coherence tomography guided by scanning laser ophthalmoscopy. *Biomed. Opt. Express*, 6(10):3701, 2015.

[178] C. W. Merkle, S. P. Chong, A. M. Kho, J. Zhu, A. Dubra, and V. J. Srinivasan. Visible light optical coherence microscopy of the brain with isotropic femtoliter resolution in vivo. *Opt. Lett.*, 43(2):198, 2018.

[179] J. A. Izatt, M. R. Hee, G. M. Owen, E. A. Swanson, and J. G. Fujimoto. Optical coherence microscopy in scattering media. *Opt. Lett.*, 19(8):590–592, 1994.

[180] J. Ben Arous, J. Binding, J.-F. Léger, M. Casado, P. Topilko, S. Gigan, A. C. Boccara, and L. Bourdieu. Single myelin fiber imaging in living rodents without labeling by deep optical coherence microscopy. *J. Biomed. Opt.*, 16(11):116012, 2011.

[181] C.-L. Chen and R. K. Wang. Optical coherence tomography based angiography [Invited]. *Biomed. Opt. Express*, 8(2):1056, 2017.

[182] A. J. Schain, R. A. Hill, and J. Grutzendler. Label-free in vivo imaging of myelinated axons in health and disease with spectral confocal reflectance microscopy. *Nat. Med.*, 20(4):443–9, apr 2014.

[183] L. A. Sordillo, Y. Pu, S. Pratavieira, Y. Budansky, and R. R. Alfano. Deep optical imaging of tissue using the second and third near-infrared spectral windows. *J. Biomed. Opt.*, 19(5):056004, 2014.

[184] L. Shi, L. A. Sordillo, A. Rodríguez-Contreras, and R. Alfano. Transmission in near-infrared optical windows for deep brain imaging. *J. Biophotonics*, 9(1-2):38–43, 2016.

[185] M. Yamanaka, T. Teranishi, H. Kawagoe, and N. Nishizawa. Optical coherence microscopy in 1700 nm spectral band for high-resolution label-free deep-tissue imaging. *Sci. Rep.*, 6(August):31715, 2016.

[186] H. Kawagoe, M. Yamanaka, S. Makita, Y. Yasuno, and N. Nishizawa. Full-range ultrahigh-resolution spectral-domain optical coherence tomography in 1.7 μm wavelength region for deep-penetration and high-resolution imaging of turbid tissues. *Appl. Phys. Express*, 9(12):7–11, 2016.

[187] A. Bachmann, R. Leitgeb, and T. Lasser. Heterodyne Fourier domain optical coherence tomography for full range probing with high axial resolution. *Opt. Express*, 14(4):1487–1496, 2006.

[188] W. J. Choi and R. K. Wang. Swept-source optical coherence tomography powered by a 1.3 μm vertical cavity surface emitting laser enables 2.3 mm deep brain imaging in mice in vivo imaging in mice in vivo. *J. Biomed. Opt.*, 20(10):106004, 2015.

[189] Y. Yoon, Q. Li, V. H. Le, W. H. Jang, T. Wang, B. Kim, S. Son, W. K. Chung, C. Joo, and K. H. Kim. Dark-field polarization-sensitive optical coherence tomography. *Opt. Express*, 23(10):12874, 2015.

[190] S. Kwon, Y. Yoon, B. Kim, W. H. Jang, B. Oh, K. Y. Chung, and K. H. Kim. Dermoscopy guided dark-field multi-functional optical coherence tomography. *Biomed. Opt. Express*, 8(3):1372, 2017.

[191] P. J. Marchand, A. Bouwens, D. Szlag, D. Nguyen, A. Descloux, M. Sison, S. Coquoz, J. Extermann, and T. Lasser. Visible spectrum extended-focus optical coherence microscopy for label-free sub-cellular tomography. *Biomed. Opt. Express*, 8(7):3343–3359, 2017.

[192] J. You, Q. Zhang, K. Park, C. Du, and Y. Pan. Quantitative imaging of microvascular blood flow networks in deep cortical layers by 1310 nm μODT. *Opt. Lett.*, 40(18):1–4, 2015.

[193] D. Lorenser, C. Christian Singe, A. Curatolo, and D. D. Sampson. Energy-efficient low-Fresnel-number Bessel beams and their application in optical coherence tomography. *Opt. Lett.*, 39(3):548, jan 2014.

[194] M. Leutenegger, R. Rao, R. A. Leitgeb, and T. Lasser. Fast focus field calculations. *Opt. Express*, 14(23):4897– 4903, 2006.

[195] P. Eugui, A. Lichtenegger, M. Augustin, D. J. Harper, M. Muck, T. Roetzer, A. Wartak, T. Konegger, G. Widhalm, C. K. Hitzenberger, and Others. Beyond backscattering: Optical neuroimaging by BRAD. *arXiv preprint arXiv:1712.00361*, 2017.

[196] J. Ren, H. Choi, K. Chung, and B. E. Bouma. Label-free volumetric optical imaging of intact murine brains. *Sci. Rep.*, 7:1–8, 2017.

[197] S. Coquoz, L. Mouchiroud, M. Sison, D. Szlag, P. Marchand, A. Bouwens, J. Auwerx, and T. Lasser. Label-free three-dimensional imaging of C . elegans with visible wavelength extended-focus optical coherence microscopy. *PLoS ONE*, 12(7):e0181676, 2017.

[198] P. S. Tsai, C. Mateo, J. J. Field, C. B. Schaffer, M. E. Anderson, and D. Kleinfeld. Ultra-large field-of-view two-photon microscopy. *Opt. Express*, 23(11):13833–47, 2015.

[199] S. Coquoz, A. Bouwens, P. J. Marchand, J. Extermann, and T. Lasser. Interferometric synthetic aperture microscopy for extended focus optical coherence microscopy. *Opt. Express*, 25(24):30807, 2017.

[200] L. Ginner, A. Kumar, D. Fechtig, L. M. Wurster, M. Salas, M. Pircher, and R. A. Leitgeb. Noniterative digital aberration correction for cellular resolution retinal optical coherence tomography in vivo. *Optica*, 4(8):924, 2017.

[201] A. Kumar, L. M. Wurster, M. Salas, L. Ginner, W. Drexler, and R. A. Leitgeb. In-vivo digital wavefront sensing using swept source OCT. *Biomed. Opt. Express*, 8(7):3369–3382, 2017.

[202] J. N. Stirman, I. T. Smith, M. W. Kudenov, and S. L. Smith. Wide field-of-view, multi-region, two-photon imaging of neuronal activity in the mammalian brain. *Nat. Biotechnol.*, 34(8):857–862, 2016.

[203] W. Yang, J. e. K. Miller, L. Carrillo-Reid, E. Pnevmatikakis, L. Paninski, R. Yuste, and D. S. Peterka. Simultaneous Multi-plane Imaging of Neural Circuits. *Neuron*, 89(2):284, 2016.

[204] S. Song, J. Xu, and R. K. Wang. Flexible wide-field optical micro-angiography based on Fourier-domain multiplexed dual-beam swept source optical coherence tomography. *J. Biophotonics*, (September):1–9, 2017.

[205] A. Schroeter, J. Grandjean, F. Schlegel, B. J. Saab, and M. Rudin. Contributions of structural connectivity and cerebrovascular parameters to functional magnetic resonance imaging signals in mice at rest and during sensory paw stimulation. *J. Cereb. Blood Flow Metab.*, 37(7):2368–2382, 2017.

[206] H. S. Wei, H. Kang, I. Y. D. Rasheed, S. Zhou, N. Lou, A. Gershteyn, E. D. McConnell, Y. Wang, K. E. Richardson, A. F. Palmer, C. Xu, J. Wan, and M. Nedergaard. Erythrocytes Are Oxygen-Sensing Regulators of the Cerebral Microcirculation. *Neuron*, 91(4):851–862, 2016.

[207] F. Fernández-Klett, N. Offenhauser, U. Dirnagl, J. Priller, and U. Lindauer. Pericytes in capillaries are contractile in vivo, but arterioles mediate functional hyperemia in the mouse brain. *Proc. Natl. Acad. Sci. U.S.A.*, 107(51):22290–22295, 2010.

Paul J. Marchand

Born May 10th 1988
Swiss / British / French citizen

Email : pjsmarchand@gmail.com / paul.marchand@epfl.ch
Mobile : 079 / 700 13 50
Av. de Cour 75, 1007 Lausanne, Switzerland

EDUCATION

EPFL, Laboratoire d'Optique Biomédicale — Lausanne, CH
PhD Thesis: Structural and functional Brain Imaging using extended-focus Optical Coherence Tomography and Microscopy. — *2013 – Current*
Design and construction of xfOCM/OCT systems in the visible and the infrared wavelength range. Application of statistical parametric mapping to Doppler OCT data to capture changes in hemodynamics during functional activation in mice.

Imperial College London — London, UK
MSc In Biomedical Engineering, Neurotechnology Stream, — *2012 – 2013*
(stream representative, Best Academic Performance Prize)
Master Thesis: In-vivo deep tissue multiphoton functional imaging (under the supervision of Prof. Schultz and Osh. Agabi)

EPFL, Laboratoire d'Optique Biomédicale — Lausanne, CH
Master Thesis: Design and Construction of an Optical Coherence Microscope in the visible wavelength range for uniform submicron resolution cellular imaging (under the supervision of Prof. Lasser and Dr. Bouwens) — *2012*

EPFL, INP Grenoble, Politecnico di Torino
MSc in Micro and Nano Integrated Systems (Nanotechnologies) — *2010 – 2012*
(Optoelectronics, Advanced Optics, Imaging Optics, Nanoelectronics)

EPFL — Lausanne, CH
BSc in Micro-Engineering — *2006 – 2010*

EXPERIENCE

EPFL, Internship at Laboratoire d'Optique Biomédicale — Lausanne, CH
Construction of a Spectrometer in the visible wavelength range. — *Summer 2012*

University of Sherbrooke — Sherbrooke, CA
Mechanical and optical characterisation of Single Electron Transistors. Use of AFM and cleanroom technology. — *Summer 2011*

EPFL — Lausanne, CH
Teaching Assistant: — *2007 – 2012*
Assistant to the course of *Elements of mechanical engineering design & CAD* for 1st year micro-engineering students.
Assistant to the course of Electronics and Electrotechnics for 1st year micro-engineering and 2nd year electrical engineering students.

LANGUAGES

English: *mothertongue*   French: *to native level*   German: *basic knowledge*   Italian: *basic knowledge*

Programming:	MATLAB, LabView, basics of C++ and C
Animal handling:	Surgical procedures (open-skull craniotomy), *in-vivo* imaging, animal care
CAD design:	Solidworks, ProE

Peer-reviewed publications

- S. Coquoz, A. Bouwens, **P. J. Marchand**, J. Extermann, and T. Lasser, "Interferometric synthetic aperture microscopy for extended focus optical coherence microscopy," Opt. Express 25, 30807-30819 (2017)

- D. Nguyen, **P. J. Marchand**, A. L. Planchette, J. Nilsson, M. Sison, J. Extermann, A. Lopez, M. Sylwestrzak, J. Sordet- Dessimoz, A. Schmidt-Christensen, D. Holmberg, D. Van De Ville, and T. Lasser, "Optical projection tomography for rapid whole mouse brain imaging," Biomed. Opt. Express 8, 5637-5650 (2017),

- S. Coquoz, **P.J. Marchand**, A. Bouwens, L. Mouchiroud, V. Sorrentino, D. Szlag, J. Auwerx, and T. Lasser, "Label-free three-dimensional imaging of Caenorhabditis elegans with visible optical coherence microscopy," PLoS One 12 (2017),

- **P. J. Marchand**, A. Bouwens, D. Szlag, D. Nguyen, A. Descloux, M. Sison, S. Coquoz, J. Extermann, and T. Lasser, "Visible spectrum extended-focus optical coherence microscopy for label-free sub-cellular tomography," Biomed. Opt. Express 8, 3343-3359 (2017),

- **P. J. Marchand**, A. Bouwens, T. Bolmont, V. K. Shamaei, D. Nguyen, D. Szlag, J. Extermann, and T. Lasser, "Statistical parametric mapping of stimuli evoked changes in total blood flow velocity in the mouse cortex obtained with extended-focus optical coherence microscopy," Biomed. Opt. Express 8, 1-15 (2017),

- M. Sison, S. Chakrabortty, J. Extermann, A. Nahas, **P. J. Marchand**, A. Lopez, T. Weil, and T. Lasser, "3D Time-lapse Imaging and Quantification of Mitochondrial Dynamics," Sci. Rep. **7**, 43275 (2017),

- M. Sylwestrzak, D. Szlag, **P. J. Marchand**, A. S. Kumar, and T. Lasser, "Massively parallel data processing for quantitative total flow imaging with optical coherence microscopy and tomography," Comput. Phys. Commun. 217, 128- 137 (2017),

- C. Berclaz, D. Szlag, D. Nguyen, J. Extermann, A. Bouwens, **P. J. Marchand**, J. Nilsson, A. Schmidt-Christensen, D. Holmberg, A. Grapin-Botton, and T. Lasser, "Label-free fast 3D coherent imaging reveals pancreatic islet micro- vascularization and dynamic blood flow," Biomed. Opt. Express 7, 4569-4580 (2016),

Conference presentations

- **P. J. Marchand**, A. Bouwens, S. Coquoz, D. Nguyen, M. Sison, J. Extermann, and T. Lasser, "Extended-focus Optical Coherence Microscopy in the visible wavelength range for live cell imaging," **Presented at:** ECBO, Munich 2015,

- **P. J. Marchand**, A. Bouwens, D. Szlag, T. Bolmont, and T. Lasser, "Quantitative Blood Flow Imaging of Functional Hyperaemia in the Mouse Cortex using Extended-focus Optical Coherence Microscopy," **Presented at:** ECBO, Munich 2015,

- **P. J. Marchand**, A. Bouwens, V. Shamaei, D. Nguyen, J. Extermann, T. Bolmont, and T. Lasser, 'Statistical parametric mapping of stimuli-evoked changes in quantitative blood flow using extended-focus optical coherence microscopy," **Presented at:** BIOS SPIE Photonics West, San Francisco 2016,

- **P. J. Marchand**, A. Bouwens, D. Nguyen, T. Bolmont, T. Harach, J. Extermann, and T. Lasser, "Imaging of functional hyperaemia using statistical parametric mapping and extended-focus optical coherence microscopy in the infrared spectral range," **Presented at:** BIOS SPIE Photonics West, San Francisco 2017,

- **P. J. Marchand**, A. Bouwens, D. Nguyen, M. Sison, S. Coquoz, D. Szlag, J. Extermann, and T. Lasser, 'Label-free subcellular tomography with extended-focus visible optical coherence microscopy," **Presented at**: ECBO, Munich 2017,